ON THE GEOPHYSICAL WELL LOG STUDIES OF SUBSURFACE FRACTURE ZONES IN A GRANITIC BATHOLITH.

by

John Cobbinah Owusu

A thesis
presented to the University of Manitoba
in partial fulfillment of the
requirements for the degree of
Master of Science
in
Geophysics

Department of Earth Sciences

Winnipeg, Manitoba

ON THE GEOPHYSICAL WELL LOG STUDIES OF SUBSURFACE FRACTURE ZONES IN A GRANITIC BATHOLITH

BY

JOHN COBBINAH OWUSU

A thesis submitted to the Faculty of Graduate Studies of the University of Manitoba in partial fulfillment of the requirements of the degree of

MASTER OF SCIENCE

ABSTRACT

The Underground Research Laboratory(URL) site on the Lac du Bonnet batholith, 12 km east of Lac du Bonnet, Manitoba, is one of several being investigated by the Atomic Energy of Canada Limited (AECL). Research is directed towards exploring the geological, geophysical and hydrological effects anticipated from the use of the granite batholith as a repository for nuclear waste. One of the major objectives of the geophysical research, is the location and mapping of subsurface fractures within the batholith.

This thesis, is concerned with the detection of fractures in a granite formation by Geophysical Well Logging and Vertical Seismic Profiling techniques. A review of the theoretical backgrounds of various geophysical logs tested in the URL experiment site has provided further insight into the factors and parameters that influence their performances in a granitic terrane. The potential of various geophysical logs in detecting fractures in a granitic formation was studied by correlation of well log data from one of the boreholes in the URL site, URL6. Results of the cross-correlation analysis indicate that the value of the correlation coefficient depends on the mineralogical and textural nature

of the formation, and may not always be a good measure of the agreement between various logs in detecting fractures.

The computational procedure to generate WKBJ synthetic seismogram for Vertical Seismic Profiling is also presented. The seismograms are accurate provided that the frequencies are very large compared to the velocity gradients of the medium such as in high resolution seismic technique. The seismogram becomes more accurate as the receiver distance from the well increases. The computation of the seismogram is extremely rapid as both inverse transforms in the algorithm are evaluated analytically. The WKBJ algorithm can handle direct, reflected and turning rays. Seismograms generated from the sonic and density data (from borehole URL6) are presented to illustrate the capability of VSP in determining the location of subsurface fracture zones. Primary reflection events from the fracture zones can be traced, level by level, to their point of origin within the formation.

ACKNOWLEDGEMENTS

The author expresses his appreciation to Dr. Wooil Moon for his interest and guidance during the course of the work. The author also wishes to thank Dr. Nash Soonawala and Mr. Art Holloway both of the Atomic Energy of Canada Ltd.(AECL), for providing the well log data and local geological information.

Financial support from the Atomic Energy of Canada Ltd.(AECL) and the Department of Earth Sciences, University of Manitoba is also greatly appreciated.

Finally, I would like to express my thanks to my fiancee, Cleantis, for her continuous support and encouragement.

CONTENTS

LIST OF TABLES

LIST OF FIGURES

Chapter I

INTRODUCTION

One of the serious long-range problems facing most industralized countries is what to do with the great stores of nuclear wastes that have been accumulating for years. These highly toxic radioactive waste are mostly by-products of nuclear power plants. Proposals for permanent storage sites for such nuclear waste have included blasting out underground vaults in plutonic crystalline rock or rock salt. Plutonic rock masses are igneous bodies which formed below the surface of the earth from magma. Rock salt is a coarsely crystalline halite formed as an evaporite. Rock salt is considered a suitable radioactive waste disposal environment because it is plastic and can flow. It is therefore self-sealing and there is virtually no possibility that emplaced radioactive waste can find a pathway to the biosphere(Tammemagi, 1976). The most serious drawback with this material, however, is the fact that salt deposits are associated with hydrocarbon deposits and therefore targets for exploration. Plutonic crystalline rocks on the other hand are homogeneous, structurally competent and seldom associated with mineralization. With these objectives, for the past few years, a number of countries including Canada, Austria, Sweden, France, U.S.A and Britain have been actively investigating the use of such plutonic rock bodies for

the disposal of nuclear radioactive waste material.

In 1980, the Atomic Energy of Canada Limited (AECL) acquired a 21-year old lease over a 3.8 km^2 area on the Lac du Bonnet batholith 12 km east of Lac du Bonnet, Manitoba(Fig.1.1(a)) for the construction of an underground research laboratory(URL). This laboratory will be used to conduct in situ geoscientific experiments in a realistic environment within the batholith. The area was chosen because it is located well within the Lac du Bonnet batholith which is considered to be representative of the granitic intrusives found in the Precambrain Shield; it also has an exellent bedrock exposure and close to the services and support facilities of the Whiteshell Nuclear Research Establishment

Since 1980, a comprehensive program of geological, geophysical and hydrological investigation have been underway to determine the characteristics of this batholith.

1.1 GEOLOGICAL AND HYDROGEOLOGICAL STUDIES

The regional geological setting of the URL site is shown in figure 1.1(b). It is located in the southeastern Manitoba, close to the border with Ontario. It is geologically situated within the English River gneissic belt, a major Archean subdivision of the western superior tectonic province of the Canadian Shield.

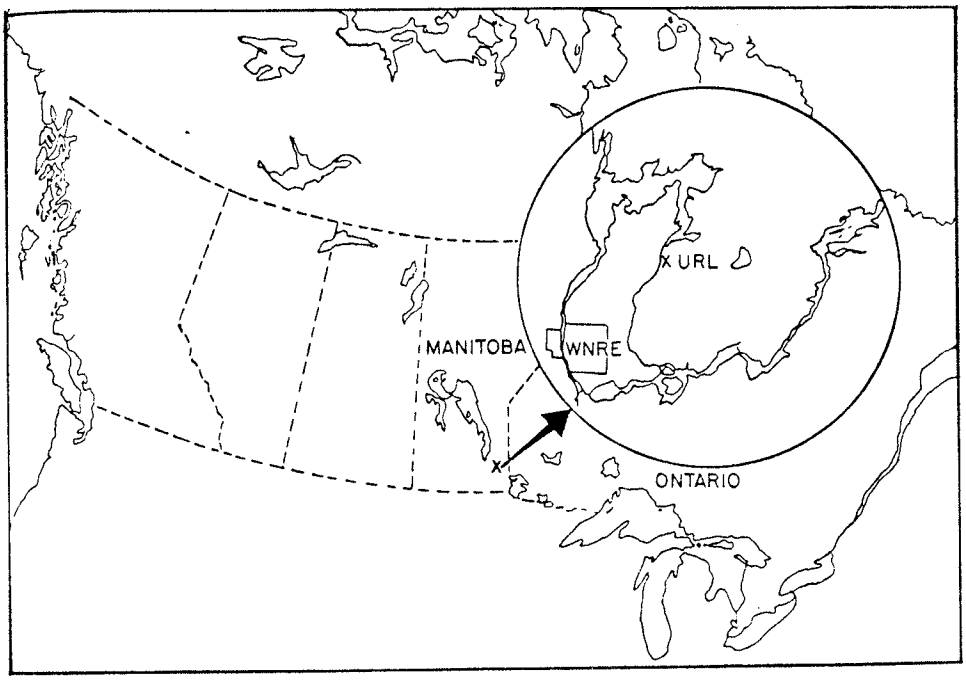

Figure 1.1(a): Location of Underground Research Laboratory (After Davison et al. 1982).

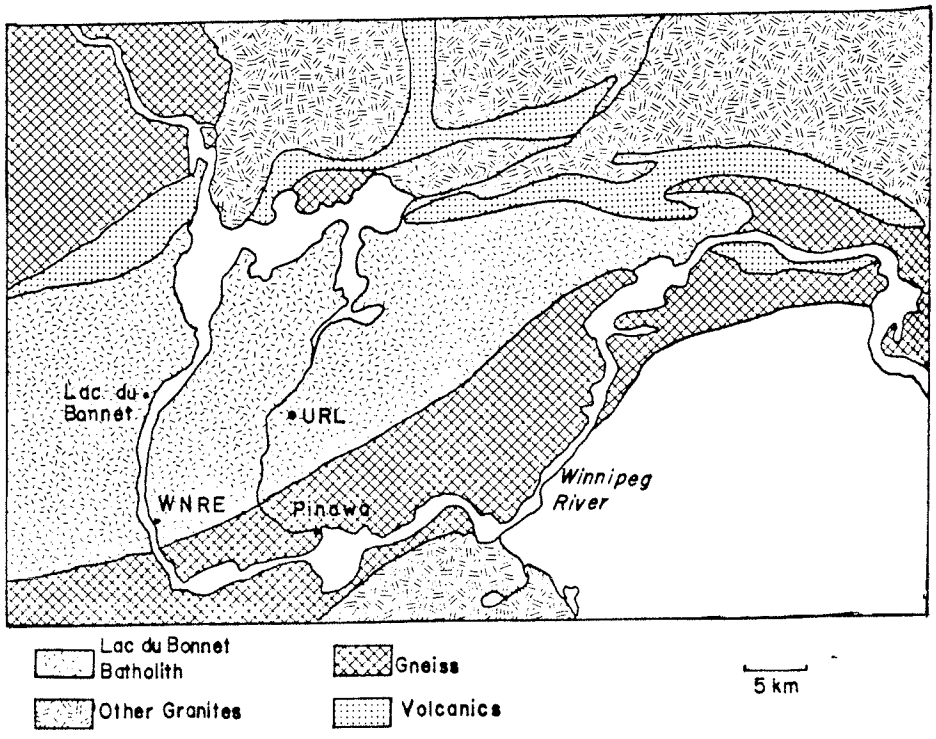

Figure 1.1(b): Geologic setting of the Underground Reserach Laboratory(After Davison et al. 1982).

Field evidence suggests that the Lac du Bonnet batholith is intrusive into the adjacent formations and that the intrusion may have postdated the last phase of the Kenoran orogeny (circa 2600my) in this area (Green, 1983). This suggestion is supported by a study of the microscopic deformational features which has shown that the batholith has undergone the least deformation compared to the rock units in the area. This URL area is composed of five granite units(Fig. 1.2); a pink porphyritic biotite granite (unit 1); foliated pink biotite-hornblende granite with strongly oriented biotite and hornblende crystals (unit 2); grey granite which at places grade into quartz monzonite (unit 3); a granite rich in xenolith of tonalite, granadiorite and quartz monzonite (unit 4) and a pink two-phase granite (unit 5). A study of the surface fractures has shown that there is a distinct fracturing pattern(fig. 1.3) and four possible sets of subvertical joints striking 025°, 115°, 045° and 165° were indicated by inspection of surface mapping(Brown, 1982). The grey granite is considerably less fractured than the other units; a fact which is also true at the subsurface.

Hydrogeological investigations have been undertaken at the URL site to study the natural undisturbed groundwater flow conditions. This involved a detailed investigation of both the shallow groundwater (arbitrary considered to extend to a depth of 70m) and the deep groundwater(below 70m) regimes.

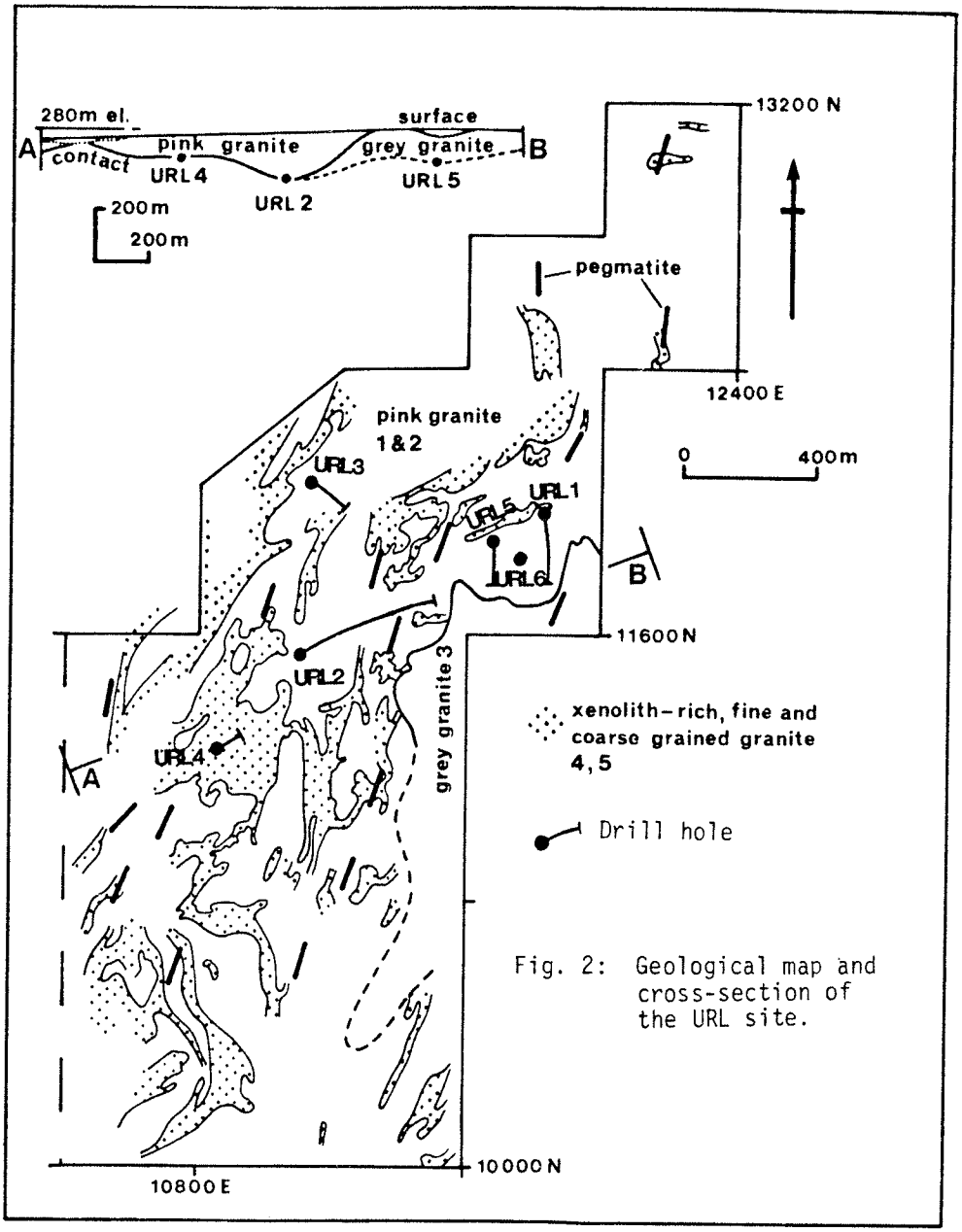

Fig. 2: Geological map and cross-section of the URL site.

Figure 1.2: Geological map of the Underground Research Laboratory(After Brown, 1982).

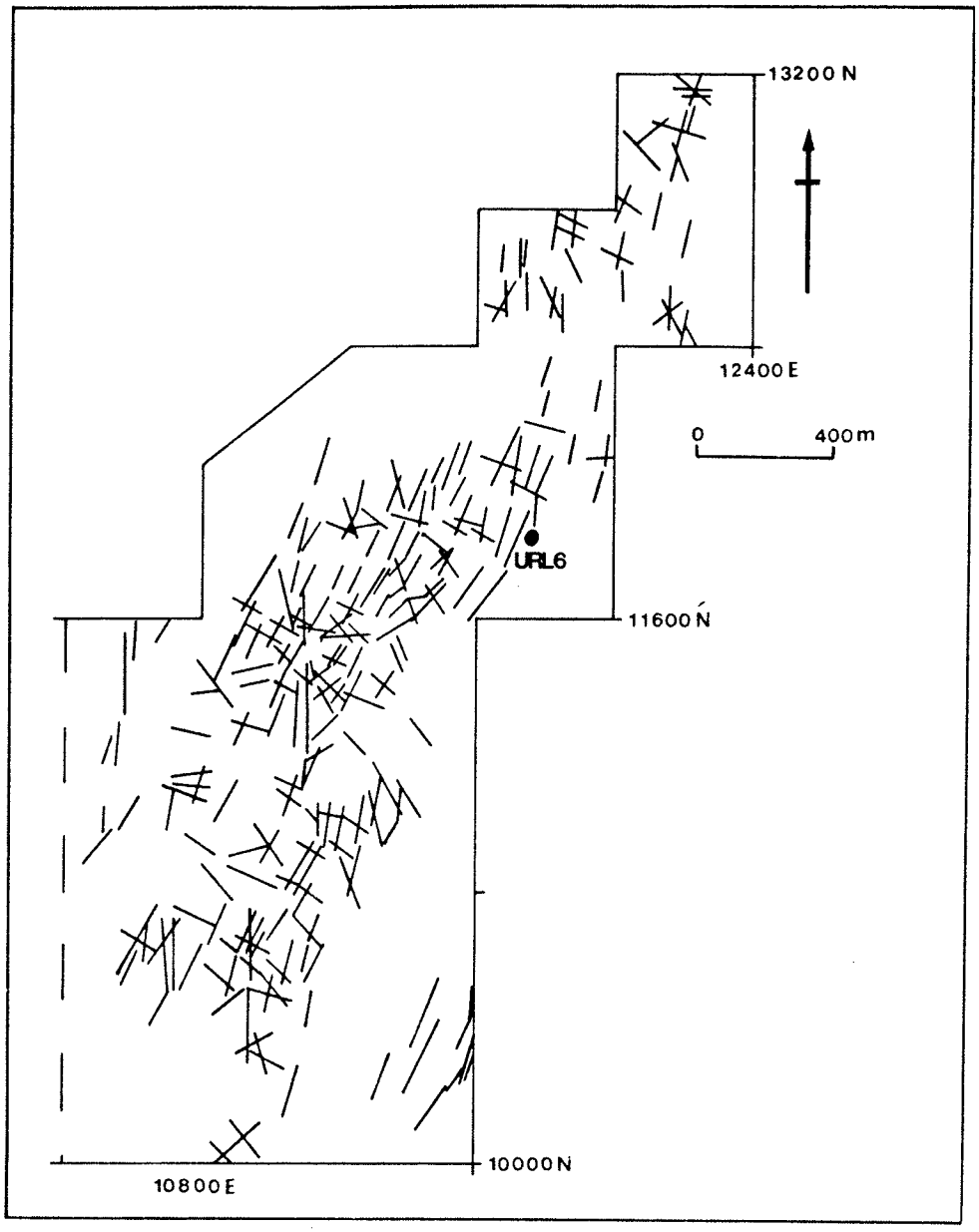

Figure 1.3: Trends of locally important sub-vertical fracture sets(After Brown, 1982).

About 30 percent of the URL area is covered by an overburden layer which is between 2 to 10m thick. The overburden material is composed of glaciolacustrine clays, silts and tills. The water conditions in this overburden has been measured by installing water table wells and piezometers. Results indicate a permeability of the order of $1*10^{-7}$ cm/s(Davison, 1982). The analysis of water samples from different levels in different boreholes suggest that the chemistry of the ground water from the deeper parts of the rock mass is distinctly different from that of the shallow parts. Davison(1982) divided the groundwaters into three different types based on their chemical composition. The shallow ground water is generally carbon dioxide enriched Ca-HCO type water and is relatively low in total disolved solid content. Groundwater from highly permeable fracture zones in the upper 150m of the rock is predominantly Na-HCO type indicating that calcium is being exchanged for sodium in this fracture zone. Water from another permeable fracture zone which appear to extend to depths of at least 330m at the URL area are characterized by increased Na and Cl content and also a high helium gas content(up to 70%).

1.2 GEOPHYSICAL STUDIES.

Different geophysical techniques have been used to study this area. A gravity survey conducted across the batholith shows that the batholith is located within a negative regional gravity anomaly and the depth to the base of the batholith is estimated to be 17.5 to 25.0 km (Brisbin, 1979). The result of a north-south aeromagnetic survey has also revealed a positive anomaly of 700 nT over this body. The total field increases smoothly from the edges into a high amplitude anomaly at the center. This peak at the center is believed to have been caused by relatively small, strongly magnetic, mafic xenoliths or intrusion(Green, 1983). A very low frequency electromagnetic and resistivity techniques, used to study the distribution of fractures, revealed that areas of low fracture density generally coincide with areas of resistivity values greater than 10000 Ω-m whereas high fracture density coincide with less than 2000 Ω-m(Soonawala, 1982). In crystalline rock, the only possible manner in which water may be release to the biosphere is by transportation via water filled fractures and faults. In view of this the location and mapping of subsurface fractures has become a major objective of the geophysical experiments. A number of downhole geophysical logs drilled in the area have succeeded in identifying the major fracture zones. Downhole television and borehole acoustic televiewer logging have also provided quantitative information regarding the width

and orientation of the fractures. Most of the fractures are shallow dipping. A high resolution seismic survey conducted over the area has confirmed the presence of the sub-horizontal fracture zones at depth(Green, 1981).

There are several theories as to the genesis and evolution of the fractures in this batholith. One hypothesis supported by Brisbin(1982) proposes a stress condition caused by a combination of epeirogenic uplift, isostatic rebound and westward horizontal plate movement. It is believed that old and filled fractures may have been developed during the emplacement of the pluton. As a result of uplift and differential uplift of the lithosphere caused by the unloading of glacial ice and sedimentary materials, these old fractures may have been reactivated causing some of them to open to fluid flow. Core analysis suggest that the shallow dipping fractures at shallow depths are zones of displacement and faulting. The absence of compressive loading is supported by milled materials, slickensides and gouges. The horizontal component of the stress which resulted in such low-dipping fractures may be related to the horizontal motion of the lithosphere.

This thesis is concerned with the detection of fractures in a granitic formation. The objectives are as follows:
a) The theory of the various geophysical logs used in the Underground Research Laboratory experiment will be reviewed to determine the factors and parameters that influence their performances in a granitic terrane.

b) Well-log data collected from one of the boreholes in the Underground Research Laboratory site(URL6), will be correlated to illustrate the the usefulness of geophysical logs in detecting fractures in a granitic formation.

c) Using the density and sonic log data and the WKBJ algorithm(Chapman, 1978), Synthetic VSP(Vertical Seismic Profiles) seismograms will be generated to illustrate the application of the Vertical Seismic Profilling technique to the detection of fractures.

Chapter II

THEORY OF GEOPHYSICAL LOGS.

Geophysical logging is widely utilized in hydrocarbon exploration where the type of formation usually encountered is sedimentary. For this reason, the fundamentals for both qualitative and quantitative interpretation of logs in sedimentary environments have been well studied and documented. In contrast, the application of geophysical logging technique in igneous and metamorphic terrane has not been extensive.

In this chapter, the theory of those geophysical logs, which are considered most suitable for fracture detection in a granitic terrane, will be reviewed. An attempt will also be made to explain some of the factors and parameters which influence their performances.

2.1 RESISTIVITY LOGGING.

Rocks are capable of transmitting electric currents mostly by means of absorbed water which they contain. The dissolved salts contained in the ground water constitute the electrolyte necessary for the conduction of current. In granite, the quantity of water contained in the pore spaces is extremely small and consequently, its resistivity is very high.

In many sedimentary strata, electric currents flow more easily in a direction parallel to the bedding planes than transversely to them. The reason for this is that a great number of mineral crystals possess a flat or elongated shapes along the bedding or foliation. At the time of deposition, they naturally take an orientation parallel to the bedding plane, and the electrons can travel with greater facility along these interstices which generally contain water with mineral solvents.

The fracture zones in a granite pluton can be considered as relatively thin beds of contrasting lithology and resistivities. The current flowing along the fracture zones will therefore be greater and consequently more conductive than the transverse direction. Such zones may include fractures filled with water or other conductive materials. The fracture zones may therefore exhibit macro-anisotropy which is different from the microanisotropy in stratified sedimentary formations in terms of the thickness of the beds. In general, the granite may be considered almost homogeneous except for these fractures. For theoretical analysis, a fractured granite may therefore be considered as an infinite macro-anisotropic medium.

Review of Theory.

The theoretical problem in resistivity logging is to evaluate the electric potential along the axis of a borehole due to a current source also located on the axis.

For a vertical borehole penetrating an infinite macro-anisotropic homogeneous medium with horizontally dipping fractures, we may define the horizontal resistivity R_H to be parellel to the fracture planes and a vertical resistivity R_V perpendicular to the fracture planes such that the mean resistivity R and the coefficient of macro-anisotropy λ are related to these parameters as

$$R = \sqrt{R_H \cdot R_V} \quad ; \quad \lambda = \sqrt{R_V / R_H} \qquad 2.1\text{-}1$$

The schematics of the configuration is shown in figure 2.1. The radius of the borehole is a and the z axis coincides with the axis of the borehole with the origin at the current source C. The current circuit is assumed to be completed through another electrode located at the surface and which is so far away from the elctrode C that its presence may be negleted when considering the current flow around C. For convenience, all linear measurements shall be defined in terms of the well radius. If δA is an element of surface and J the current density in amperes/meter^2, then the current I passing through δA is

$$I = J \cdot \delta A \qquad 2.1\text{-}2$$

The current density J and the electric potential V are related by

$$J = -\sigma \nabla V \qquad 2.1\text{-}3$$

where σ is the conductivity of the medium.

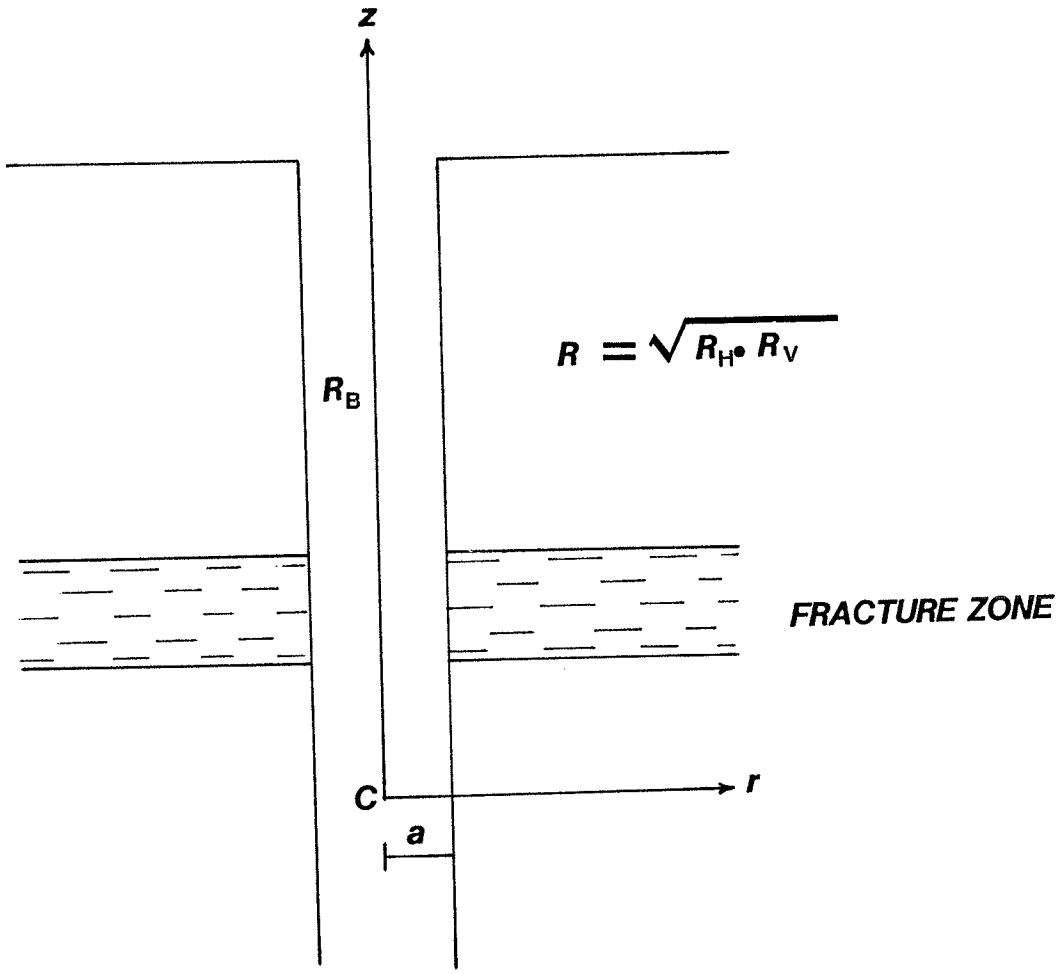

R_H - HORIZONTAL RESISTIVITY

R_V - VERTICAL RESISTIVITY

R_B - BOREHOLE FLUID RESISTIVITY

C - CURRENT ELECTRODE

a - RADIUS OF BOREHOLE

Figure 2.1: Configuration for a current source in a fluid-filled borehole.

In cylindrical coordinates, equation 2.1-3 can be written as(Kunz and Moran, 1958)

$$J = -\left(\frac{1}{R_H}\frac{\partial V}{\partial r}\hat{r} + \frac{1}{R_V}\frac{\partial V}{\partial z}\hat{z}\right) \qquad 2.1-4$$

If charge is conserved within a volume V enclosed by a surface A, then we can write

$$\int_A J \cdot dA = 0 \qquad 2.1-5$$

According to Gauss' Theorem, the volume integral of the divergence of the current throughout a given region is equal to the total charge enclosed, so that in this case

$$\int_V \nabla \cdot J \, dv = 0 \qquad 2.1-6$$

Taking V as an infinitesimal volume enclosing the current electrode C, we obtain for this point(Kunz and Moran, 1958)

$$\nabla \cdot J = \frac{1}{r}\frac{\partial}{\partial r}\left(\frac{r}{R_H}\frac{\partial V}{\partial r}\right) + \frac{\partial}{\partial z}\left(\frac{1}{R_V}\frac{\partial V}{\partial z}\right) \qquad 2.1-7$$

Kunz and Moran(1958) have shown that problems involving anisotropic media can be transformed into equivalent problems involving only isotropic media as(see Appendix A).

$$\nabla \cdot J = \frac{1}{r'}\frac{\partial}{\partial r'}\left(\frac{r'}{R'}\frac{\partial V'}{\partial r'}\right) + \frac{\partial}{\partial z'}\left(\frac{1}{R'}\frac{\partial V'}{\partial z'}\right) \qquad 2.1-8$$

where the primed quantities represent the equivalent for an isotropic medium. If we represent the potential and resistivity within the borehole as V_B and R_B respectively, and the formation potential as V_F, then equation 2.1-7 can be evaluated subject to the following boundary conditions.

a) The potential must be continuous across the wall of the borehole:

$$V_B(r,z) = V_F(r,z) \quad \text{at} \quad r = 1 \qquad 2.1-9$$

b) The normal components of the current density must be continuous across the wall of the borehole:

$$\frac{1}{R_B}\frac{\partial V_B(r,z)}{\partial r} = \frac{1}{R_H}\frac{\partial V_F(r,z)}{\partial r} \quad \text{at} \quad r = 1 \qquad 2.1-10$$

c) The potential within both the formation and the borehole must tend to zero at very large distance:

$$V_B(r,z)\ ,\ V_F(r,z) \longrightarrow 0 \quad \text{as} \quad \bar{x} \longrightarrow \infty \qquad 2.1-11$$

where $\bar{x} = \sqrt{r^2+z^2}$

d) For a point very close to the current source the potential must approach that of a homogeneous isotropic medium having a resistivity R_B :

$$V_B(r,z)\Big|_{\bar{x}\to 0} \longrightarrow \frac{R_B I}{4\pi a \bar{x}} \quad \text{as} \quad \bar{x} \to 0 \qquad 2.1-12$$

This becomes infinite as $\bar{x} \to 0$ hence the potential function should have the form:

$$V_B(r,z) = V(r,z) + V_B^*(r,z) \qquad 2.1-13$$

where V_B^* is finite and continuous at all points in the borehole except the origin where it is zero.

Equation 2.1-8 may be solved by Fourier's method. If a solution of the form

$$V(r', z') = f(r')\,\phi(z') \qquad 2.1-14$$

is assumed, then equation 2.1-8 becomes

$$\frac{f''(r')}{f(r')} + \frac{1}{r'}\frac{f'(r')}{f(r')} + \frac{\phi''(z')}{\phi(z')} = 0 \qquad 2.1-15$$

This can be seperated into two differential equations:

$$\frac{\phi''(z')}{\phi(z')} + m^2 = 0 \qquad 2.1-16a$$

$$\frac{f''(r')}{f(r')} + \frac{1}{r'}\frac{f'(r')}{f(r')} - m^2 = 0 \qquad 2.1-16b$$

where m is a constant. The solutions of equations 2.1-16a and 2.1-16b are of the form

$$\phi(z') = A(m)\cos mz' + B(m)\sin mz' \qquad 2.1-17a$$

$$f(r') = C(m)I_0(mr') + D(m)K_0(mr') \qquad 2.1-17b$$

where $I_0(mr')$ and $K_0(mr')$ are Bessel functions of the first and second kinds respectively; and A(m), B(m), C(m) and D(m) are constants depending on m. Since the potential must be not depend on sign of z, equation 2.1-14 cannot contain terms of the form $I_0(mr')\sin mz'$ and $K_0(mr')\sin mz'$, and so their coefficients must be zero. Hence the complete solution of equation 2.1-14 has the form of

$$V(r', z') = \int_0^\infty A(m)I_0(mr')\cos mz'\,dm + \int_0^\infty B(m)K_0(mr')\cos mz'\,dm \qquad 2.1-18$$

The potential function must satisfy the condition expressed in equations 2.1-12 and 2.1-13. Thus using the Weber-Lipschitz representation of the Bessel fuction:

$$V_B(r',z') = \frac{R_B I}{4\pi a\sqrt{r'^2+z'^2}} = \frac{R_B I}{2\pi^2 a}\int_0^\infty K_0(mr')\cos mz'\,dm \qquad 2.1-19$$

The function V_B^* , being finite and continuous through all space, cannot contain $K_0(mr')$ which becomes infinity as r' goes to zero; therefore equation 2.1-13 is satisfied if

$$B(m) = \frac{R_B I}{2\pi^2 a} \quad \text{and} \quad V_B^*(r',z') = \int_0^\infty A(m) I_0(mr')\cos mz'\,dm \qquad 2.1-20$$

Therefore the potential within the borehole is :

$$V_B(r',z') = \frac{R_B I}{2\pi^2 a}\int_0^\infty K_0(mr')\cos mz'\,dm + \int_0^\infty A(m) I_0(mr')\cos mz'\,dm \qquad 2.1-21$$

In the formation, the potential cannot terms involving $I_0(mr')$ which tend to become infinite for large values of r'. Therefore, the potential in the formation is:

$$V_F(r',z') = \int_0^\infty B(m) K_0(mr')\cos mz'\,dm \qquad 2.1-22$$

Making the following substitutions:

$$C(m) = \frac{2\pi^2 a}{R_B I} A(m) \qquad 2.1-23a$$

$$D(m) = \frac{2\pi^2 a}{R' I} B(m) \qquad 2.1-23b$$

Equations 2.1-21 and 2.1-22 can be re-written as

$$V_B(r',z') = \frac{R_B I}{2\pi^2 a}\left[\int_0^\infty K_0(mr')\cos mz'\,dm + \int_0^\infty C(m) I_0(mr')\,dm\right] \qquad 2.1-24a$$

$$V_F(r',z') = \frac{R' I}{2\pi^2 a}\int_0^\infty D(m) K_0(mr')\cos mz'\,dm \qquad 2.1-24b$$

From equation A.7 in appendix A, we have

$$r' = r/\lambda \quad ; \quad z' = z \quad \text{and} \quad R' = \frac{R}{\lambda} = R_H \qquad 2.1-25$$

Substituting the above into equations 2.1-24a and 2.1-24b and noting that $\lambda=1$ for the borehole fluid, the potential function within the borehole and the formatiom are

$$V_B(r,z) = \frac{R_B I}{2\pi^2 a}\left[\int_0^\infty K_0(mr)\cos mz\,dm + \int_0^\infty C(m) I_0(mr)\cos mz\,dm\right] \qquad 2.1-26a$$

$$V_F(r,z) = \frac{RI}{2\pi^2 \lambda a}\int_0^\infty D(m) K_0(mr/\lambda)\cos mz\,dm \qquad 2.1-26b$$

To evaluate C(m) and D(m) we shall use the boundary conditions implied in equations 2.1-9 and 2.1-10. That is

$$V_B(r,z)\Big|_{r=1} = V_F(r,z)\Big|_{r=1} \qquad 2.1-27a$$

and

$$\frac{1}{R_B}\frac{\partial V_B(r,z)}{\partial r}\Big|_{r=1} = \frac{1}{R_H}\frac{\partial V_F(r,z)}{\partial r}\Big|_{r=1} \qquad 2.1-27b$$

For equation 2.1-27a this gives

$$R_B K_0(m) + R_B C(m) I_0(m) = \frac{R}{\lambda} D(m) K_0(m/\lambda) \qquad 2.1-28$$

Making use of the Bessel function identity:

$$I_0'(x) = I_1(x) \quad ; \quad K_0'(x) = -K_1(x) \qquad 2.1-29$$

where the prime quantities indicate complete derivatives of the corresponding Bessel functions. The potential gradients become

$$\frac{\partial V_B(r,z)}{\partial r} = \frac{R_B I}{2\pi^2 a}\int_0^\infty \left[-K_1(mr) + C(m) I_1(mr)\right]\cos mz \cdot m\,dm \qquad 2.1-30a$$

and

$$\frac{\partial V_F(r,z)}{\partial r} = \frac{RI}{2\pi^2 \lambda a}\int_0^\infty - D(m) K_1(mr/\lambda)\cos mz \cdot m\,dm \qquad 2.1-30b$$

Equation 2.1-27b requires that

$$\frac{1}{R_B}\left.\frac{\partial V_B(r,z)}{\partial r}\right|_{r=1} = \frac{1}{R_H}\left.\frac{\partial V_H(r,z)}{\partial r}\right|_{r=1} \qquad 2.1-31$$

From equations 2.1-30a and 2.1-30b this means

$$C(m)\,I_1(m) - K_1(m) = -\frac{\Delta(m)}{\lambda}K_1(m/\lambda) \qquad 2.1-32$$

Solving equations 2.1-28 and 2.1-32 we obtain

$$C(m) = \frac{\frac{R\lambda}{R_B}K_1(m)K_0(m/\lambda) - K_0(m)K_1(m/\lambda)}{\frac{R\lambda}{R_B}I_1(m)K_0(m/\lambda) + I_0(m)K_1(m/\lambda)} \qquad 2.1-33$$

At points along the z axis(r=0) the potential is given by

$$V_B(r,z)\Big|_{r=0} = \frac{I R_B}{2\pi^2 a}\left[\frac{\pi}{2z} + \int_0^\infty C(m)\cos mz\, dm\right] \qquad 2.1-34$$

2.1.1 Normal resistivity log.

In normal resistivity logging, a low frequency alternating current is sent through the formation via current electrodes C_1 and C_2(fig. 2.2) thereby creating an electrical field in the surrounding media. C_1 and C_2 are assumed to be wide apart so that the effect of their electric fields on the other is negligible.

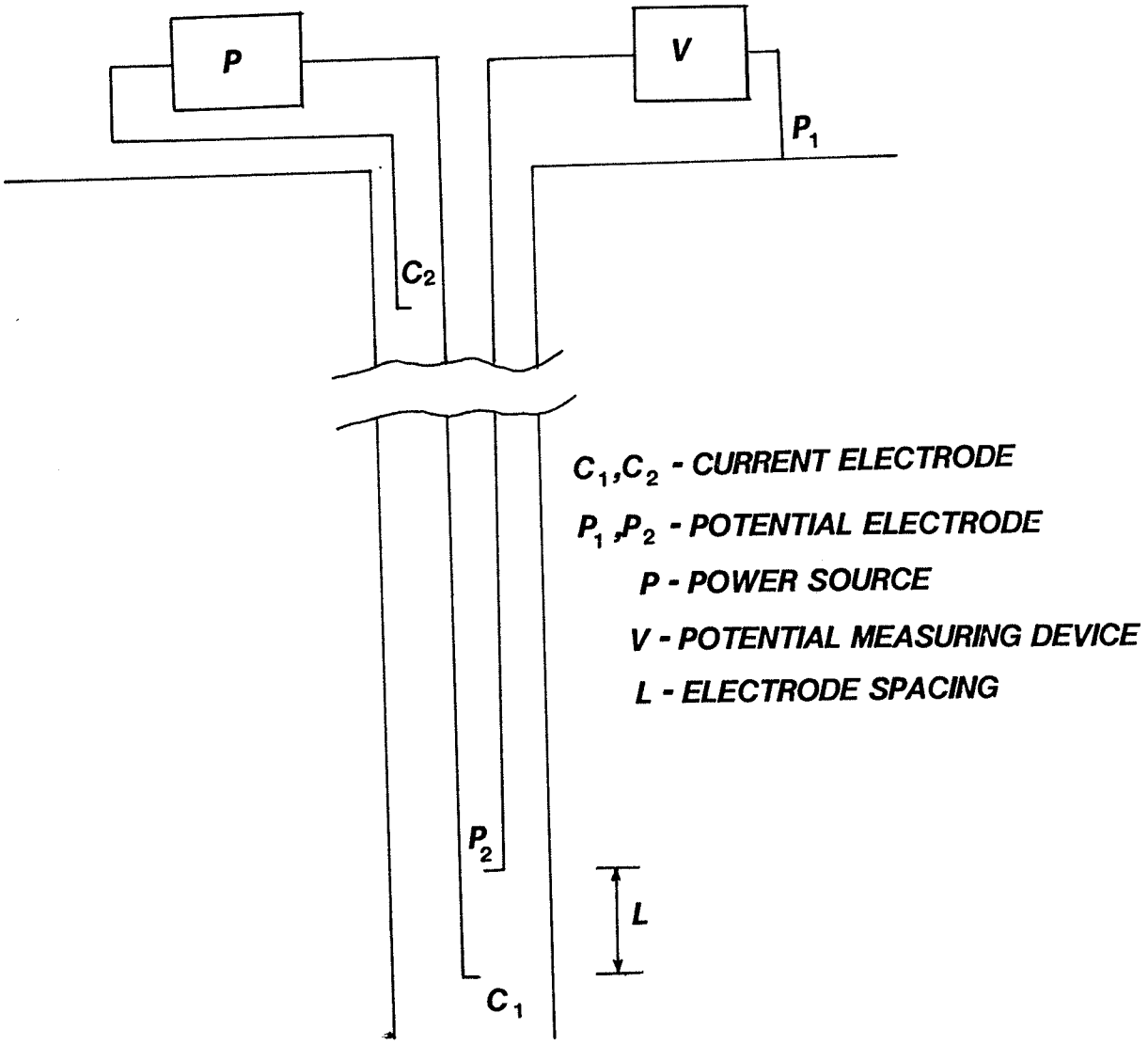

Figure 2.2: Schematics of normal resistivity tool.

The apparent resistivity Ra measured by the normal resistivity log is given by

$$R_a = \frac{4\pi L V_B(0,L)}{I} \qquad 2\cdot1\cdot1-1$$

making the substitution z = L/a in equation 2.1-34 we have

$$R_a = R_B + \frac{2R_B L}{\pi a}\int_0^\infty \left[\frac{\frac{\lambda R}{R_B} K_1(m)K_0(m/\lambda) - K_0(m)K_1(m/\lambda)}{\frac{\lambda R}{R_B} I_1(m)K_0(m/\lambda) + I_0(m)K_1(m/\lambda)}\right]$$

$$= R_B + \frac{R_B L}{a}\cdot F \qquad 2\cdot1\cdot1-2$$

where F is a function of the macro-anisotropy λ, ratio of the mean resistivity of the surrounding rock formation R to the borehole fluid resistivity R_B and the ratio of the electrode spacing L to the borehole radius a. Hence the apparent resistivity measured by the normal log depends on the electrode spacing, the diameter of the borehole, the resistivity contrast between the surrounding rock formation and the borehole fluid, the macro-anisotropy and the resistivity of the formation between the electrodes. The effect of these factors on the normal resistivity log are discussed below.

Ratio of electrode spacing to borehole radius.

For electrode spacing small compared to the hole diameter, i.e L/a very small

$$\frac{2L}{\pi}\int_0^\infty C(m)\cos mL\, dm \longrightarrow 0 \qquad 2\cdot1\cdot1-3$$

and the apparent resistivity Ra approaches the borehole fluid resistivity. For electrode spacing very large compared to the borehole radius i.e L/a very large, it can be shown that

$$\frac{2L}{\pi a}\int_0^{\infty} C(m)\cos\frac{mL}{a}\,dm \longrightarrow \frac{R - R_B}{R_B} \qquad 2\cdot1\cdot1-4$$

The apparent resistivity is approximately equal to the mean resistivity of the surrounding rock formation, R. The physical basis for the above behaviour is that for a large electrode spacing, the measured current is able to penetrate deeper into the surrounding rock formation. This however is achieved at the expense of the vertical resolution; because as the electrode spacing increases it becomes increasingly difficult to resolve the very thin fractures. This partly explains the difference in the resistivity values measured by the resistivity 32'' and 16'' logs.

Resistivity of the formation.

The conductivity of the formation between the electrodes will be controlled primarily by the water content and to a lesser extent by the mineralogical composition of the formation. Water content strongly affects the electrical properties of rocks at moderate temperatures because of the much higher conductivity of water relative to the constituent minerals in most rocks. The conductivity of water bearing fracture zones will depends upon the quantity and distribution of the water within the fractures.

At low concentrations of water the effect is controlled by the physical and chemical processes between the water and the fracture surface(Olhoeft, 1981). But with increasing water content the bulk conductivity becomes less sensitive to surface effects and more dependent upon the conductivity of the water held in the fractures.

Macro-anisotropy.

The variation of micro-anisotropy with Ra/R_b has been investigated by Kunz and Moran(1958). For a given R_H/R_b, increased micro-anisotropy corresponds in general to an increased Ra. A normal resistivity log perpendicular to the plane of the beds measures the horizontal resistivity so an increase in microanisotropy can be viewed as an increased tendency for the measured current to flow more deeply into the formation. A similar relationship can be expected to exist in a macro-anisotropic medium since both phenomena are the similar. Campbell(1977) studied the relation between the macro-anisotropy coefficient and resistivity contrast between the different formations. The results for a sequence of interbedded layers with different resistivities are shown in fiqure 2.3. The parameter f represent either f_1, the fraction of the total thickness having resistivity ρ_1 or f_2, the fraction of the total thickness having resistivity ρ_2. The macro-anisotropy increases with increasing fraction of the more resistive bed.

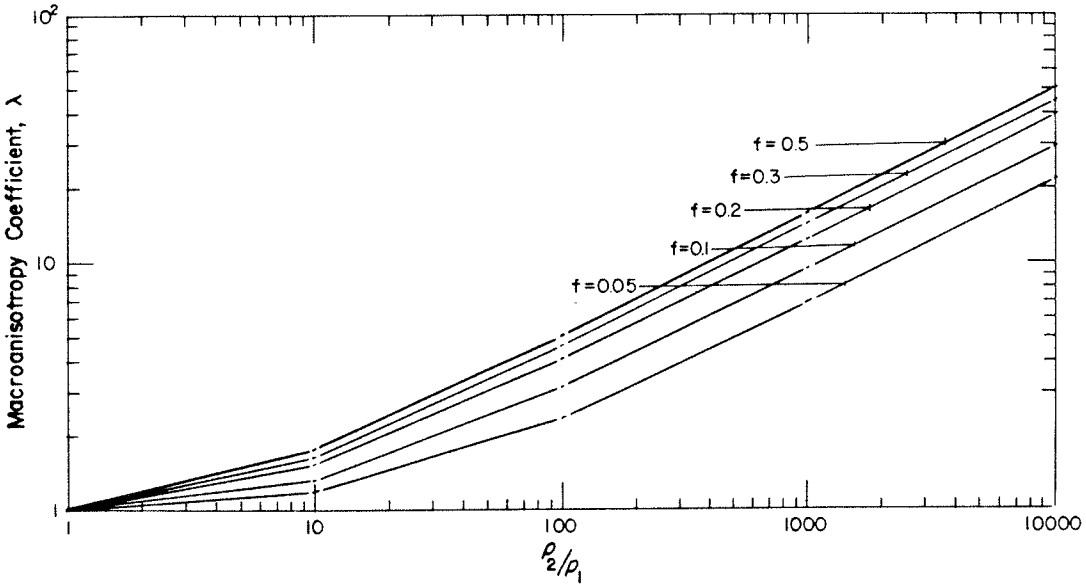

Figure 2.3: Macro-anisotropy coefficient for a sequence of interbedded layers of resistivities and . The parameter f represents either f_1, the fraction of the total thickness having resistivity , or f_2, the fraction of totatal thickness having resistivity . Thus to find values appropriate for, say, $f_1=0.8$, we use the curve for $f=f_2=0.2$ (After Campbell, 1977).

This suggests probable decrease in macro-anisotropy for intense fracture zones which contain less resistive materials. The macroanisotropy also depends on the proportion of vertical and horizontal fractures. Vertical fractures reduce the effective macro-anisotropy by offering vertical path to the measured current. For a fixed electrode spacing, an increase in the thickness of the fracture zones would lead to a decrease in the effective macro-anisotropy of the formation.

Resistivity contrast.

For a fixed electrode spacing, the apparent resistivity Ra approaches the resistivity of the fluid in the borehole as the resistivity contrast between the formation and borehole fluid increases. This phenomenum is due to the tendency of the measured current to take the least resistive path; the current therefore travel along the fluid column in the borehole instead of within the formation. An increase in the thickness of fracture zones which contain less resistive materials would reduce the resistivity contrast between the formation and the borehole fluid. The apparent resistivity value would therefore be determined to a considerable extent by the resistivity of the fracture infilling materials.

2.1.2 Focused-beam log

The focused-beam are a family of resistivity tools which use focusing currents to control the path taken by the measured currents. Schlumberger's laterlog 7(Doll, 1951) shown in figure 2.4 can be used to illustrate the principle of the focused-beam devices.

At the center of this seven-electrode array, the main current electrode A_0 emits a constant measured current I_0. Symmetrically arranged around A_0 are two pairs of potential electrodes, M M' and N N' . At the end of the array are two more electrodes, A and A' which are equidistant from A_0. The focusing current from A and A', I is continuously varied in such a way that the potential difference between electrodes MN and M'N' is zero forcing I_0 to flow in a narrow disc horizontally outward into the formation. For a homogeneous medium the shape of the current beam and the value of the I is constant. In the presence of inhomogeneties, the value of I will change and thereby changing the potential at N but not the shape of the beam I_0, since a zero potential difference still exist between electrodes MN and M'N'.

Review of Theory.

Consider a Laterlog 7 array, with its electrode lying in an infinite homogeneous medium with A_0 as the origin and electrode spacing a,b and c(Fig. 2.5). The potential at N can be expressed as(Jackson, 1981):

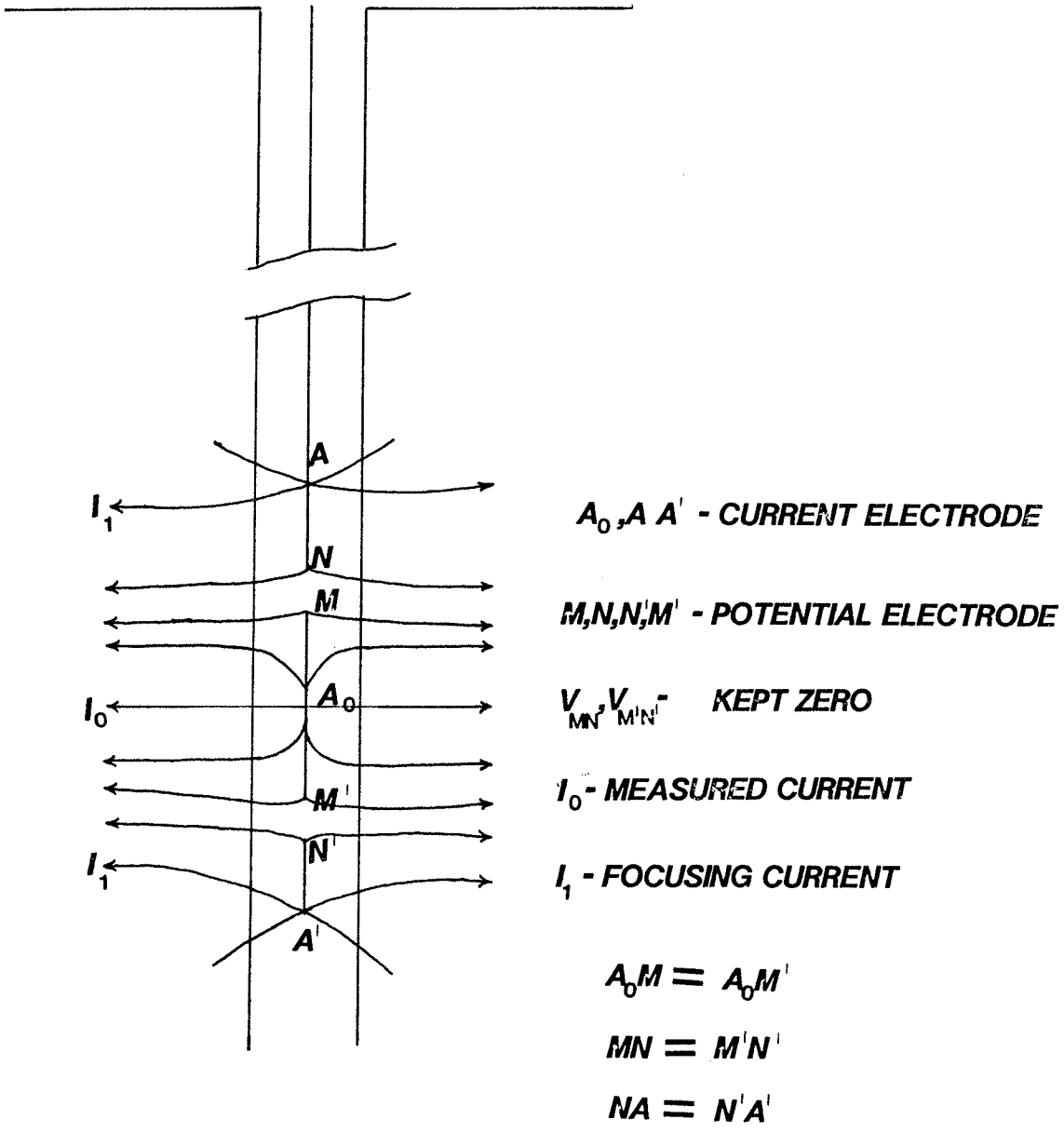

Figure 2.4: Focused-beam log in a fluid-filled borehole (After Jackson, 1981).

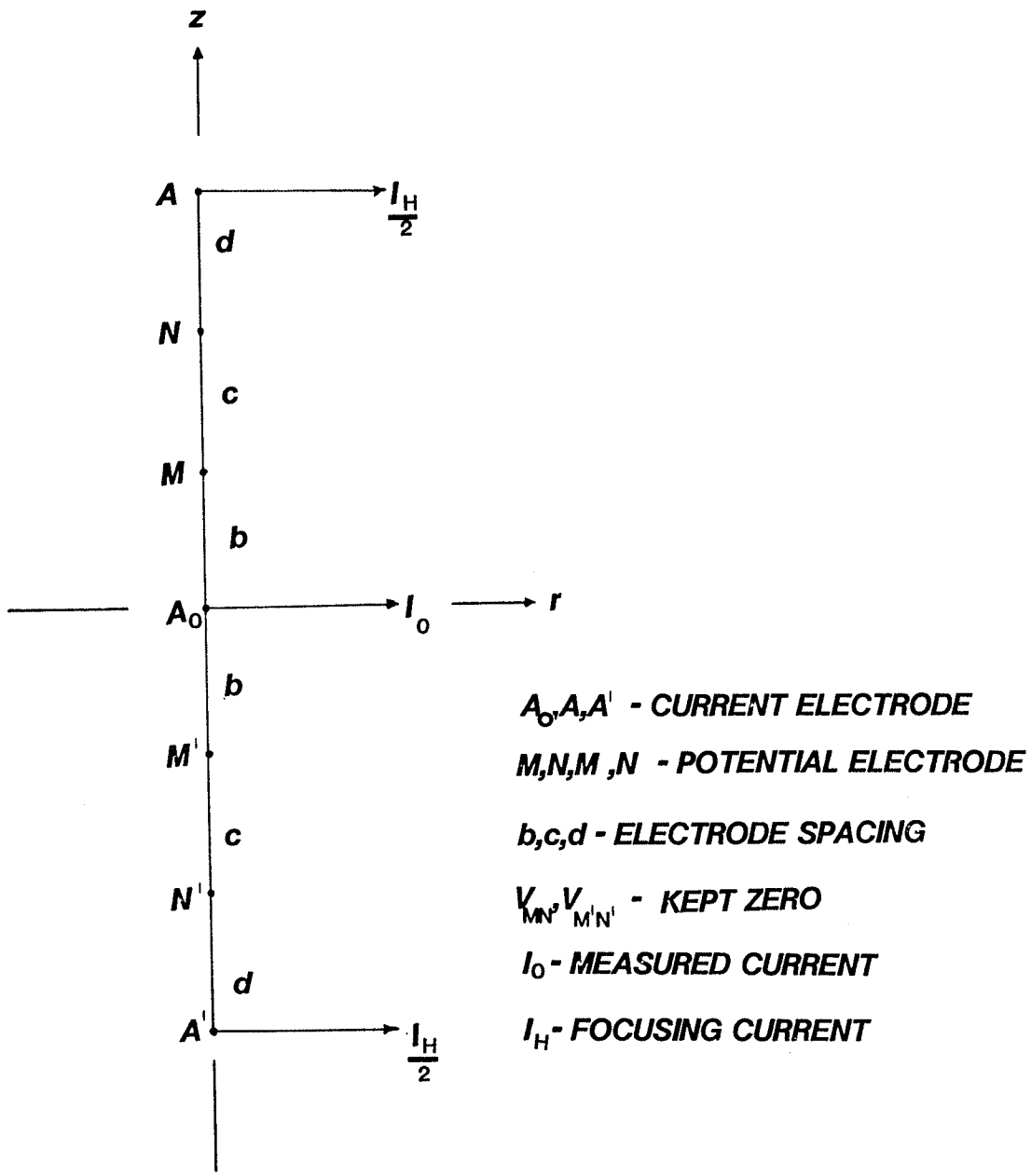

Figure 2.5: Focused-beam log in a homogeneous medium.

$$V(0,N) = \frac{RI_0}{4\pi A_0 N} + \frac{R I_H/2}{4\pi}\left\{\frac{1}{AN} + \frac{1}{A'N}\right\} \qquad 2\cdot1\cdot2-1$$

where I_H is the value of I for a homogeneous medium. For a general point (0,z) on the axis, the potential is given by(Jackson, 1981)

$$V(0,z) = \frac{R}{4\pi}\left\{I_0 F(0,z) + I_H E(0,z)\right\} \qquad 2\cdot1\cdot2-2$$

F(0,z) and E(0,z) depend on the relative position of the potential electrode (0,z) and the current electrodes A_0, A and A'(See appendix B for derivation of F(0,z) and E(0,z)). The potential at M(z=b) is given by

$$V(0,b) = \frac{R}{4\pi}\left\{I_0 F(0,b) + I_H E(0,b)\right\} \qquad 2\cdot1\cdot2-3$$

Similarly for N(z=b+c)

$$V(0,b+c) = \frac{R}{4\pi}\left\{I_0 F(0,b+c) + I_H E(0,b+c)\right\} \qquad 2\cdot1\cdot2-4$$

For zero potential difference between M and N,

$$I_0 F(0,b) + I_H E(0,b) = I_0 F(0,b+c) + I_H E(0,b+c)$$

$$V(0,b) = V(0,b+c) \qquad 2\cdot1\cdot2-5$$

giving

$$I_H = I_0\left[\frac{F(0,b+c) - F(0,b)}{E(0,b) - E(0,b+c)}\right] \qquad 2\cdot1\cdot2-6$$

Then

$$V(0,b) = \frac{RI_0}{4\pi}\left[F(0,a) + \left\{\frac{F(0,b+c)-F(0,b)}{E(0,b)-E(0,b+c)}\right\}E(0,b)\right] \qquad 2\cdot1\cdot2-7$$

hence the resistivity of the homogeneous medium is given by

$$R = \frac{V(0,b)\cdot GF}{I_0} \qquad 2\cdot1\cdot2-8$$

where the geometrical factor GF is given as

$$GF = \frac{4\pi}{\left[F(0,b) + \left\{\frac{F(0,b+c)-F(0,b)}{E(0,b)-E(0,b+c)}\right\}E(0,b)\right]} \qquad 2\cdot1\cdot2-9$$

Hence the geometrical factor depends only on the electrode arrangement. Now consider the Laterolog array in the presence of a borehole(Fig. 2.4). The notations are the same as used in the case of the normal resistivity log. The potential at M is given in appendix C, by sum of the effects of three current electrodes as

$$V_{A_0AA'}(M) = \frac{R_B I_0}{4\pi a}\left\{F(0,b') + J_0 E(0,b') + F'\left(\lambda, \frac{R}{R_B}, b', c', d'\right)\right\}$$

where $2\cdot1\cdot2-10$

$$J_0 = I_1/I_0$$

and

$$F'\left(\lambda, \frac{R}{R_B}, b', c', d'\right) = 2\pi\left\{\int_0^\infty C(m)\cos mb'\,dm + J_0\int_0^\infty C(m)\left[\cos m(c'+d') + \cos m(2b'+c'+d')\right]dm\right\}$$

where

$$b' = A_oM = A_oM', \qquad c' = MN = M'N', \qquad d' = NA = N'A'$$

Thus from equation 2.1.2-8 the apparent resistivity Ra is given as

$$R_a = \frac{4\pi V_{A_oAA'}(M)}{I_o\left[F(o,b') + \left\{\frac{F(o,b'+c') - F(o,b')}{E(o,b') - E(o,b'+c')}\right\}E(o,b')\right]} \qquad 2.1.2-11$$

Hence, the focused-beam log is influenced by the same factors as the normal resistivity log namely the micro-anisotropy of the formation, the resistivity of the formation, the resistivity contrast between the formation and the borehole fluid and the electrode spacing. However, by constraining the measured current to flow out horizontally into the formation rather than spreading out vertically, the effect due to a large resistivity contrast is greatly minimized. Because of this, the focused-beam log measures the resistivity of the formation much more accurately than the normal logs. The thickness of the current sheet Io is approximately 32'' and this is retained up to a distance from the borehole somewhat greater than the total length AA'(80'')(Schlumberger, 1972).

2.1.3 Single-point resistance log.

In the single-point resistance logging, a low alternating current I, is driven through the ground between an electrode A in the borehole and a surface return electrode B(Fig. 2.6). The amount of current which flows in such a circuit is given by

$$I = \frac{E}{\sum R_i + R_A} \qquad 2.1.3-1$$

where $\sum R_i$ is the sum of the resistances of the various components of the recording equipment and R_A is the grounding resistance of the electrode in the borehole. The grounding resistance is proportional to the effective resistivity, ρ_e, of the formation close to the electrode:

$$R_A = T \cdot \rho_e \qquad 2.1.3-2$$

where T is the geometric factor of the single-point resistance electrode. Thus equation 2.1.3-1 becomes:

$$I = \frac{E}{\sum R_i + T \cdot \rho_e} = \frac{E}{Const. + T \cdot \rho_e} \qquad 2.1.3-3$$

hence the current will tend to increase in the zones of low effective resistivity and decrease in the zones of high effective resistivity. This current is measured under a constant applied voltage and recorded as a resistance curve.

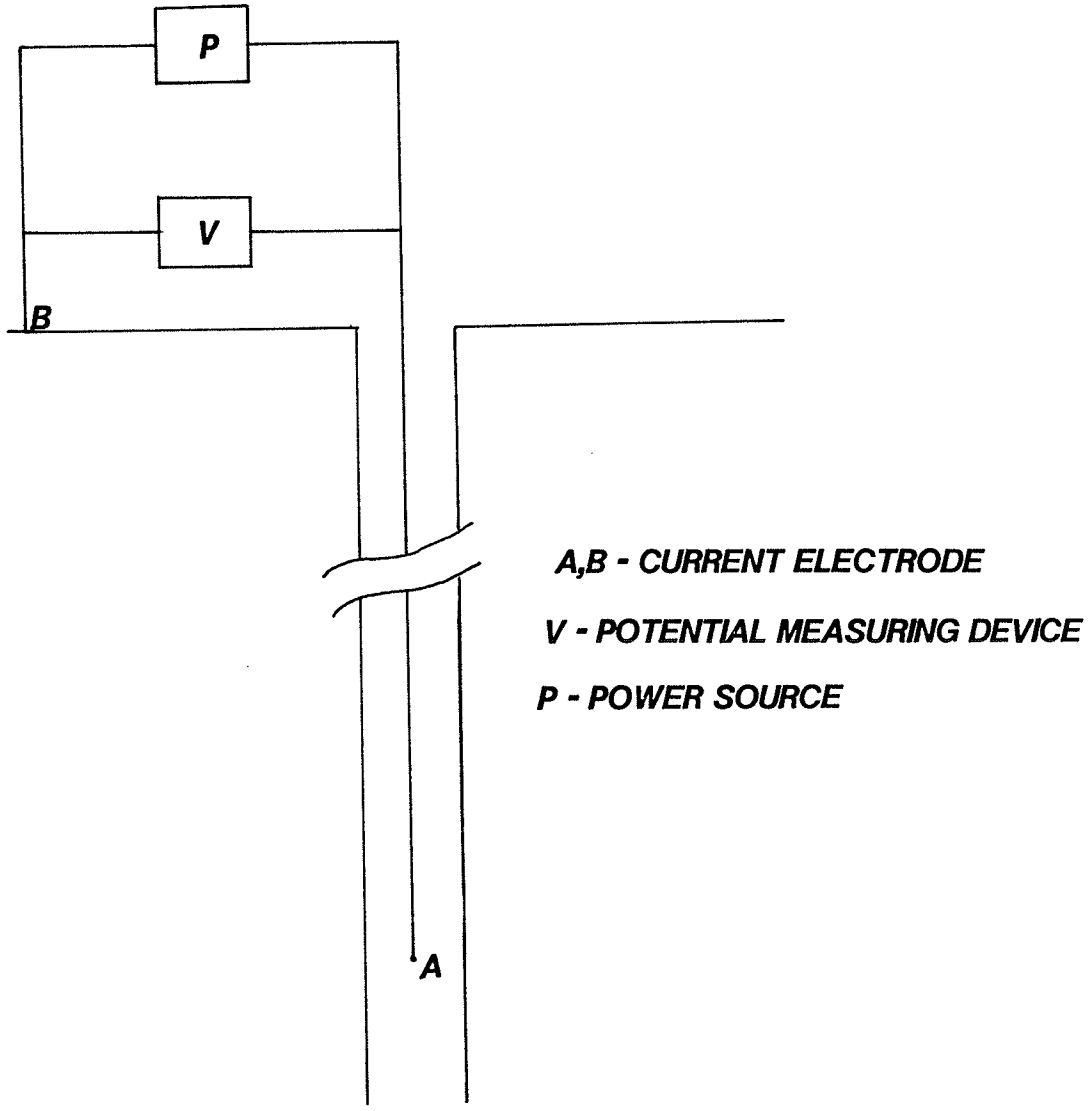

Figure 2.6: Schematics of a single-point resistance logging tool.

Review of Theory.

The grounding resistance of a spherical elctrode within a borehole which penetrate an infinite homogeneous macro-anisotropic medium can be approximated by the resistance of a series of thin shells(fig. 2.7) if we replace the formation with an equivalent isotropic formation. The shells are spherical and composed of the formation material except for small zones within the borehole which are represented by flat discs. The total resistance of a such a shell is given by(Dakhnov, 1962)

$$R_T = \frac{R_B}{4\pi}\left(\frac{1}{r_e} - \frac{1}{a}\right) + \frac{R'}{4\pi a}\cdot\frac{\pi/2}{\sqrt{R'/2R_B + 1}} \qquad 2\cdot1\cdot3-4$$

where R' is the resistivity of the equivalent isotropic formation, R is the resistivity of the borehole fluid and re the radius of the electrode. For a spherical electrode the geometric factor is $1/4\pi r_e$, hence the effective resistivity measured by the single-point electrode is

$$\rho_e = \frac{R_T}{T} = 4\pi r_e\left[\frac{R_B}{4\pi}\left(\frac{1}{r_e}\right) - \frac{R_B}{4\pi a}\cdot\frac{\pi/2}{\sqrt{R'/2R_B + 1}}\right]$$

$$= R_B\left[1 + \frac{r_e}{a}\left(\frac{R'}{R_B}\cdot\frac{\pi/2}{\sqrt{R'/2R_B + 1}} - 1\right)\right]$$

$2\cdot1\cdot3-5$

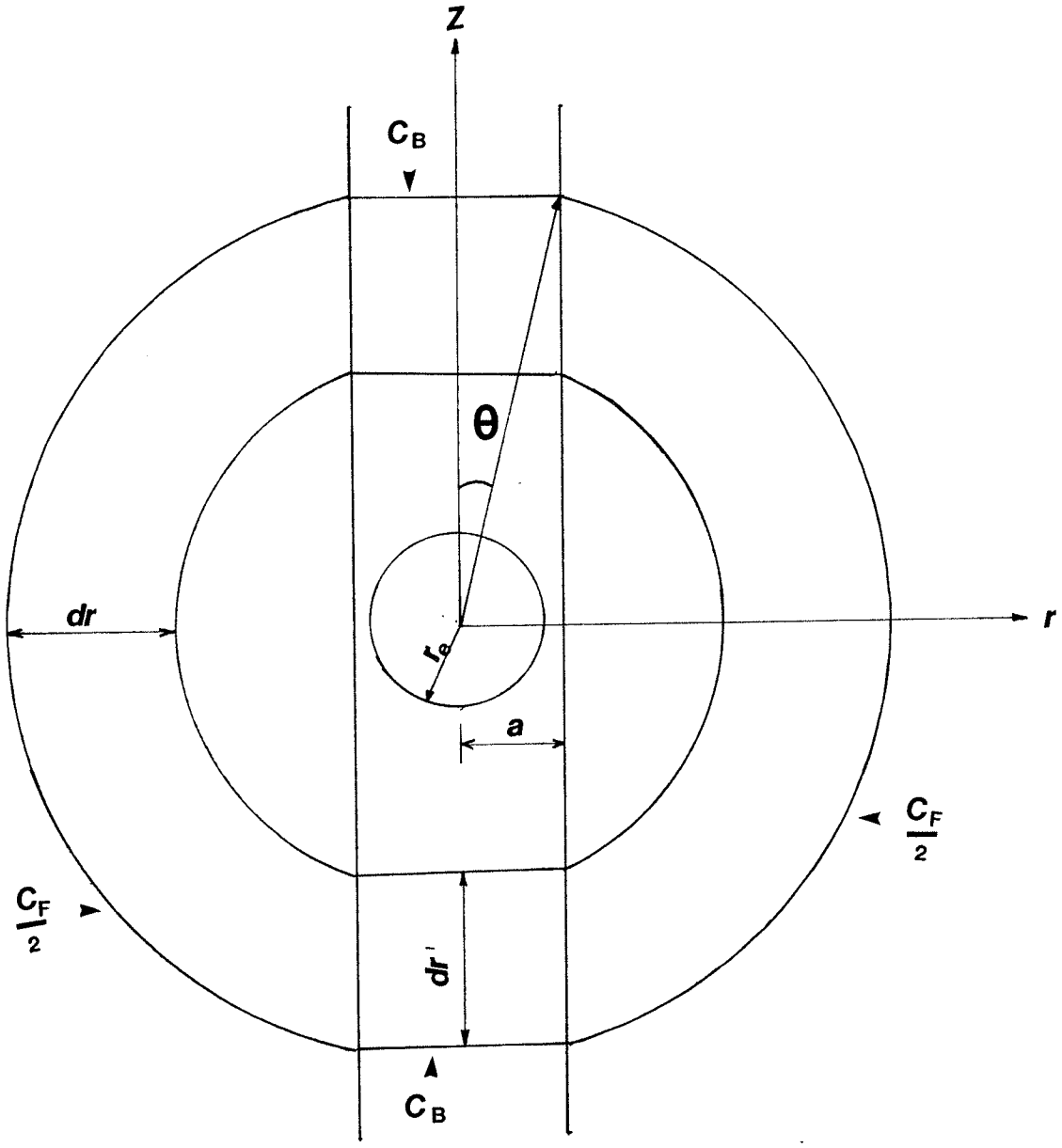

Figure 2.7: Configuration for grounding potential of a spherical electrode(After Dakhnov, 1962).

The effect of the formation becomes increasingly greater as its resistivity is raised in relation to the resistivity of the borehole fluid. But if the ratio of the electrode diameter to the borehole diameter is very small, then from equation 2.1.3-5 we have

$$\rho_e \simeq R_e \qquad 2.1.3-6$$

This means that the grounding resistance of the electrode will be affected to a very minor extent by the formation. This effect will even be more pronounced if the borehole fluid is relatively more conductive than the formation as is in the case of granite. The penetration of the current is about five times the diameter of the electrode(Kayal, 1979); the current therefore cannot penetrate highly resistive fracture zones. In such zones, the log will not only record a low resistance but would also fail to reveal many details of the fracture zone. Thus, in order to detect fracture zones and other inhomogeneties in a highly resistive formation such as granite, the resistivity being measured should be comparable to the borehole fluid resistivity.

The interval between 150m and 250m on the normal and the resistance logs (fig.4.3) is rather featureless even though the focused-beam log detects fracturing within this interval. Unlike the fracture zones at 90-150m and 267-272m, this interval is characterized by very high background resistivity value.

The absence of fracturing on the normal and the resistance logs may be attributed to the large resistivity contrast between the formation within this interval and the borehole fluid. The mean resistivity of the borehole fluid is about 52 Ω-m whiles the formation resistivity for this interval is in the order of 1000 Ω-m. This gives a resistivity contrast of the order of 1000 Ω-m which may be large enough to alter the path taken by the measured current. It is also realized that the resistance log is capable of detecting only the abnormally low resistive zones.

2.2 SPONTANEOUS POTENTIAL LOGGING.

Spontaneous potential logging consists of measuring the potential generated within the formation penetrated by the borehole. The tool uses a surface reference electrode N (fig. 2.8) and an inhole electrode M. The potential of the reference elctrode is constant so the variation in recorded voltage as the electrode M moves along the borehole are the variations in the spontaneous potential. The natural potential within rocks may be attributed to three principal mecahnisms: electrokinetic, liquid-junction and mineralization potential. The causes of these mechanism are discussed in the following sections.

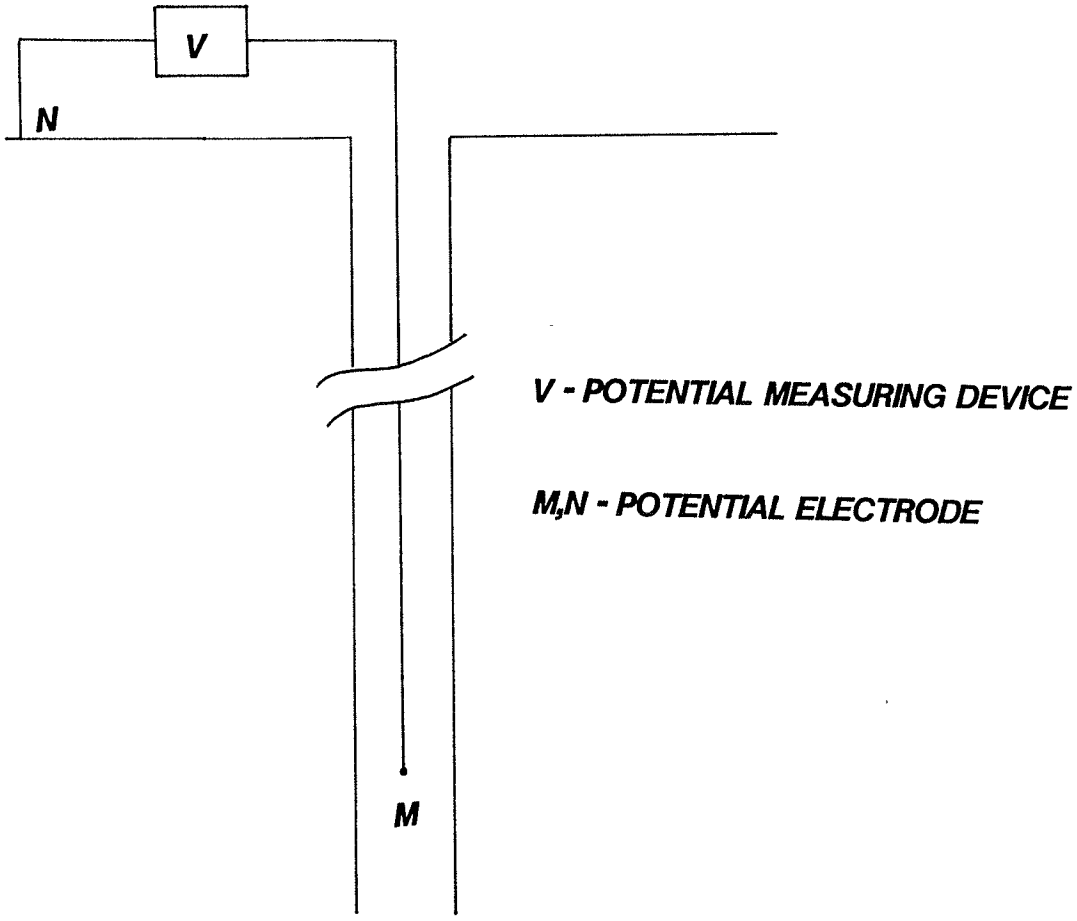

Figure 2.8: Schematics of spontaneous potential logging tool.

2.2.1 Electrokinetic Potential.

Electrokinetic potential are generated by the filtration of the fluid into the pores of the rocks.

Review of Theory.

Consider a liquid of viscosity η and electrical resistivity ρ flowing under a pressure difference Δp with a velocity v through a capillary with a raduis r and length l. The electrokinetic potential is given as(Dakhnov, 1962)

$$E = \frac{\epsilon \xi \rho \Delta p}{4 \eta l} \qquad 2.2.1-1$$

where ϵ is the dielectric constant of the liquid; ξ is the difference in potential between the fixed and mobile layers of liquid or the zeta potential. Hence, the electrokinetic potential is directly proportional to the dielectric constant, the resistivity of the solution, the zeta potential and the resultant pressure, and inversely proportional to the viscosity of the liquid. The polarity of the electrokinetic potential is controlled by the polarity of the zeta potential and the pressure drop. The magnitude of the zeta potential is determined by the properties of the adsorbed ions. Not enough is presently known about the behavior of ρ, ξ and η in the pores of rocks to allow direct calculation of the electrokinetic potential but the factors affecting the electrokinetic coupling, $E/\Delta p$, has been investigated. Tuman(1963) obtained $E/\Delta p$ values of about 150mV/atm to

390mV/atm using 500Ω-m distilled water in porous sandstone, and about 15mV/atm using 4.4Ω-m water. Ahmad(1964) obtained $E/\Delta p$ values in quartz sand ranging from 50mV/atm for 24Ω-m pore fluid to about 2400mV/atm for 2700Ω-m pore fluid. Ogilvy et al.(1969) found the value of the streaming potential to be considerably dependent on the permeability of the rock. This experiment also revealed that there is an optimum permeability value which yields a maximum streaming potential. In fractures, streamimg potential is believed to be the major contribution to the spontaneous potential anomally(Aguilera, 1980; Ogilvy et al. 1969). However, the factors affecting the origin in such zones are not yet clear.

2.2.2 Liquid-Junction Potential.

Liquid-juction potential is generated as a result of difference in mobilities of various ions in solution of different concentrations. Its value is given by(Telford et al., 1981)

$$E_L = \frac{G\theta(I_a - I_c)}{Fn(I_a + I_c)} \log(C_1/C_2) \qquad 2\cdot2\cdot2\text{-}1$$

where G is the gas constant(8.31 J/ C), F is the Faraday constant($9.65*10^4$ C/mol), θ the absolute temperature, n the valence, Ia and Ic the mobilities of the anions and cations respectively and C_1, C_2 the concentrations of the of the different solutions.

In sedimentary formation, liquid-junction potential is believed to develop at the interface between the fresh mud filtrate in the invaded zone and the saline formation water beyond the invaded zone; as a result of the greater mobility of the chloride anions over sodium cations, there is a net flow of chloride anions into the invaded zone. The detection of a significant liquid-junction potential in crystalline rocks has not been reported. This may be due to the fact such rocks normally contain very little fluid in their pore spaces to stimulate an appreciable liquid-junction anomally.

2.2.3 Mineralization Potential.

Mineralization potential is generated at the surfaces of minerals such as pyrite, pyrhotite, chalcopyrite, chalcocite, magnetite, covallite and graphite. The mechanism of generation is not completely understood but it is believed to be due to an oxidation-reduction reaction between the minerals and the oxygen in the borehole fluid.

2.2.4 Spontaneous Potential at the URL Site.

The mechanism of sponataneous potential formation in crystalline rocks has not been extensively investigated. It is therefore very hard to determine the precise nature of spontaneous potential anomaly. Bogoslosky and Ogilvy(1972), in a laboratory experiment simulated fractures by a system

of quartz glass plates and found out that a positive potential exists at small pressure gradients(0.003-0.03). With an increase in pressure gradient, large and negative potential values are observed. The absolute value of the potential decreases with the opening of the fracture.

Hydrogeologic investigation conducted at the URL site by Davison(1982) indicates that a hydraulic gradient of 0.003 exists in a highly permeable zone between boreholes URL-5 and URL-3 in the direction URL-5 to URL-3. Permeability values range from $1*10^{-12}$ cm/s for portions of the rock which contain no visible fractures to $1*10^{-3}$ cm/s for some highly fractured zones. Chemical analyses of groundwater samples from the URL site indicate that the water contain appreciable amounts of calcium, magnesium, sodium and chloride ions(Soonawala, 1982). When calcium and magnesium are present in dilute salt solutions a complex electrochemical phenomena results(Wyllie, 1957). They arise basically because of the great affinity of the clays in the borehole for divalent ions. Also core sample analysis indicates the presence of minor amounts of sulfides which might generate appreciable mineralization potentail. It is therefore possible that the spontaneous potential anomaly at the URL site is generated by a combination of the various process outlined above.

2.3 NEUTRON LOGGING.

The neutron log is used principally to delineate porous formations in hydrocarbon exploration. It employs a neutron source and either a gamma ray or a neutron detector. The neutrons emmitted by a source collide with the nuclei of the formation material, losing energy with each collision as they travel through the formation until their energy reach the thermal range and are captured. The nuclei which absorb the thermal neutrons becomes unstable and emits a gamma ray of capture. When the concentration of neutron capture materials in the formation is large, most of the thermal neutrons are captured within a short distance of the source; otherwise the thermal neutrons will travel farther from the source before being captured. Accordingly, the counting rate at the detector increases for decreased thermal neutron capture materials and vice versa. Depending on the type of detector, either the thermal neutrons or the emmited gamma rays are counted. In the following theoritical studies a gamma ray detector is assumed.

Review of Theory.

The basic principle behind the neutron log is the creation of a neutron flux by the neutron source in both the borehole and the formation. It is the neutron flux in the formation which generates the gamma rays counted by the detector. In this review the multi-group diffusion theory approach is followed.

This theory assumes a fast neutron point source and the neutrons are slowed down to thermal thermal energies. Figure 2.9 represents a theoretical borehole model for the neutron flux calculation. The inner cylinder represents a borehole of radius a containing water. The outer cylinder represents the effective radiated formation of radius b. Assume a point source of strength Q located at the origin of the r-z coordinate axes and a point detector D located at a distance z above the source. The height of the cylinders is assume to be 2h. The neutron balance equations for the two regions for the fast and thermal neutrons can be expressed as follows (Morse, 1977):

$$D_{1A} \nabla^2 \phi_{1A}(r,z) - \phi_{1A}(r,z) \Sigma_{1A} + S(r,z) = 0 \qquad 0 \le r \le a \qquad 2.3\text{-}1a$$

$$D_{2A} \nabla^2 \phi_{2A}(r,z) - \phi_{2A}(r,z) \Sigma_{2A} + \phi_{1A}(r,z) \Sigma_{1A} = 0 \qquad 0 \le r \le a \qquad 2.3\text{-}1b$$

$$D_{1A} \nabla^2 \phi_{1B}(r,z) - \phi_{1B}(r,z) \Sigma_{1B} = 0 \qquad a \le r \le b \qquad 2.3\text{-}1c$$

$$D_{2B} \nabla^2 \phi_{2B}(r,z) - \phi_{2B}(r,z) \Sigma_{2B} + \phi_{1B}(r,z) \Sigma_{1A} = 0 \qquad a \le r \le b \qquad 2.3\text{-}1d$$

where

S(r,z) = neutron source strength per unit volume.

D = diffusion coefficient.

= neutron flux

1 denotes fast neutrons.

2 denotes thermal neutrons.

A denotes the borehole region containing water

B denotes the effective irradiated formation

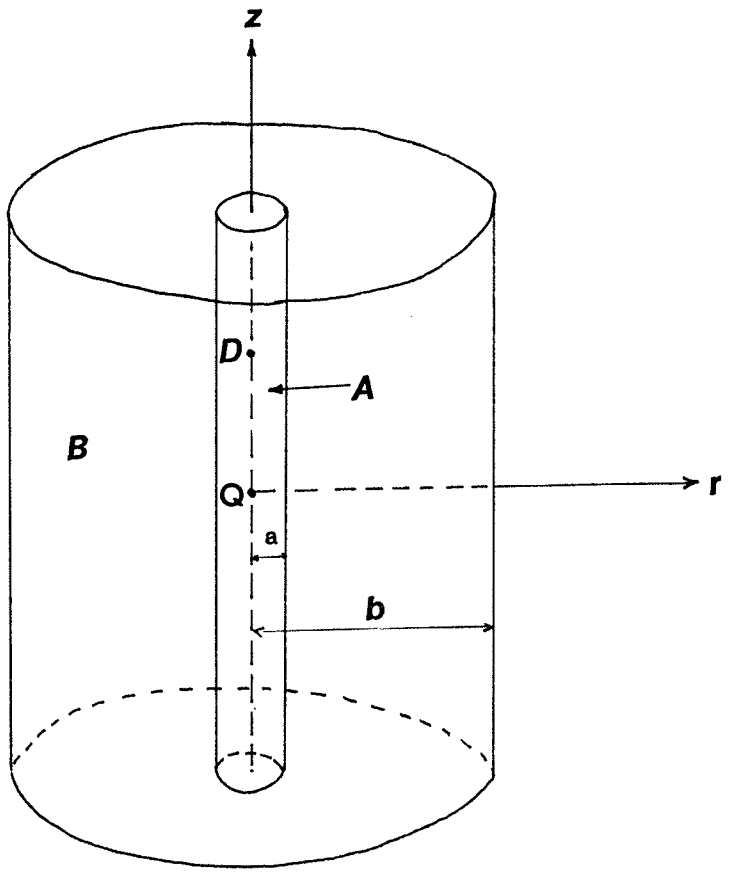

B - EFFECTIVE RADIATED FORMATION

A - FLUID-FILLED BOREHOLE

b - RADIUS OF EFFECTIVE RADIATED FORMATION

a - RADIUS OF BOREHOLE

Q - NEUTRON SOURCE

D - DETECTOR

Figure 2.9: Theoretical model for neutron flux calculation.

∇^2 = Laplacian operator.

Σ_1 = macroscopic removal cross-section for fast to thermal energy

Σ_2 = macroscopic thermal absorption cross-section

The boundary conditions at r=a are

(i)The neutron flux must be continuous.

$$\phi_{1A} + \phi_{2A} = \phi_{1B} + \phi_{2B}$$

(ii)The current density must be continuous.

$$D_{1A}\phi_{1A} + D_{2A}\phi_{2A} = D_{1B}\phi_{1B} + D_{2B}\phi_{2B}$$

Title and Allen(1966) gave the solution of equation 2.3-1a through 2.3-1d as follows:

$$\phi_{1A} = \frac{Q}{4\pi D_{1A}}\left[\frac{\exp\left(-\sqrt{r^2+z^2}/L_{1A}\right)}{\sqrt{r^2+z^2}} + \frac{\exp\left(-\sqrt{r^2+(z-2h)^2}/L_{1A}\right)}{\sqrt{r^2+(z-2h)^2}}\right]$$

$$+ \frac{Q}{2\pi D_{1A}h}\sum\left(\frac{A_n}{B_n}\right)I_o(\alpha_n r)\cos(\lambda_n z) \qquad 2.3-2$$

$$\phi_{2A} = \frac{Mh}{2}\left[\frac{\exp\left(-\sqrt{r^2+z^2}/L_{2A}\right)}{\sqrt{r^2+z^2}} + \frac{\exp\left(-\sqrt{r^2+(z-2h)^2}/L_{2A}\right)}{\sqrt{r^2+(z-2h)^2}}\right.$$

$$\left. - \frac{\exp\left(-\sqrt{r^2+z^2}/L_{2A}\right)}{\sqrt{r^2+z^2}} + \frac{\exp\left(-\sqrt{r^2+(z-2h)^2}/L_{2A}\right)}{\sqrt{r^2+(z-2h)^2}}\right]$$

$$+ M\sum\left[\left(\frac{A_n}{B_n}\right)I_o(\alpha_n r) + \frac{C_n}{B_n S_4}I_o(B_n r)\right]\cos(\lambda_n r) \qquad 2.3-3$$

$$\phi_{1B} = \sum_n G_n K_o(\gamma_n r) \cos(\lambda_n z) \qquad 2\cdot3-4$$

$$\phi_{2B} = \sum_n L_n K_o(\delta_n r) \cos(\lambda_n z) + S_3 \phi_{1B} \qquad 2\cdot3-5$$

$$M = \frac{Q}{2\pi D_{2A} h}\left(\frac{L_{2A}^2}{L_{1A}^2 - L_{2A}^2}\right) \quad ; \quad B_n = \frac{Q}{2\pi D_{1A} h}$$

where

$$S_3 = \frac{D_{1B} L_{2B}^2}{D_{2B}(L_{1B}^2 - L_{2B}^2)} \qquad S_4 = \frac{D_{1A} L_{2A}^2}{D_{2A}(L_{1A}^2 - L_{2A}^2)}$$

$$L_{1A} = \left[D_{1A} / \Sigma_{1A}\right]^{1/2} \qquad L_{2A} = \left[D_{2A} / \Sigma_{2A}\right]^{1/2}$$

$$L_{1B} = \left[D_{1B} / \Sigma_{1B}\right]^{1/2} \qquad L_{2B} = \left[D_{2B} / \Sigma_{2B}\right]^{1/2}$$

$$\gamma_n = \left[\lambda_n^2 + L_{1A}^{-2}\right]^{1/2} \qquad \alpha_n = \left[\lambda_n^2 + L_{1A}^{-2}\right]^{1/2}$$

$$\delta_n = \left[\lambda_n^2 + L_{2B}^{-2}\right]^{1/2} \qquad \beta_n = \left[\lambda_n^2 + L_{2A}^{-2}\right]^{1/2}$$

$$\lambda_n = n\pi/2h \qquad n = 1, 3, 5$$

and

$$A_n = \left[\frac{D_{1A}\alpha_n a K_o(\gamma_n a) K_1(\alpha_n a) - D_{1B}\gamma_n a K_1(\gamma_n a) K_o(\alpha_n a)}{D_{1A}\alpha_n a K_o(\gamma_n a) I_1(\alpha_n a) + D_{1B}\gamma_n a K_1(\gamma_n a) I_o(\alpha_n a)}\right] B_n$$

$$G_n = \left[\frac{(A_n / B_n) I_o(\alpha_n a) + K_o(\alpha_n a)}{K_o(\gamma_n a)}\right] B_n$$

$$L_n = \frac{S_4 B_n}{K_0(\delta_n a)}\left[\left(\frac{C_n}{B_n}\right)\frac{1}{S_4} I_0(\beta_n a) - K_0(\beta_n a) + (1-P)K_0(\gamma_n a)\left(\frac{G_n}{B_n}\right)\right]$$

$$C_n = \frac{R \cdot B_n \cdot S_4}{D_{2A}\beta_n a I_1(\beta_n a)K_0(\delta_n a) + D_{2B}\delta_n a K_1(\delta_n a) I_0(\beta_n a)}$$

in which

$$R = D_{2B}\delta_n a K_1(\delta_n a)\left[P\left(\frac{G_n}{B_n}\right)K_0(\gamma_n a) + K_0(\beta_n a) - K_0(\alpha_n a)\right.$$

$$\left. - \left(\frac{A_n}{B_n}\right) I_0(\alpha_n a)\right] - K_0(\delta_n a)\left\{ D_{2A}\gamma_n a P\left(\frac{G_n}{B_n}\right) K_1(\gamma_n a)\right.$$

$$\left. + D_{2A}\left[\beta_n a K_1(\beta_n a) - \alpha_n a\left\{K_1(\alpha_n a) - \left(\frac{A_n}{B_n}\right) I_1(\alpha_n a)\right\}\right]\right\}$$

$$P = D_{1A} D_{2A} L_{2B}^2 \left(L_{1A}^2 - L_{2A}^2\right) / D_{2B} D_{1A} L_{2A}^2 \left(L_{1B}^2 - L_{2B}^2\right)$$

$I_0(\alpha_n a)$, $K_0(\alpha_n a)$ = **Bessel function of zero order**

$K_1(\alpha_n a)$ = **Bessel function of first order**

Equation 2.3-5 is the expression for the thermal neutron flux distribution in the formation. These are the neutrons responsible for the generation of the gamma rays. The magnitude of the equation 2.3-5 is determined by the slowing down length of the fast neutrons in the borehole L_{1A} and in the formation L_{1B}, the thermal neutron diffusion lengths in the borehole L_{2A} and in the formation L_{2B}. The slowing down length of the fast neutron is determined by the concentration of light elements. The amount of energy lost per collision is inversely proportional to the relative mass of the nucleus with which the neutron collides. The greatest energy loss however occurs when the neutron strikes a nucleus of practically equal mass i.e hydrogen. Hence L_{1B} is principally dependent on the amount of water in the formation. As a result of successive collisions the neutrons are slowed down to thermal energies(0.025eV). They then diffuse randormly without lossing any more energy until they are captured. The distance travelled by the thermal neutrons before capture, which is called thermal neutron diffusion length, is therefore determined by the amount of thermal neutron absorbing elements in the formation. Table 1 gives the netron capture cross-section for some of the commonly occuring elements in the granite.

TABLE 1

Neutron capture cross-section for some common elements in granite(Telford et al. 1981).

ELEMENT	CROSS-SECTION(BARNS)
HYDROGEN	0.330
OXYGEN	0.002
SODIUM	0.530
MAGNESIUM	0.270
ALUMINIUM	0.230
SILICON	0.160
POTASSIUM	2.100
CALCIUM	0.430
IRON	2.600

In sedimentary formation, the neutron log is primarily responsive to the hydrogen nuclei contained in shales and in the rock pore system. These hydrogen nuclei determine both the fast neutron slowing down length as well as the thermal neutron diffusion lengths. The log therefore measures the porosity of the formation. In granite the situation is different. Since the amount of water in the pore spaces is extremely small, the slowing down of the fast neutrons will be controlled by other light elements such as oxygen and sodium in the granite. Also, compared to hydrogen, elements such as sodium, potassium and iron all have a greater neutron capture probability and it is possible that their contribution to the total emmited gamma rays reaching the detector may be greater than the gamma rays due to the hydrogen in the formation. It is therefore obvious that the response of the neutron log in granite should not be interpreted only in terms of porosity. The effect of thermal neutron absorbing materials must also be taken into account.

The response of the neutron log at a fracture zone may be determined by the nature of the infilling materials and the ground water flowing through. For water saturated fractures, the neutrons would be slowed down and captured within a short distance due to the high concentration of hydrogen nuclei. The depth of investigation in this case will be very shallow. For closed fractures a determining factor may be the thermal neutron absorbing capacity of the fracture infilling material.

2.4 DENSITY LOGGING.

The density log measures the formation density. The tool consists of an energy source which is either cobalt 60 or cesium 137 and two detectors(fig. 2.10). The long-spaced combination measures deeper into the formation whereas the shorter spaced set up is more influenced by mud cake and other materials that exists between the tool and the formation. The use of two detectors is so that a correction for the effect of the borehole fluid can be made. The source emits medium-energy gamma rays which undergo compton scattering as a results of collision with the formation electrons. The source and the detector are so designed that the tool response is predominanatly due to this phenomenon. The scattered gamma rays reaching the detector at a fixed distance from the source, are counted as an indication of the formation density.

Interaction of Gamma Rays with matter.

Gamma rays interact with matter through three main processes. These are:

a) Photoelectric effect.

The gamma ray losses all of its energy to a bound atomic electron. Part of the energy is used to overcome the binding forces to an atom and the remainder appears as the kinetic energy of the electron. For the main rock-forming elements, that is elements with atomic numbers between 1 and

20, photoelectric absorption is the dominating factor in the low energy range (less than 0.02MeV)(Danes, 1960).

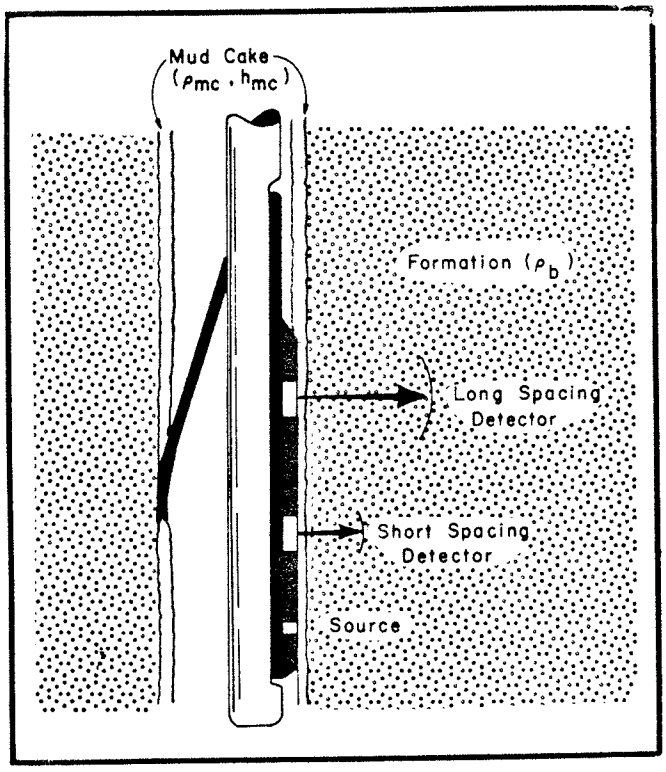

Figure 2.10: Schematics of density logging tool(After Schlumberger, 1972).

b) Compton scattering.

The gamma ray is deflected in its path by the atomic electrons of the formation and continues to travel with a reduced energy. This the dominating process for gamma energy of about 1MeV.

c) Pair production

The gamma ray is annihilated near a nucleus or electron while creating an electron-positron pair. The energy required for the process is greater than the rest energy of the pair. Since the electron rest mass is 0.51MeV, pair production cannot take place unless the gamma ray energy originally was larger than 1.02MeV. At about 10MeV, pair production is the same order of magnitude as compton scattering and at 100MeV it becomes the dominating factor (Danes, 1960). Hence it is essentially a high energy process.

Review of Theory.

The migration of gamma rays through a formation can be studied by the stationary-state Boltzmann transport equation. This equation of continuity expresses the equilibrium existing in a six-dimensional photon phase space of volume element $d\tau \equiv dV d\Omega dE$. A phase space is a six-dimensional space whose coordinates are the three ordinary space coordinates(x,y,z) and the corresponding three components of the momentum. For a photon in a homogeneous medium, Tittman and

Wahl(1964) gave the expression for the number of photons per unit energy interval and per unit solid angle crossing a unit area having its normal in the direction Ω at a distance r per unit time $F(r,\Omega,E)$ as

$$\Omega\cdot\nabla F(r,\Omega,E) + \Sigma_T(E)F(r,\Omega,E) = \int_{\Omega'}\int_{E}^{E_0} F(r,\Omega',E')\,\Sigma_s(\Omega'\rightarrow\Omega, E\rightarrow E')\,dE'd\Omega' + S(r,\Omega,E)$$

2·4−1

Here E is the gamma ray energy, Σ_T the total macroscopic interaction cross section of the medium at energy E, $S(r,\Omega,E)$ the distribution of photon sources in phase space, Σ_s is the macroscopic cross section for scattering from the direction Ω' into Ω and simultaneously from energy E′into E. The first term accounts for the transport loss rate of photons from a volume element dV in configuration space, and the second accounts for the collision loss rate from a photon phase space of volume $d\tau \equiv dV d\Omega dE$. The integral expression is a measure of the rate at which photons from all points in phase space are scattered into $d\Omega\,dE$; and $S(r,\Omega,E)$ is the initial rate of photons in $d\tau$. To obtain an expression for the current density per unit area, equation 2.4-1 is integrated over Ω. This gives(Tittman and Wahl, 1964)

$$\nabla\cdot j(r,E) + \Sigma_T(E)f(r,E) = \int_{E}^{E_0} f(r,E')\,\Sigma_s(E'\rightarrow E)\,dE' + S(r,E)$$

2·4−2

here $f(r,E) \equiv \int_{\Omega} F(r,\Omega,E)d\Omega$ is the number of photons per unit time in dE crossing the surface of a sphere of unit cross section at r and $j(r,E) \equiv \int_{\Omega} F(r,\Omega,E)d\Omega$ is the current density. An approximate solution to equation 2.4-2 can be obtained by integrating over E. This gives(Tittman and Wahl, 1964)

$$\nabla \cdot J(r) + \int_0^{E_0} f(r,E')\,\Sigma_a(E')\,dE' = S(r) \qquad 2.4\text{-}3$$

where

$$J(r) \equiv \int_0^{E_0} j(r,E)\,dE$$

and

$$S(r) \equiv \int_0^{E_0} S(r,E)\,dE$$

If it is assumed that f(r,E) is seperable into a function of distance, $f_1(r)$ and a function of energy, $f_2(E)$, then

$$f(r,E) = f_1(r)\,f_2(E) \qquad 2.4\text{-}4$$

and if Fick's law holds,

$$J = -D\nabla f_1(r) \qquad 2.4\text{-}5$$

then equation 2.4-3 reduces to a stationary-state diffusion equation(Tittman and Wahl, 1964).

$$\nabla^2 f_1(r) - \frac{\langle \Sigma_a \rangle}{D} f_1(r) = \frac{S(r)}{D} \qquad 2.4\text{-}6$$

or $$\nabla^2 f_1(r) - \frac{f_1(r)}{L^2} = -\frac{S(r)}{L} \qquad 2.4-6b$$

here $\langle \Sigma_a \rangle \equiv \int_0^{E_0} f_2(E)\Sigma_a(E)dE$ is the macroscopic absorption cross section averaged over the energy spectrum of the flux such that $f_1(r)\langle \Sigma_a \rangle$ is the total absorption rate per unit volume at r, and $L = \sqrt{D/\langle \Sigma_a \rangle}$ is the diffusion length and D is the diffusion constant. The solution of equation 2.4-6b is of the form(Tittman and Wahl, 1964)

$$f_1(r) = \frac{S}{D} \cdot \frac{e^{-r/L}}{4\pi r} = \frac{S}{D} \cdot \frac{e^{-\frac{r\rho_B}{K}}}{r} \qquad 2.4-7$$

where $L = K/\rho_B$, and ρ_B is the formatiom density and K is a constant of proportionality. Equation 2.4-7 describes the qualitative properties of most density logging tools; that there is an approximate exponential dependence of the tool response on the bulk formation density. This relation is the basis of operation of the density log.

The total cross-section for the interaction of gamma rays with matter include all processes by which gamma rays are lost from a beam on transmission through matter. It is defined by(Danes,1960)

$$I = I_0 e^{-\sigma_t x} \qquad 2.4-8$$

where I is the gamma intensity after traversing an absorber of thickness x. The total cross-section is made up of components due to photoelectric effect σ_{PE}, compton scattering

σ_{cs} and pair production σ_{pp} .ie

$$\sigma_t = \sigma_{p\bar{e}} + \sigma_{cs} + \sigma_{pp} \qquad 2.4-9$$

In density logging the source energy is about 1MeV, sufficiently low enough to effectively eliminate pair production and the scintillating detectors are set so that they do not see gamma rays with energies that significantly are affected by photoelectric effect. The most dominant process therefore is compton scattering and the total cross-section equals the compton scattering cross-section. Since this phenomenon occurs on the orbital electrons, the intensity of the scattered radiation reaching the detector is a measure of the electron density E_d of the formation. The relation between the electron density E_d and the bulk density ρ_b is given by Tittman and Wahl(1964) as

$$E_d = N_o \left(Z/A \right) \rho_b \qquad 2.4-10$$

where N_0 is Avogadro's number($6.03*10^{23}$ per mole) and (Z/A) the ratio of the number of electrons per atom(or molecule) to the atomic(or molecular) weight which is assumed to be 0.5. For most reservior rock types for example limestone, dolomite and sandstone, Z/A is close to 0.5 and the relation between bulk density and electron density is apparently the same. Errors are introduced if the Z/A ratio differ significantly from the assumed value. For water, this difference is very significant but since most commercial logs are calibrated in a water filled limestone, the error is removed. The Z/A ratio for some of minerals identified by core analy-

sis in the URL is shown in Table 2. Even though the error produced by ignoring the Z/A effect may be very small, their effect in quantitative gravity analysis may be appreciable. This error may be corrected if the chemical composition of is accurately known. Perharps the best procedure to correct these errors is to utilized density values from core analysis. Another phenomenon that might introduce error is the gamma rays produced by the natural radioactivity of granite. Potassium(K40) which occurs in potash feldspar as a major component of granite, emits gamma rays of a single energy of 1.46MeV and the radioactive elements of the uranium and the thorium series, which occur in accessory minerals, emit many gamma rays of energies up to 3MeV. These gamma rays experience compton-scattering collision as they travel through the formation and the scattered rays would add up to the total gamma rays at the detector. Since the intensity of gamma radiation is very high for granite these secondary scattered gamma rays may far exceed those generated by the induced source. The effect of these naturally occuring gamma rays may however be eliminated by taking the difference of the readings at the two detectors.

From the above analysis, it clear that the response of the density log in fractured zones will depend on the electron density of the fracture infilling materials. Heavy elements because of their large electron density will generate increased gamma count at the detector. Fluid saturated

fractures would generate low gamma counts due the light elements, hydrogen and oxygen.

2.5 SONIC LOGGING

In sonic logging, the travel times of acoustic waves over a specified formation interval is measured. The reciprocal of this gives the velocity of the formation within that interval. There are essentially four types of seismic waves propagating in fluid-filled borehole: two (P and S) headwaves and two quided waves. The first of the head waves begins as a compressional P wave in the borehole fluid. It undergoes a critical refraction into the formation as a P wave and then is refracted back into the fluid as a compressional wave. The other head wave begins as an S wave provided the shear wave velocity of the formation is higher than the compressional velocity of the borehole The quided wave include reflected conical wave(Biot, 1952) or pseudo-Rayleigh waves(Cheng et al. 1981). This wave decays radially away from the borehole wall in the solid and is oscillatory in the fluid. It has a phase velocity bounded by the shear velocity of the formation and the compressional wave velocity of the fluid. The group velocity has an upper bound which is the shear velocity of the formation. The other quided wave is a tube wave which propagates along the borehole wall. Its amplitude decays exponentially away from both sides of the fluid/formation interface.

TABLE 2

Z/A ratio for some of the common minerals in granite

MINERALS	Z/A
CALCITE	0.49956
WATER	0.55506
LIMONITE	0.48732
CHLORITE	0.50370
QUARTZ	0.49925
BIOTITE	0.49288
ORTHOCLASE	0.49560
ALBITE	0.49570
OLIGOCLASE	0.49620

The pressure response in a fluid filled borehole at an axial distance z and radial distance r due to a point source (fig. 2.11) is given by (Tsang and Rader, 1979).

$$P(r,z,t) = \frac{i P_0 R_0}{4\pi} \int_{-\infty}^{\infty} X(\omega) e^{-i\omega t} d\omega \int_{-\infty}^{\infty} A J_0(k_r r) e^{ikz} dk \qquad 2\cdot5\text{-}1$$

where P_0R_0 is the amplitude related to the source, ω is the angular frequency, $X(\omega)$ is the source spectrum, J_0 is the Bessel function of the zeroth order, k is the wavenumber in the z direction, k_r is the wavenumber in the radial direction in the fluid given by

$$k_r^2 = \frac{\omega^2}{\alpha_f^2} - k^2$$

and A is given by

$$A = \frac{f_1 k_r a H_1^{(1)}(k_r a) + f_2 H_0^{(1)}(k_r a)}{f_1 k_r a J_1(k_r a) + f_2 J_0(k_r a)}$$

where

$$f_1 = \mu_m \left[\frac{2k_s^2}{a^2} - \frac{(k_s^2 - 2k^2) H_0^{(1)}(k_r^{(c)} a)}{k_r^{(c)} a H_1^{(1)}(k_r^{(c)} a)} - \frac{4k^2 k_r^{(s)} H_0^{1}(k_r^{(s)} a)}{a H_1^{(1)}(k_r^{(s)} a)} \right]$$

and

$$f_2 = \frac{K_f \omega^2 k_s^2}{\alpha_f^2}$$

with

$$k_r^{(c)} = (k_c^2 - k^2)^{1/2} \quad , \quad k_r^{(s)} = (k_s^2 - k^2)^{1/2}$$

$$k_c^2 = \frac{\omega^2}{\alpha_m^2} \quad , \quad k_s^2 = \frac{\omega^2}{\beta_m^2}$$

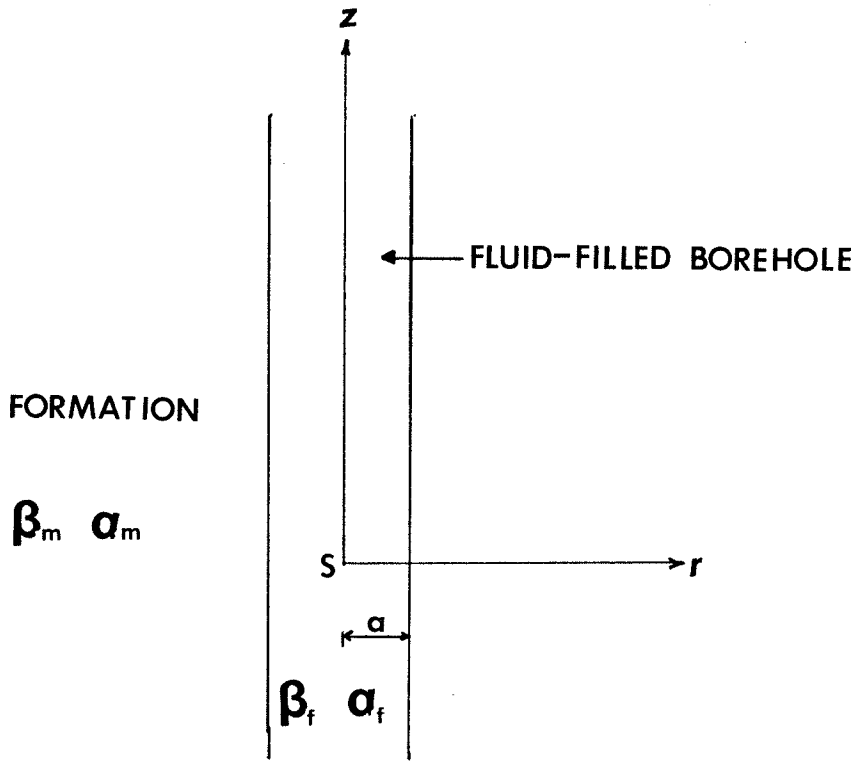

α_f – *P WAVE VELOCITY OF FLUID*

β_f – *S WAVE VELOCITY OF FLUID*

α_m – *P WAVE VELOCITY OF FORMATION*

β_m – *S WAVE VELOCITY OF FORMATION*

a - RADIUS OF BOREHOLE

S - SOURCE

Figure 2.11: Configuration for elastic waves in borehole.

where μ_m, α_m and β_m are the shear modulus, P and S wave velocity of the formation respectively, K_f and α_f are the bulk modulus and P wave velocity of fluid respectively, $H_0(k_r^c a)$ is a zeroth-order Hankel function and $H_1(k_r^s a)$ is a first-order Hankel function. Equation 2.5-1 generates all the four types of waves listed above. Using numerical techniques, Paillet and White(1982) were able to seperate the various componets and analyzed them to gain further insight into the physical mechanism that control the propagation of these waves. Power spectrum analysis revealed that both normal modes and head waves are influenced by the presence of laterally confined fluid in the borehole.

In sonic logging it is only the compressional headwave which is monitored. The theoretical predicted arrival time is simply given as

$$t_c = \frac{Z}{\alpha_m} + \frac{2a \cos\theta_c}{\alpha_f} \qquad 2.5-2$$

where

$$\theta_c = \sin^{-1}(\alpha_f/\alpha_m)$$

The interval time Δt, is the difference in arrival times between two receivers z apart for the same portion of the compressional waveform and it related to the velocity of the formation between the two receivers by the relation

$$\frac{1}{\Delta t} = V_m = \sqrt{\frac{K_m + (4/3)\mu_m}{\rho_m}} \qquad 2.5-3$$

where K_m and ρ_m are the bulk modulus and density of the formation respectively. Hence, the interval transit time is related to the elastic properties of the formation.

The presence of fractures would affect the elastic properties of the medium even though the fractional volume occupied by the fractures may be extremely small. Hajnal et. al.(1983) found in borehole measurements carried out under low lithostatic stress condition that the ratio $(VF/VL)^2$ where VF and VL are the in-situ velocity and intact rock velocity respectively, decrease linearly with increasing fracture frequency. This suggests that the compressional wave transit time may be used as a measure of fracture frequency.

2.5.1 Elastic Moduli and Seismic Velocities for Fracture Zones.

O'Connell and Budiansky (1974) used a self-consistent approximation to calculate the effective elastic moduli of solid permeated with isotropic distribution of flat fractures(cracks) from the energy of a single fracture. In the self-consistent energy approach, the isothermal potential energy, $\underline{\Phi}$, of the unfractured body, is related to the isothermal potential energy, $\bar{\underline{\Phi}}$, of the fractured body by

$$\bar{\underline{\Phi}} = \underline{\Phi} + \Delta\underline{\Phi} \qquad 2.5.1\text{-}1$$

where $\Delta\underline{\Phi}$ is the potential energy change due to insertion of fractures. Approximate values of the effective elastic

constants of the fractured body is obtained by means of plausible estimates for various loading conditions. The fracture(crack) density is defined as

$$\epsilon = \left(\frac{2N}{\pi}\right)\left\langle \frac{A^2}{P}\right\rangle \qquad 2.5.1-2$$

where A and P are the fracture area and perimeter respectively, and N is the number of fractures per unit volume. For a circular fracture of radius s, this reduces to

$$\epsilon = N\langle S^3\rangle \qquad 2.5.1-3$$

It has been shown by O'Connell and Budiansky (1974) that the static elastic moduli of a fluid-saturated fractured solids are nearly independent of the shape of the fractures as long as the fractures are defined as in equation 2.5.1-2. Hence only circular fractures will be considered with the understanding that the results may be used for fractures of other shapes. O'Connell and Budiansky(1974) estimated the effective elastic constants for a fractured body under different physical conditions. For dry fractures or fliud-filled fractures in which there is a bulk flow of fluid out of, or into, fractures resulting from changes in fluid pressure in the fractures, the effective elastic moduli are given by O'-Connell and Budiansky(1977) as

$$\frac{\bar{K}}{K} = 1 - \frac{16}{19}\left(\frac{1-\bar{\nu}^2}{1-2\nu}\right)\epsilon \quad , \quad \frac{\bar{G}}{G} = 1 - \frac{32}{45}\frac{(1-\bar{\nu})(5-\bar{\nu})}{(2-\bar{\nu})}\epsilon$$

$$\bar{\nu} = \nu + \frac{32}{45}\frac{(1-\bar{\nu}^2)(1-2\nu)}{(2-\bar{\nu})}\epsilon \qquad 2.5.1-4$$

where $\bar{K}$, $\bar{G}$ and $\bar{\nu}$ are the bulk modulus, rigidity and Poisson's ratio of the fractured material; and K, G and ν are the corresponding parameters for the unfractured matrix. For fluid saturated fractures in which shear stresses in the fluid relax completely, but no fluid is able to flow out of any of the fractures:

$$\frac{\bar{K}}{K} = 1 \quad ; \quad \frac{\bar{G}}{G} = 1 - \frac{32}{15}\left(\frac{1-\bar{\nu}}{2-\bar{\nu}}\right)\epsilon$$

2.5.1-5

$$\bar{\nu} = \nu + \frac{32}{45}\cdot\frac{(1-\bar{\nu}^2)(1-2\nu)}{(2-\bar{\nu})}\cdot\epsilon$$

The changes in fluid pressure may not be the same in every fracture. This case is known as 'saturated-isolated'. For the case of partial saturation, O'Connell and Budiansky(1974) gave the fracture density as

$$\epsilon = \frac{45}{16}\cdot\frac{(\nu-\bar{\nu})}{(1-\bar{\nu}^2)}\cdot\frac{(2-\bar{\nu})}{\left[(1-s)(1+3\nu)(2-\bar{\nu}) - 2(1-2\nu)\right]}$$

2.5.1-6

where s is the saturation fraction. The effective elastic moduli are

$$\frac{\bar{K}}{K} = 1 - \frac{16}{19}\,\frac{(1-\bar{\nu}^2)(1-s)}{(1-2\nu)}\,\epsilon$$

2.5.1-7

$$\frac{G}{G} = 1 - \frac{32}{45}\cdot(1-\bar{\nu})\left[1 - s + \frac{3}{2-\bar{\nu}}\right]\epsilon$$

There is an additional case which is intermediate between the 'saturated isolated' and the 'dry' case. If all the fractures are in communication with each other, but no fluid flow is permitted out of the bulk regions of the sample, the effective bulk moduli will be the same as for the 'saturated-isobaric' case but the fractured material will respond in shear as if the fractures were dry. This case is known as 'saturated-isobaric' and the effective elastic parameters are given by O'Connell and Budiansky(1977) as

$$\frac{\bar{K}}{K} = 1 \quad , \quad \frac{\bar{G}}{G} = 1 - \frac{32}{45}\frac{(1-\nu')(5-\nu')}{(2-\nu')}\epsilon \qquad 2.5.1-8$$

where

$$\nu' = \nu - \frac{16}{45}\frac{(1-\nu'^2)(10\nu - 3\nu\nu' - \nu')}{(2-\nu')}\epsilon$$

here ν has been changed to ν' because it is no longer the effective Poisson's ratio of the bulk material. The effective Poisson's ratio for the bulk material is

$$\bar{\nu} = \frac{(1+\nu)\bar{K}/K - (1-2\nu)\bar{G}/G}{2(1+\nu)\bar{K}/K + (1-2\nu)\bar{G}/G} \qquad 2.5.1-9$$

The seismic velocities within the fractured material for any particular case is given by

$$\bar{V}_s = V_s\left(\frac{\bar{G}}{G}\right)^{1/2} \quad , \quad \bar{V}_p = V_p\left[\frac{(1-\bar{\nu})(1+\nu)}{(1+\bar{\nu})(1-\nu)}\cdot\frac{\bar{K}}{K}\right]^{1/2}$$

$$2.5.1-10$$

The transition between the cases described above involve the relaxation of the shear stresses in a viscous fluid and the flow of a viscous fluid in a permeable medium. These effects are described by O'Connell and Budiansky(1977) in terms of linear viscoelasticity. The results are represented as frequency dependent effective moduli, which are appropriate for sinusoidal variation of stress and strain. For fluid-saturated fractures, the effective moduli in equation 2.5.1-7 are modified to

$$\frac{\bar{K}}{K} = 1 \quad , \quad \frac{\bar{G}}{G} = 1 - \frac{32}{45}\left(\frac{1-\nu'}{2-\nu'}\right)\left[(2-\nu')D + 3C\right]\epsilon$$

2.5.1-11

where ν' is the root of

$$\nu' = \nu + \frac{16}{45}\left(\frac{1-\nu'^2}{2-\nu'}\right)\left[2(1-2\nu)C - (2-\nu')(1+3\nu)D\right]\epsilon$$

where

$$D = \left[-id\omega_1/\omega\right] \Big/ \left[1 - id\omega_1/\omega\right]$$

with

$$d = \frac{9}{16}\left(\frac{1-2\nu}{1-\nu}\right)\frac{1}{1-\nu'} \cdot \frac{\bar{G}}{G}$$

and

$$C = \left[-ie\omega_2/\omega\right] \Big/ \left[1 - ie\omega_2/\omega\right]$$

with

$$e = \frac{\pi}{4}\left(\frac{2-\nu'}{1-\nu'}\right)\frac{\bar{G}}{G}$$

where ω_1 and ω_2 are the characteristic frequencies. For closely spaced fractures having many intersection:

$$\omega_1 \simeq \left(\frac{K}{\eta}\right)\left(\frac{c}{a}\right)^3 \quad , \quad \omega_2 \simeq \left(\frac{G}{\eta}\right)\left(\frac{c}{a}\right) \qquad 2.5.1\text{-}12$$

where c/a is the aspect(thickness to diameter) ratio of the fracture, ω_1, the characteristic frequency for the flow of fluid between fractures corresponding to the transition from 'saturated-isolated' to 'saturated-isobaric', and w_2, the characteristic frequency for the relaxation of shear stress in the viscous fluid in the fracture, which corresponds to the transition from the 'glue' case in which fractures have no effect on the moduli to the 'saturated isolated' case. For water saturated thin fractures, seismic and laboratory elastic wave velocities correspond to a state ranging between 'saturated-isobaric' at frequencies in and below seismic range and 'saturated-isolated' at high frequencies(O'Connell and Budiansky, 1977).

2.6 SOME IMPLICATIONS FOR VSP.

Even though in sonic logging, the emphasis is on the compressional wave transit time, studies have indicated that it is not as sensitive to the presence of fracture as the amplitude of the other modes of wave propagation. While the velocity of the shear wave is not significantly affected by the presence of water its amplitude is greatly attenuated. Gratsinskiy et al.(1968), in a laboratory experiment, simulated fractures with gaps in a steel block and found out

that the shear wave attenuation was greater than that of the compressional wave and also the amount of attenuation increased with fracture opening. The water in fractures reduces the friction coefficient which exist within the fractures, facilitating relative sliding across fracture surfaces and thus increasing the attenuation(Johnston et al.,1979). Paillet and White(1982) studied the acoustic modes in a borehole and demonstrated that the amplitude associated with shear and tube wave anomalies could all be used to recognize hydraulically significant fractures. Amplitude logs that are constructed for wells penetrating fractured formation and a qualitative estimation of effective fracture width on the acoustic borehole televiewer log, suggest that tube wave amplitude deflection is roughly proportional to total fracture aperture.

Vertical seismic profiling affords an unique opportunity to study the seismic wave attenuation, since the measurement allows a propagating seismic wavefront to be analyzed in real earth conditions. Hauge(1981) used the spectral ratio method to extract attenuation information from VSP data. In the this method, seismic wave attenuation is assumed to be a linear function of frequency. This relation can be expressed as

$$A_2(f) = G_z A_1(f) e^{-\beta_z f} \qquad 2.6-1$$

where f is the frequency, G_z is a frequency independent factor that accounts for the amplitude effects such as

spherical divergence, variations in recording gain, changes in source and receiver couplings; A_1 and A_2 are the amplitude spectra of the downhole pulse recorded at depths Z_1 and Z_2 respectively. The exponent, B_z, is the cumulative seismic wave attenuation between the depths Z_1 and Z_2. Measurements obtained from different stratigraphic areas indicate a strong dependence of attenuation on lithology. Since the amplitude of both the compressional and shear are attenuated by fractures, this suggests that attenuation measurements may be a valid parameter for mapping fracture zones.

VSP also permits accurate measurements of the amplitude associted with shear and tube wave anomalies.

2.7 GAMMA LOGGING.

The gamma log measures the 'natural' gamma-ray emission of the formation. These gamma-rays originate in the spontaneous disintergration of atoms of potassium-40 and the radioactive substances formed during the decay of uranium and thorium series elements. The detector, which is either a Geiger counter or a scintillation meter is lowered into the borehole and the pulses generated as the gamma rays enter the detector are countered. In sedimentary formation the gamma-log normally reflects the shale content. This is because the radioactive elements tend to concentrate in clays and shales. Of the common rock types, granite has the highest concentration of potassium, uranium and thorium.

Granite would therfore have a very high intensity of gamma radiation. For an unaltered granite, the potassium content would be quite constant because potassium is related to the content of potash feldspar which is a relatively constant major component of granite(Keys, 1979). Thorium and uranium on the other hand occur in accessory minerals and therefore may show considerable variation. Alteration of granite in fluid filled fractures may cause changes in the chemical composition of the rock. Alteration of felspars to zeolites have been noted(Keys, 1979). Also there is the possibility of uranium being preferentially concentrated in fractures because of its higher mobility under oxidizing ground-water conditions. These therefore suggest that the use of gamma-ray spectroscopy may provide a better means of locating fractures in granite. The conventional detectors record the total gamma count which might not show a considerable variation in granite.

Compared to the neutron log, the gamma log is less useful in detecting fluid-filled fracture zones in granite. The neutron log responds to the water in the fractures regardless to its chemical composition. On the contrary, the intensity of the gamma radiation for fliud-filled fractures depends on the level of radioactivity in the water which is controlled by chemical reactions such hydrothermal alteration and oxidation. When used in combination with the density log, the neutron log can be useful in identifying mineralized zones.

2.8 TEMPERATURE LOGGING.

The temperature log measures the ambient temperature in the borehole. The geothermal gradient Γ is related to the quantity of heat H flowing through the formation per unit time, the thermal resistivity τ of the formation and the temperature, T, in the borehole by the relation

$$\Gamma = \frac{dT}{dz} = H\tau \qquad 2.8-1$$

where $\frac{dT}{dz}$ is the geothermal gradient. Hence if thermal equilibrium exist in the borehole, the geothermal gradient is related to the lithologic changes in the formation.

Temperature logs can be used to detect permeable fracture zones. For small constant flow of water the temperature, but not the gradient will be disturbed by a constant amount(Birch, 1947). Fractures which are open to fluid flow may cause a temperature anomaly whose polarity will depend on whether the fluid flows out or into the borehole.

2.9 CALIPER LOGGING.

The caliper log uses a mechanical device with movable arms to measure the diameter of the borehole. The number of arms range from one to four. Normally, borehole are not always the same diameter as the drill bit but are often enlarged by fracturing and caving that results from chemical and mechanical reactions of the drillpipe and drilling fluid with the formation.

Caliper logs may be classified according to the area of contact against the formation and the number of arms. The area of contact between the arm and the formation determines the vertical resolution. The smaller arms have better vertical resolution. The number of arms on a caliper log, determines its response to the shape of the hole. Generally, the one and two armed caliper log measure the largest diameter of the hole at the point of contact. The hole diameter measured by the three and four armed caliper log is greater than the smallest diameter but less than the greatest diameter at the point of contact. Because it measures the diameter of a cavity, the caliper log may not detect closed fractures.

Chapter III

INTERPOLATION OF WELL LOG DATA.

Geophysical well log data are sometimes recorded at unequal spaced points but because most data processing techniques require the data points to be equally spaced, we resort to interpolation to convert the unequally spaced data into equally spaced data. There are a variety of interpolation methods but perhaps one of the simplest is the Lagrangian interpolation method. It is easy to to program because of the simplicity of its recursion formulae.

In this chapter, the Lagrangian interpolation method is reviewed. The error introduced by this method when applied to an unequally spaced well log data is also investigated.

3.1 LAGRANGIAN INTERPOLATION METHOD.

Suppose that we are given N+1 data pairs $(x_0 y_0)$, (x_1, y_1),.....$(x_N y_N)$ representing N+1 points of a function y=f(x) where the explicit form of f(x) is not known. The x_i (i=0,..,N) are assumed to be distinct values of the independent variable x. The Lagrangian polynomial $P_N(x)$ of maximum degree N which approximates y=f(x) over an interval I containing $x_0, x_1, ...x$ is given by Gerald(1980) as

$$P_N(x) = y_0 \frac{(x-x_1)(x-x_2)\cdots\cdots(x-x_N)}{(x_0-x_1)(x_0-x_2)\cdots\cdots(x_0-x_N)}$$

$$+ y_1 \frac{(x-x_0)(x-x_2)\cdots\cdots(x-x_N)}{(x_1-x_0)(x_1-x_2)\cdots\cdots(x_1-x_N)}$$

$$+ \cdots\cdots\cdots$$

$$+ y_K \frac{(x-x_0)(x-x_1)\cdots(x-x_{K-1})(x-x_{K+1})\cdots(x-x_N)}{(x_K-x_0)(x_K-x_1)\cdots(x_K-x_{K-1})(x_K-x_{K+1})\cdots(x_K-x_N)}$$

$$+ \cdots\cdots$$

$$+ y_N \frac{(x-x_0)(x-x_1)\cdots\cdots\cdots(x-x_{N-1})}{(x_N-x_0)(x_N-x_1)\cdots\cdots\cdots(x_N-x_{N-1})} \qquad 3.1-1$$

The error E(x) is given by Gerald(1980) as

$$E(x) = f(x) - P_N(x) = (x-x_0)(x-x_1)\cdots\cdots(x-x_N)\frac{f^{N+1}(I)}{(N+1)!} \qquad 3.1-2$$

where the interval I lies between the largest and the smallest of the x_i for the interpolation. The error depends upon both the signal and the data spacing. For a given data spacing, the upper and lower bounds on the error can only be estimated if we have information on the (N+1)st derivative of the actual function f(x). For well log data, precise determination of the actual function is not always possible and so it becomes impossible to estimate the interpolation error in a deterministic sense. For this reason, we would compare the original and interpolated well log data using different number of points for the interpolation, W(3,5,7,9,11). The unequal spaced x-values used for this

experiment was obtained from the sonic well log data. Here, the largest and the smallest sample intervals are 0.051m and 0.050m respectively.

3.2 RESULTS AND DISCUSSION.

The results of this analysis are shown in figures 3.1 and 3.2. The spacing of the interpolated points is 0.05 m. For W=3, there is no significant difference between the original and the interpolated data. On the contrary, there is a conspicuous difference between the original and the interpolated data for W=11. We also notice a number of oscillations in the interpolated data which appears to increase with an increasing number of points used for the interpolation.

Even though this analysis is rather subjective, it is obvious that the interpolation error would be larger for W=11. These results indicate that, in order to minimize the interpolation error, no more than five data points are required for acceptable interpolation results.

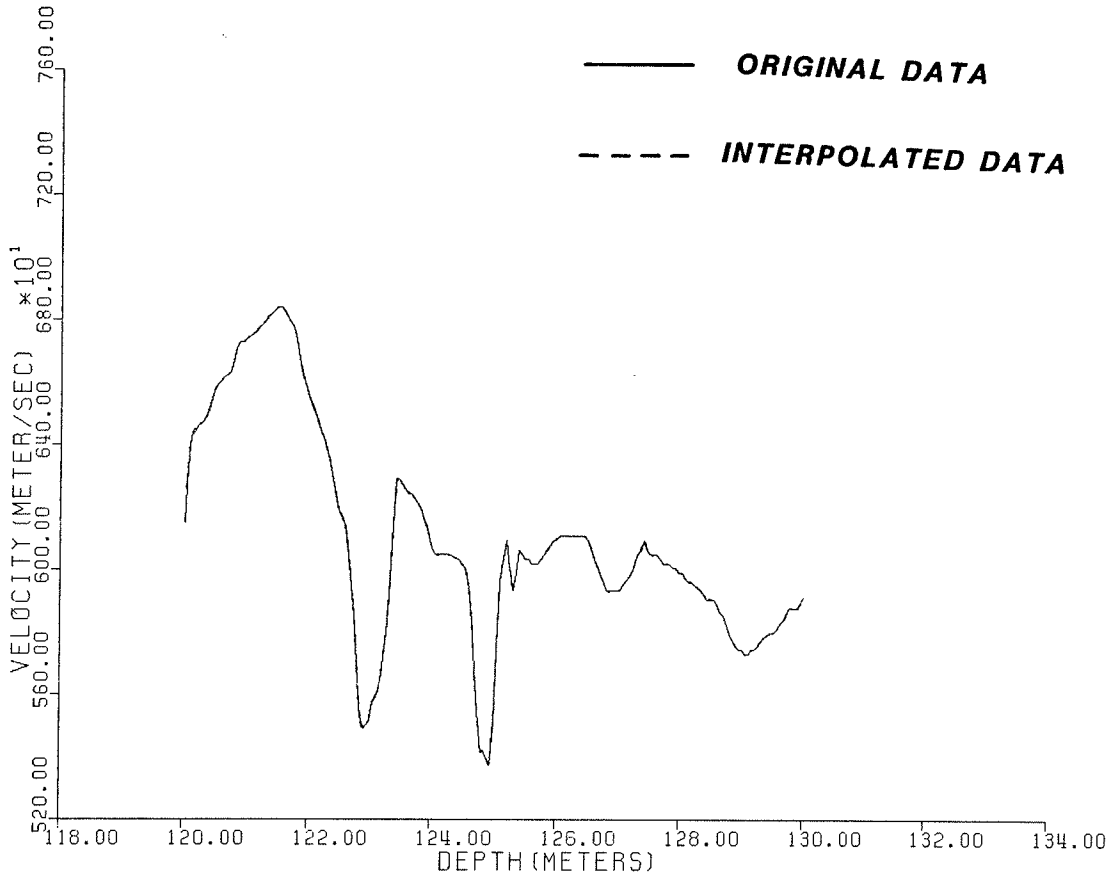

Fig.3.1: Original and interpolated sonic well log data for W=3.

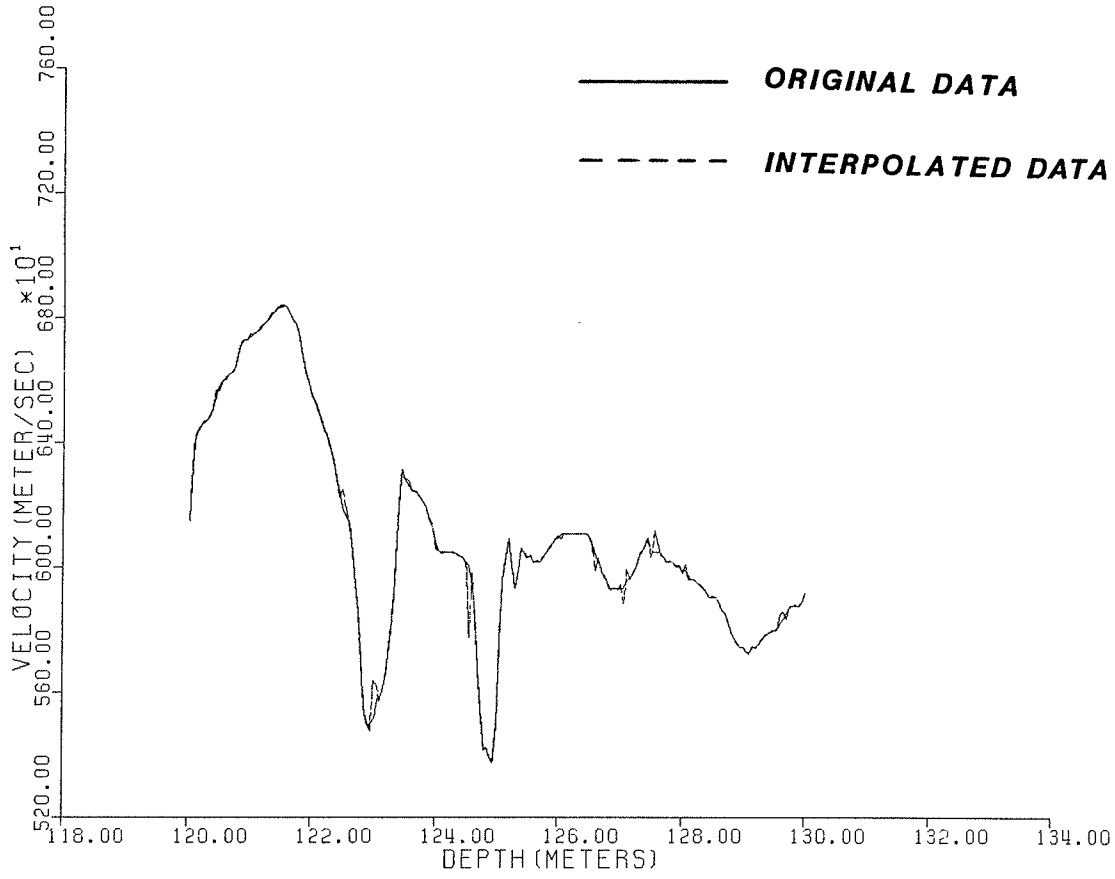

Fig.3.2: Original and interpolated sonic well log data for W=11.

Chapter IV

CORRELATION OF GEOPHYSICAL LOGS IN GRANITE.

In the evaluation of potential sites for the nuclear waste repositories, one of the requirements imposed on geophysical logs is to be able to detect fractures within the granite body. This is very important because fractures are the main conduits along which toxic materials from the disposal vault could be carried to the surrounding environment. Igneous rocks are relatively homogeneous and the ability of geophysical logs to detect such fractures will depend on the petrophysical contrast that exist between the fracture sections and the non-fractured host rock.

One of the major advantages derived from running different types of logs is that these logs can be correlated to provide a much more accurate picture of the subsurface. But in most cases, such correlations are only qualitative and the advantages of a quantitative correlation are overlooked. In this chapter, well log data from the borehole URL6 are presented to illustrate the potential of geophysical logs in detecting fractures within a granite batholith. In order to obtain a quantitative measure of the agreement between the various logs in detecting fractures, cross-correlation will be performed for different pairs of the well log data.

4.1 NATURE AND DISTRIBUTION OF FRACTURE.

The histogram of fracture frequency at depth in the borehole URL6, deduced from the borehole television log(Lau et al. 1983), is shown in figure 4.1. Also shown in figure 4.2 is the same fracture distribution determined from core logging analysis. Even though the number of fractures determined by these two techniques differ, the fracture pattern are very similar. The formation is characterized by well-fractured zones(fracture frequency greater than or equal to 20/5 but less than 50/5) between 97.85-100.08m, 113.19-114.72m and 265.03-272.42; and by six sets of fractures with attitudes of 216° /20° NW, 136° /20° SW, subhorizontal, 38° /21° SE, 348° /24° E and 29° /36° SE. Open fractures are defined as fractures with aperture and filled fractures as fractures with infilling material. Partly open fractures are defined as fractures that are partly filled with infilling materials and have aperture. The common infilling materials are calcite, chlorite, hematite, limonite and sulfides.

4.2 LOG RESPONSE

A suite of geophysical logs recorded in the borehole URL6, is shown in figure 4.3. These logs include the caliper, density, normal resistivity(16'' and 32''), focused-beam, gamma, neutron, single point resistance, sonic, spontaneous potential and temperature logs.

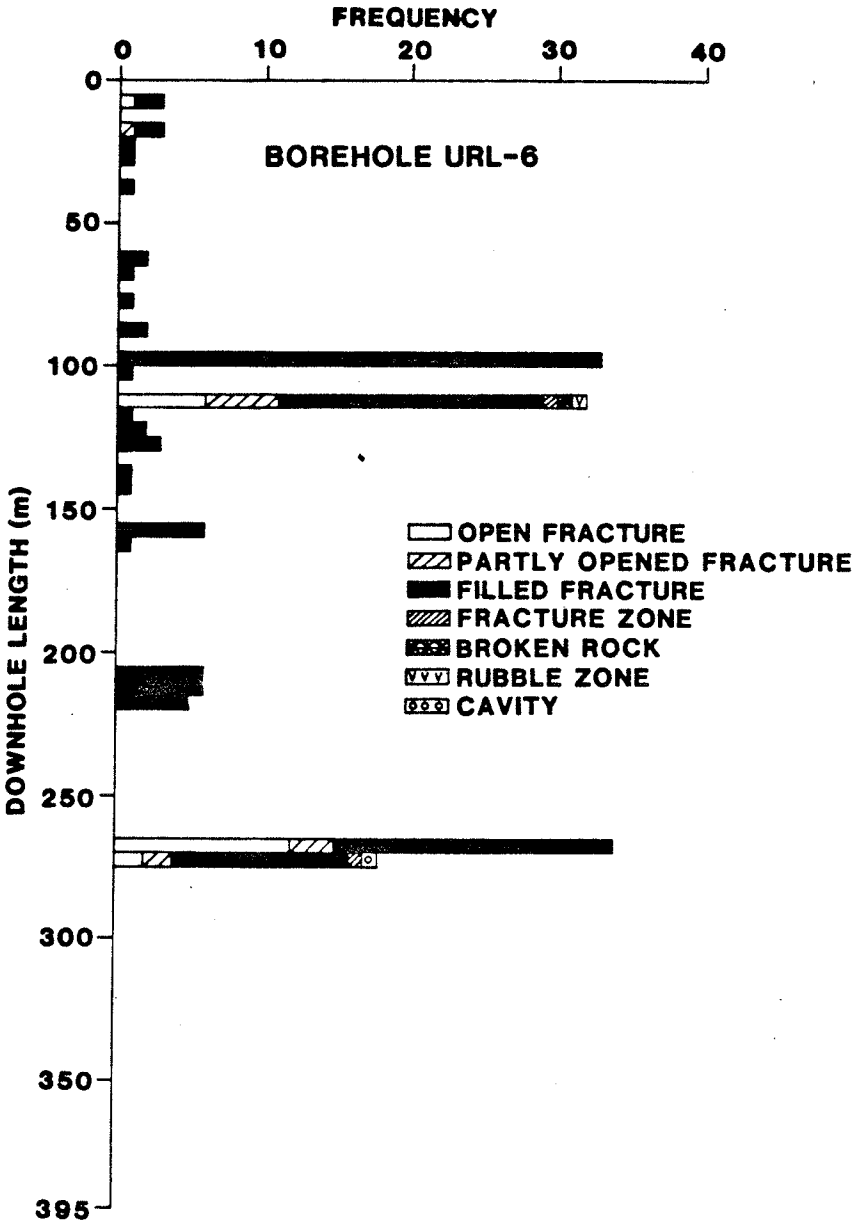

Fig.4.1: Distribution of fractures along the length of borehole URL6 by television survey(Lau et al. 1983).

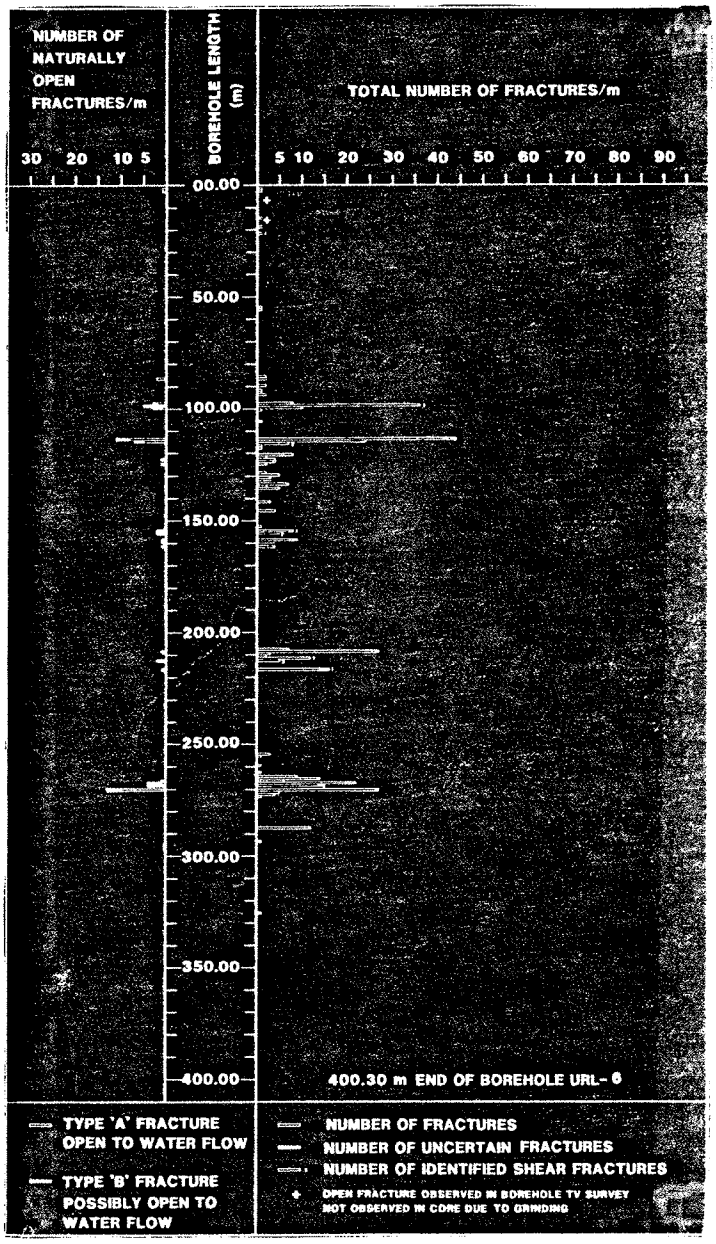

Fig.4.2: Distribution of fractures along the length of borehole URL6 by core analysis.

Fig.4.3: A suite of geophysical logs used to detect fractures.

Caliper Log

The caliper log(fig.4.4) measures fluatuations in the borehole diameter. The spike at 270m coincide with an open fracture. The filled fractures are not adequately resolved. The wall of the borehole is generally rough; this may be attributed to other causes other than fracturing. The step at 271.86m signifies an abrupt termination of the survey when a blockade of the hole was encountered.

Density Log.

The density log(fig.4.5) measures the formation density. It has a background value of 2.7kg/m^3 . Superimposed on this background are two well defined anomalous zones; a positive anomaly at 110-145.4m and a negative anomaly at 267-271m. The positive anomaly indicates the presence of a high density materials; core sample analysis indicate the occurence of hematite and chlorite in this interval. The negative anomaly could be due to either an open fracture or a low density material.

Gamma Log.

The gamma log(fig.4.6) measures the natural radioactivity of the granite. The lack of distinct anomalies can be attributed to the fact that granite has the highest concentration of the three naturally occuring radioelements potassium, uranium and thorium and the total gamma count from these elements may have partially overshadowed the anomalies that might be present. There is also the possibility that the water and other fracture infilling materials may contain

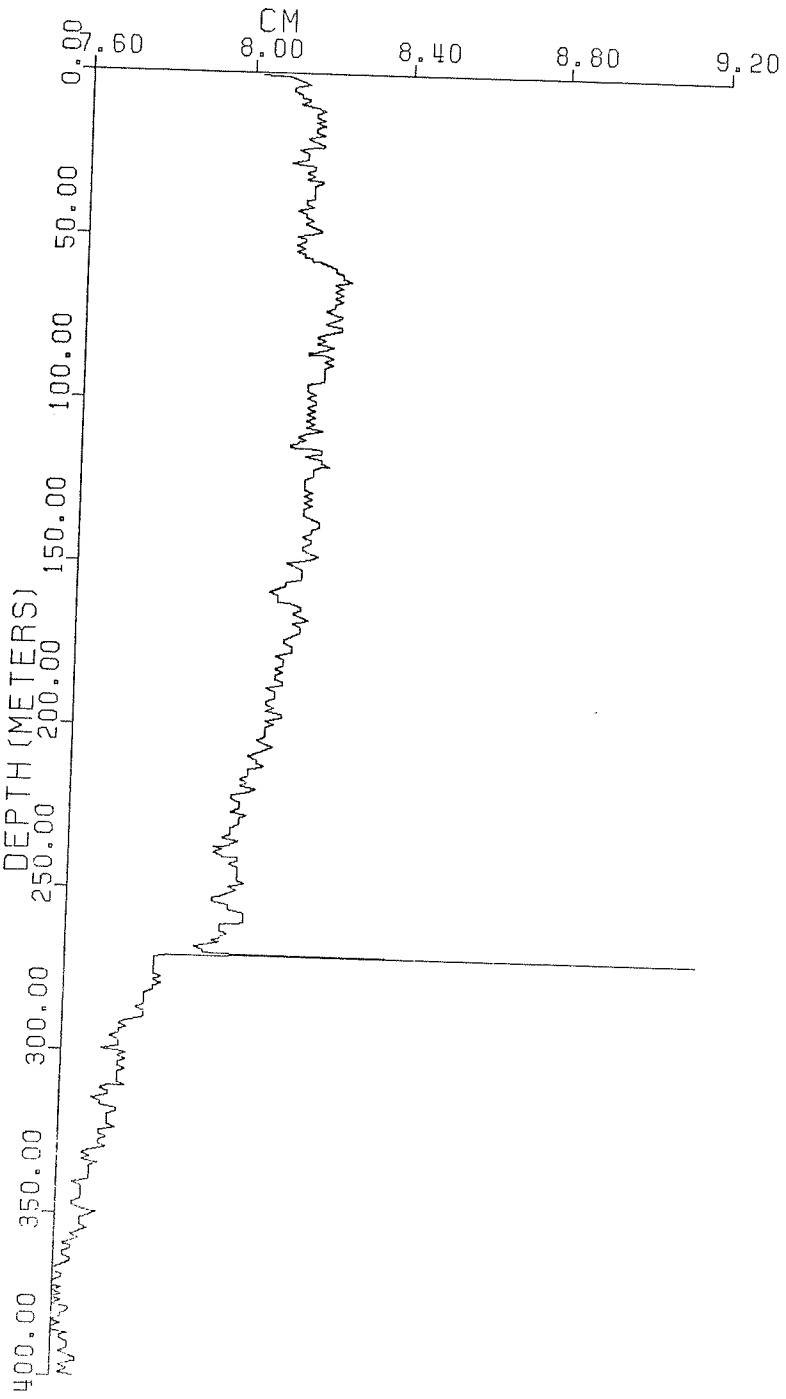

Fig.4.4: Caliper log for borehole URL6.

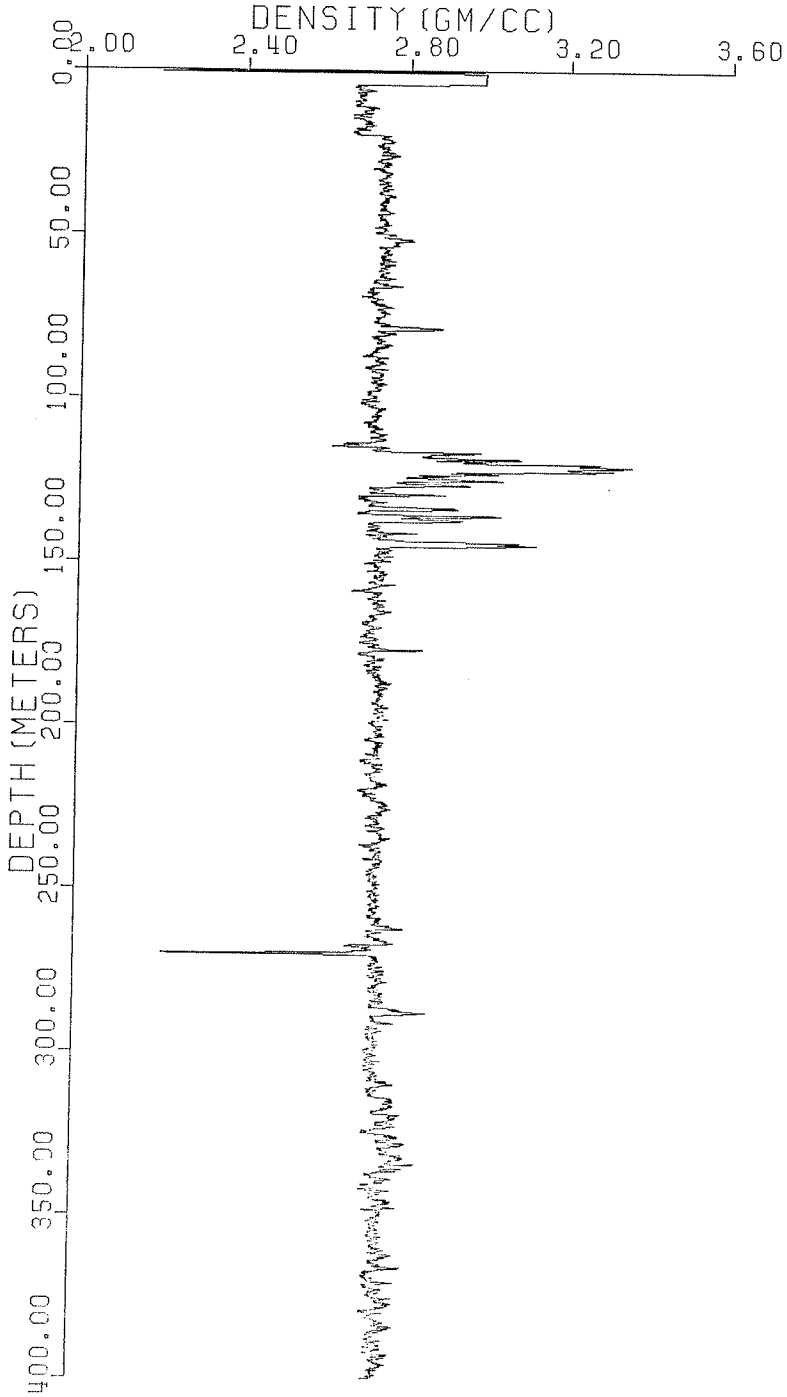

Fig.4.5: Density log for borehole URL6.

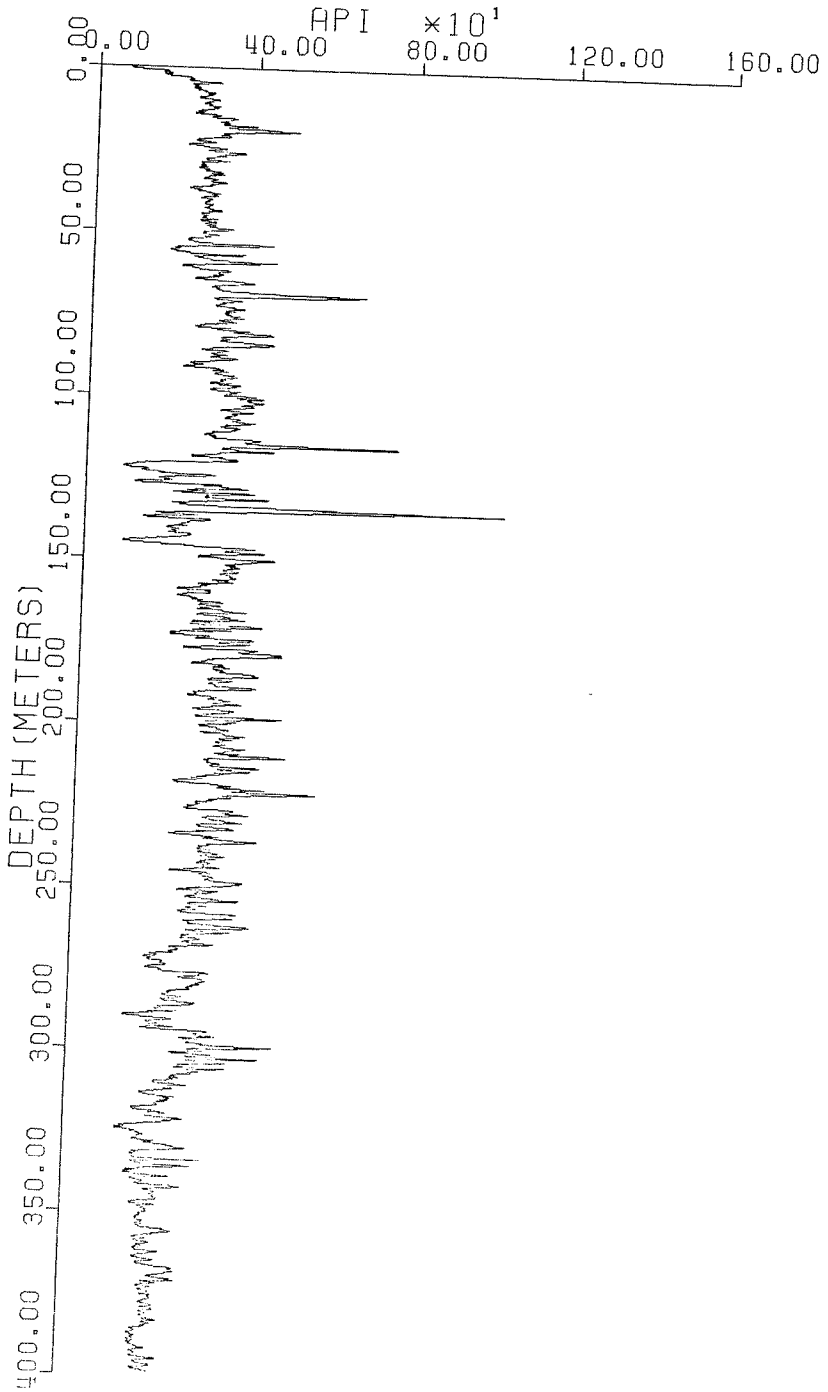

Fig.4.6: Gamma log for borehole URL6.

some traces of radioactivity as a result of various hydrothermal reactions. However, there is a remarkable variation in the count rate between 110-140m which is in coincidence with the density log.

Neutron Log.

The neutron log(fig.4.7) is used principally for delineation of porous formation. Lower count rate are usually attributed to porous zones or increasing water content. It can also be attributed to other minerals which are good absorbers of thermal neutrons. Major zones with lower count rates occur at 110-150m, 264-271m and 287.9-288.4m. There is a good agreement between the neutron and the density log.

Sonic Log.

The sonic log(fig.4.8) measures the interval transit time which is the reciprocal of the compressional wave velocity. The oustanding features occur at 110-140m, 202.5-203m, 267-271m, 287.9-288.4m and 383.5-384.8m. These indicate fracture zones. The anomaly at 110-140m is caused by the high density materials.

Spontaneous-Potential log.

The spontaneous log(fig.4.9) measures the potential generated within the granite. It is rather featureless except for some minor variations at 24.4m, 113.7m, 124.4m, 144.7m and 267-271m. These indicate permeable or mineralized zones. The last anomaly in particular coincide with the sonic, neutron and density logs.

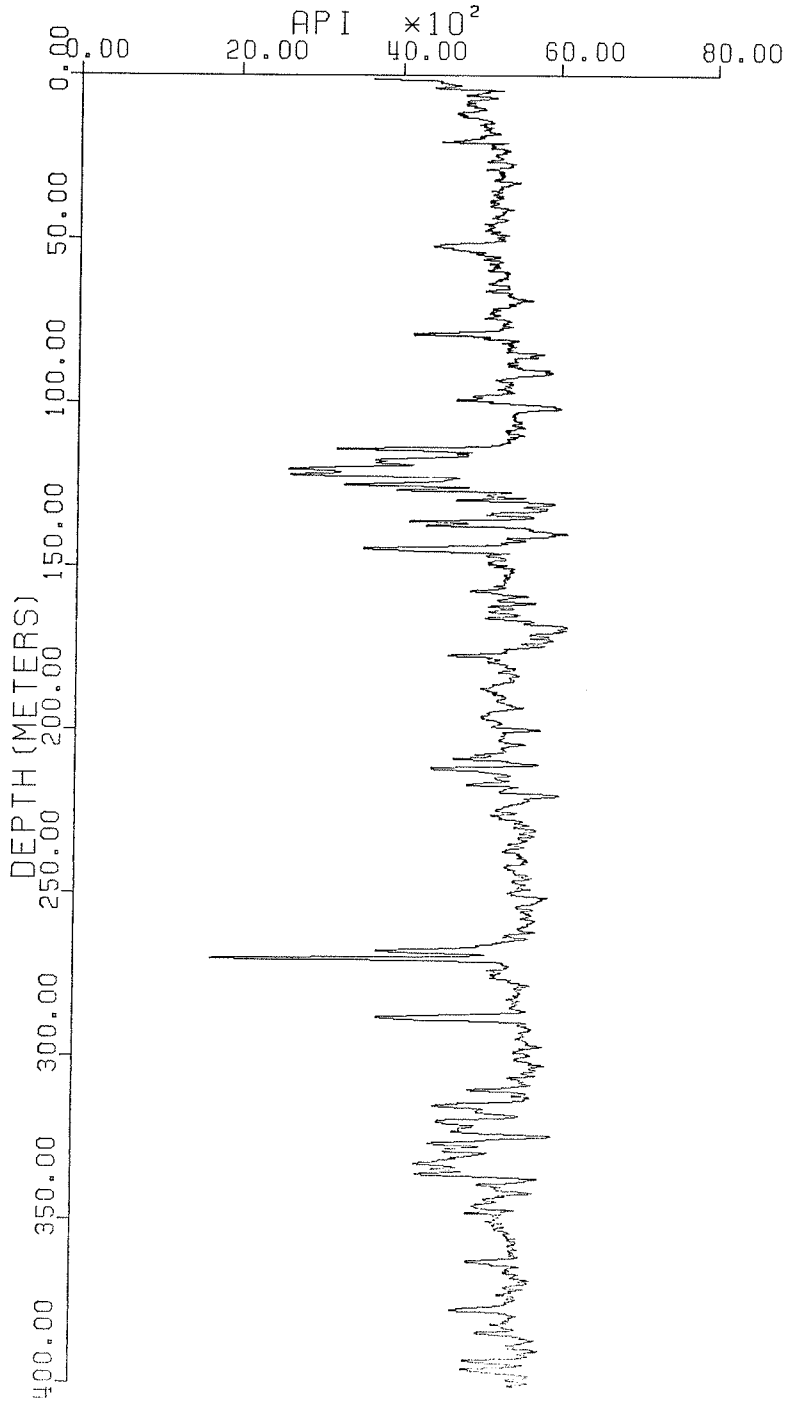

Fig.4.7: Neutron log for borehole URL6.

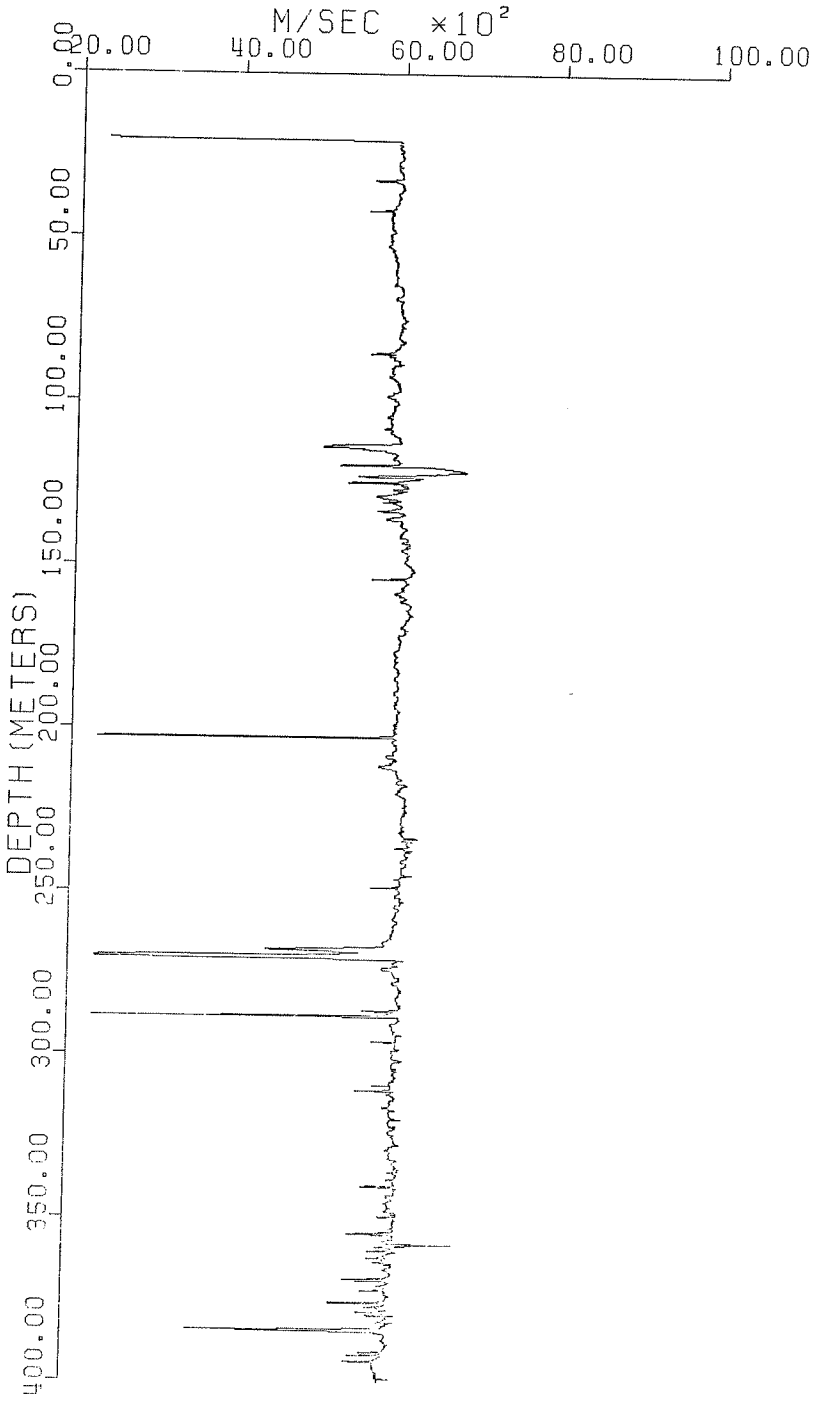

Fig.4.8: Sonic log for borehole URL6.

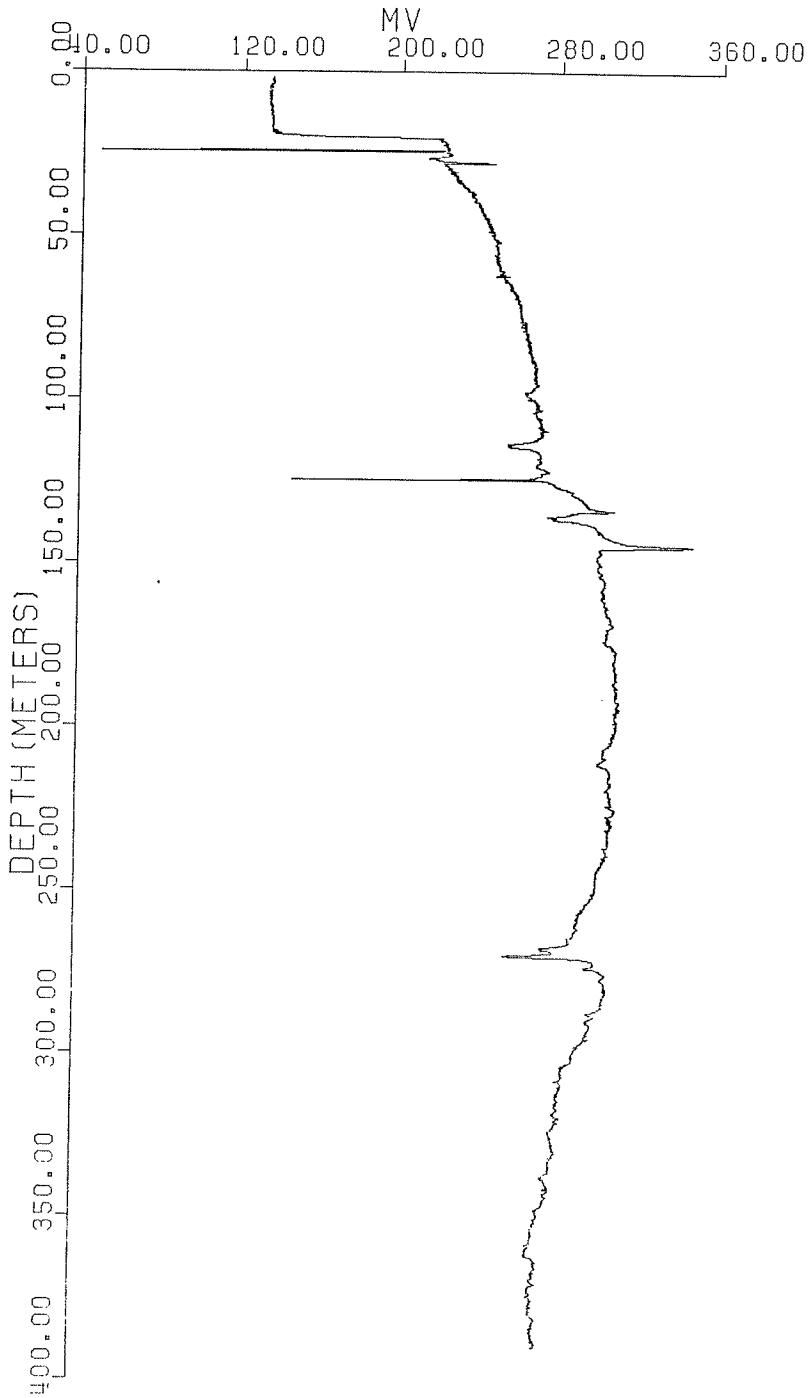

Fig.4.9: Spontaneous potential log for borehole URL6.

Temperature Log.

The temperature log(fig.4.10) measures the temperature within the borehole. There is a general increase with depth. The anomaly at 257.5-285m signifies an inflow of warm water.

Resistivity Logs.

The normal(16'' and 32''), focused-beam and the single-point logs(fig.4.11-4.14) all measure the electrical resistance of the formation. Granite has a very high resistivity due to its low porosity. Anomalous deflections associated with fracturing occur at 98-145m and 265-272m with the single-point and the focused-beam logs showing the least and most intense variations respectively. Petrologically, the granite penetrated by the by the borehole is predominantly composed of a pink and grey granite which have characteristic resistivity values. Core sample analysis has revealed that except for the interval 118-120m and 225-245m, the transition between these two units occur at 280m. This can be detected on the focused-beam log. The log has a background value of about 70000 Ω-m down to 240m; characteristic variations associated with fracture zones occur within 110-150m and 208-220m. Below 240m, the resistivity begins a steep decrease until another fracture zone is encountered at 265-272m after which the background drops to about 120 Ω-m.

Fig.4.10: Temperature log for borehole URL6.

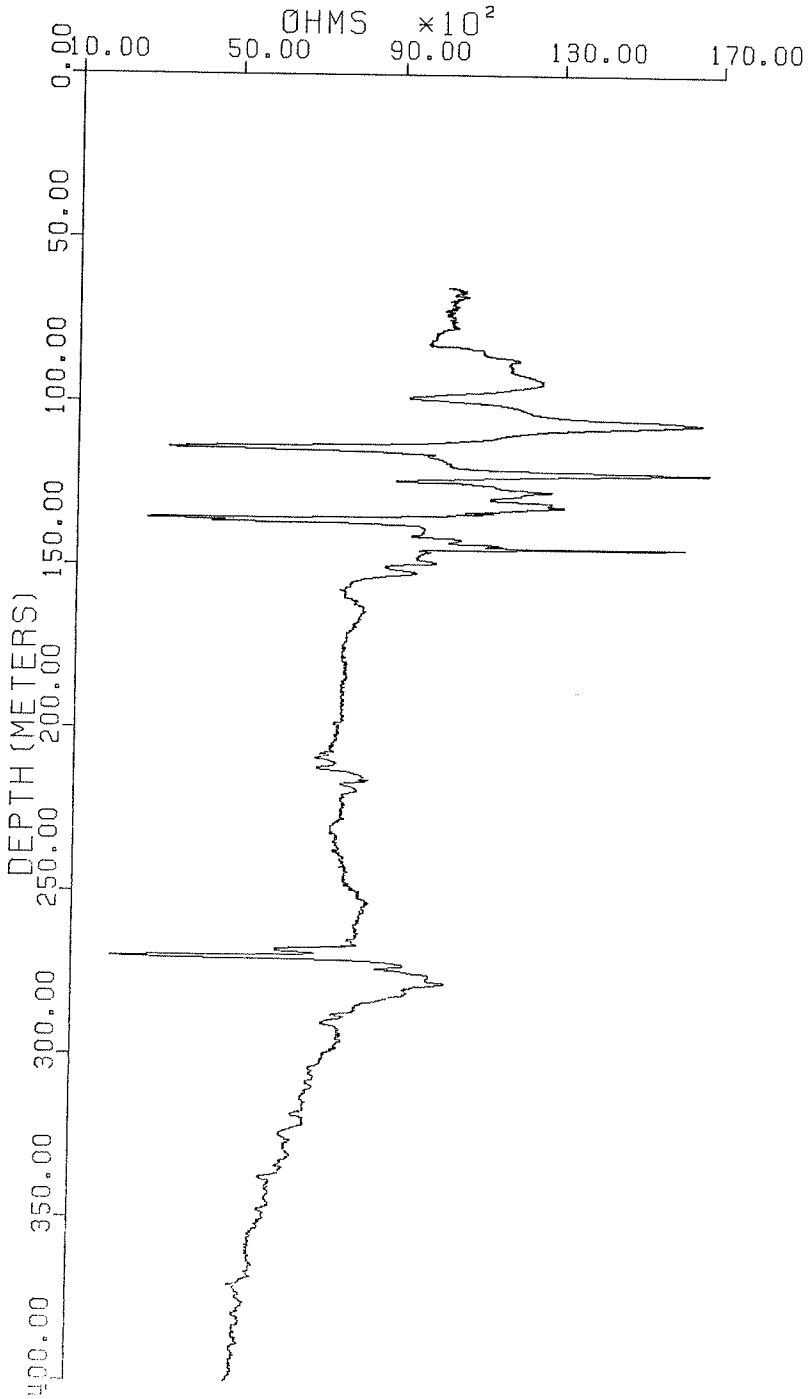

Fig.4.11: Normal resistivity(16'') log for borehole URL6.

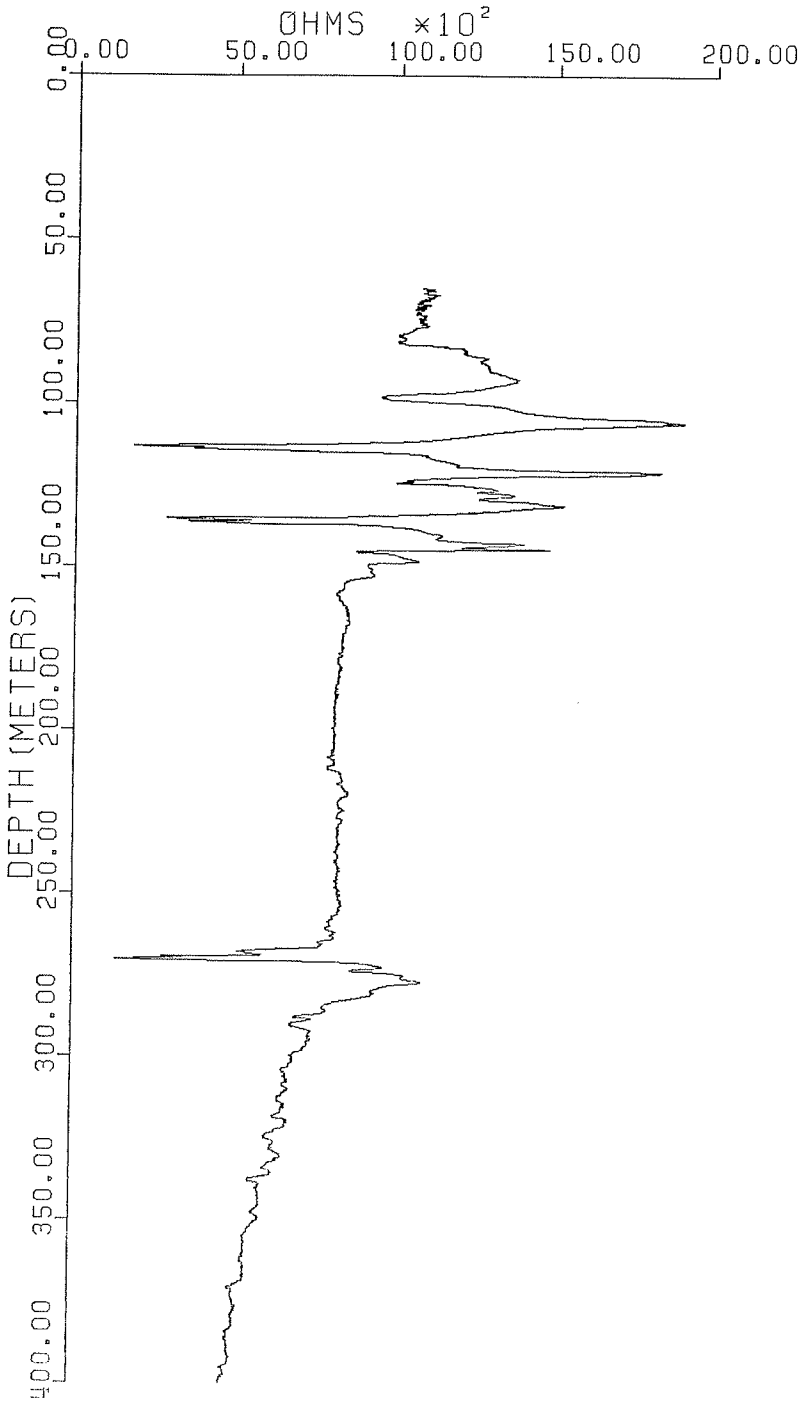

Fig.4.12: Normal resistivity(32'') log for borehole URL6.

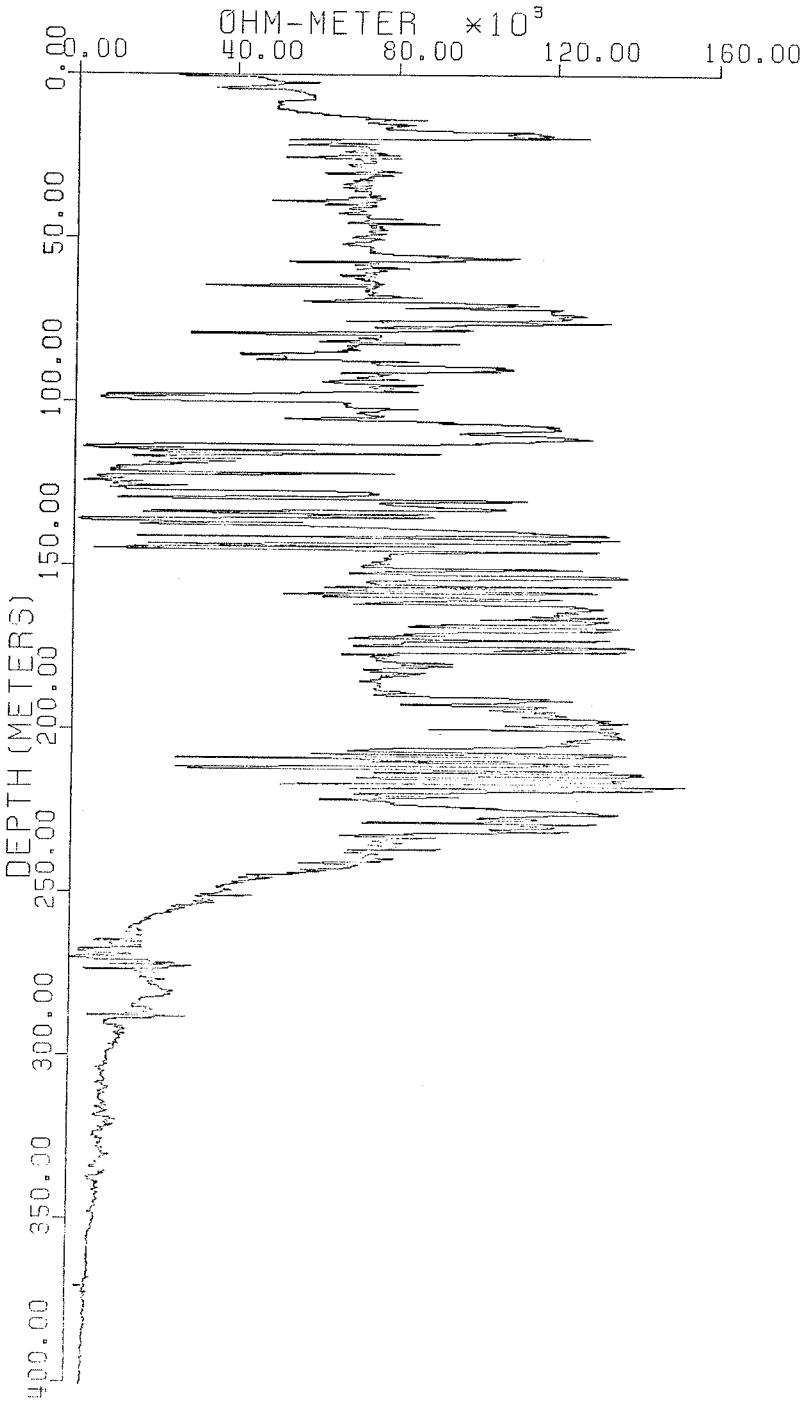

Fig.4.13: Focused-beam log for borehole URL6.

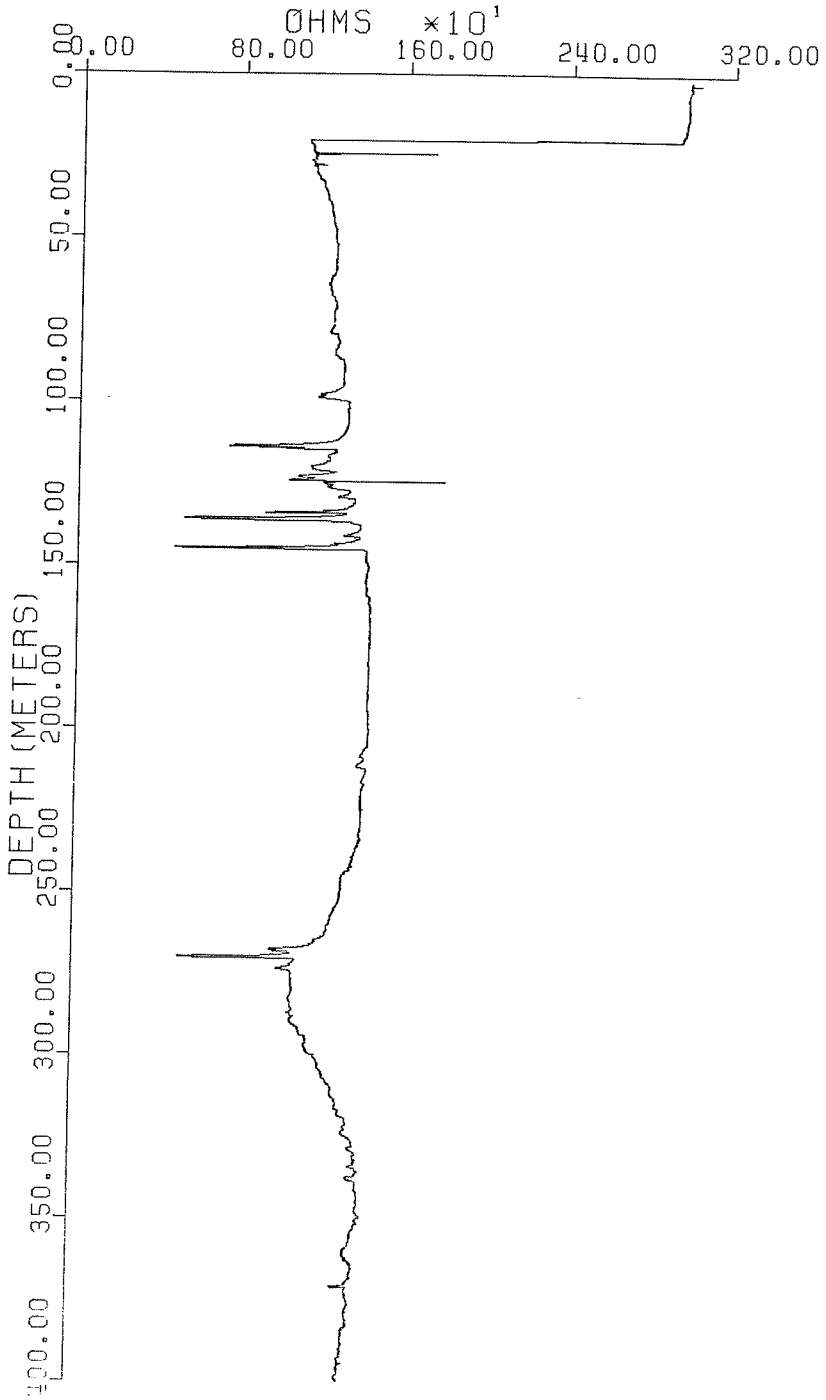

Fig.4.14: Single point resistance log for borehole URL6.

4.2.0.1 Remarks on Geophysical Log Data.

The general correlation amongst the various geophysical logs is quite impressive. Two distinct fracture zones can be deduced. These are located at 98-150m and 267-272m. The latter is characterized by a low electrical resistivity, low density, low compressional wave velocity, low neutron count rate, anomalous borehole diameter and temperature increase. These observations suggest a permeable zone. The fracture zone which occur at 98-150m is charaterized by variations of the neutron, density, sonic and the resistivity logs which suggest the occurrence of different minerals. It also appears to be a predominantly filled fracture zone with no indication of fluid flow from either the temperature or the caliper log. The spontaneous log however suggest that a limited permeability may exist in this zone.

Apart from these two major fracture zones, there are other intervals where fracturing is apparent and can be traced on only a few of the logs.

A fracture zone which appears to be located at 202.5-215m can be traced on the sonic and the resistivity logs. The faint intensity of this anomaly on the normal log resistivity logs may be due to the large resistivity contrast that exist between this interval and the water in the borehole. The penetration of the measured current of the normal log is severely affected by large resistivity contrasts. Another fracture appears to be located at 286.5-289.4m. This is

characterized by a low compressional wave velocity, a low neutron count rate and a slightly high density anomaly.

4.3 CROSS-CORRELATION.

The basis of the correlation method employed is the assumption that well-log recorded is a geologic time(space) series with defined trends; and that the associated maximum errors occur at the fracture zones. Hence, if the trends are removed what remains is a time series describing the distribution of the fractures.

Review of Cross-Correlation Theory.

Let us assume that we have made measurements of two quantitative variables, X and Y, which have been measured at n specified depths down a single well: thus the data are of the form $\{x_i\, y_i\, d_i,\ (i=1, 2, \ldots\ldots\ldots n)\}$ where $(x_i\, y_i)$ denotes a pair of reading recorded at the ith position (depth di in the well; the data have been ordered by depth, that is d_1, d_2 ,....,dn The cross-correlation C_{xy} between X and Y is given by

$$C_{xy} = \frac{\sum^{n} (x_i - \bar{x})(y_i - \bar{y})}{\left[\sum^{n}(x_i-\bar{x})^2 \sum^{n}(y_i-\bar{y})^2\right]} \qquad 4\cdot3-1$$

where

$$\bar{x} = \frac{\sum^{n} x_i}{n} \quad , \quad \bar{y} = \frac{\sum^{n} y_i}{n}$$

The value of C_{XY} ranges from 0, when there is no correlation to ±1 when there is complete correlation. The expression in equation 4.3-1 can be rewritten as

$$C_{XY} = \sum^{n} \frac{(x_i - \bar{x})(y_i - \bar{y})}{\left[\sum^{n}(x_i-\bar{x})^2 \sum^{n}(y_i-\bar{y})^2\right]} = \sum^{n} D_{XY} \qquad 4.3-2$$

where

$$D_{XY} = \frac{(x_i - \bar{x})(y_i - \bar{y})}{\left[\sum^{n}(x_i-\bar{x})^2 \sum^{n}(y_i-\bar{y})^2\right]}$$

ΣD_{XY} represents the correlation between X and Y as a function of depth.

If the two variables have different lengths, equations 4.3-1 and 4.3-2 are modified to accomodate only a fixed window size of data common to both logs.

4.3.1 Data.

Before the analysis is started, the following assumptions were made:

(1) Removal of trends from the data does not degrade the results of the mathematical analysis,

(2) The effect of the overburden layer is excluded from analysis by chosing a starting depth of 20.5m.

The first assumption was necessary because interuption of field procedures and water salinity can result in artificial waveform trends that are not related to the occurence of fractures. The second assumption was to ensure that the analysis is confined only to granite.

Because the correlation algorithm requires that the data values occur at equal intervals, Lagrange's interpolation method was used to obtain an evenly spaced data points at intervals of 0.05m. To minimize the interpolation error, three data points were used for the interpolation.

4.3.2 Trend Analysis.

The interpolated data were considered as consisted of the following components:

(1) Background and Trend Y(x).

(2) Occassional fluctuation F(x) due to the fractures.

(3) Irregular fluctuation or noise E(x).

And the assumed additive model has the form

$$y(x) = Y(x) + F(x) + E(x) \qquad 4.3.2\text{-}1$$

A preliminary analysis of the data indicats that the trends may be represented by polynomials of degrees not greater than three. Hence if the occassional fluctuations F(x) are ignored, then under the additive model we have

$$y(x) = \beta_0 + \beta_1 x + \cdots\cdots \beta_n x^n + E(x) \qquad 4.3.2\text{-}2$$

where β_n's are coefficients to be determined from the data.

4.3.3 Analytical Procedure.

Different polynomials were fitted to each well log data, and the coefficients of the polynomial which best represents the trend was determined by the method of least squares. The trend was removed from the data by subtracting the best fit polynomial. Different pairs of the processed logs were cross-correlated using equations 4.3-1 and 4.3-2 for the following intervals;

(1) 90 - 150m

(2) 267 -272m

(3) Total length.

The first and second intervals contain the two major fracture zones.

4.4 RESULTS AND DISCUSSION.

The correlation results are shown in figure 4.15 through 4.25. Even though the correlation values can either be positive or negative, only the absolute values are plotted. The correlation coefficients values for the total lenght are generally low and except for the correlation of resistivity(16'')-resistivity(32'') and neutron-density, the values are all less than 0.5. The caliper log correlates the least with the other geophysical logs. It must be emphasized that these values represent the global or total correlation amongst the various logs. The correlation ΣD_{XY} as a function of depth, are shown in figures 4.26 through 4.77.

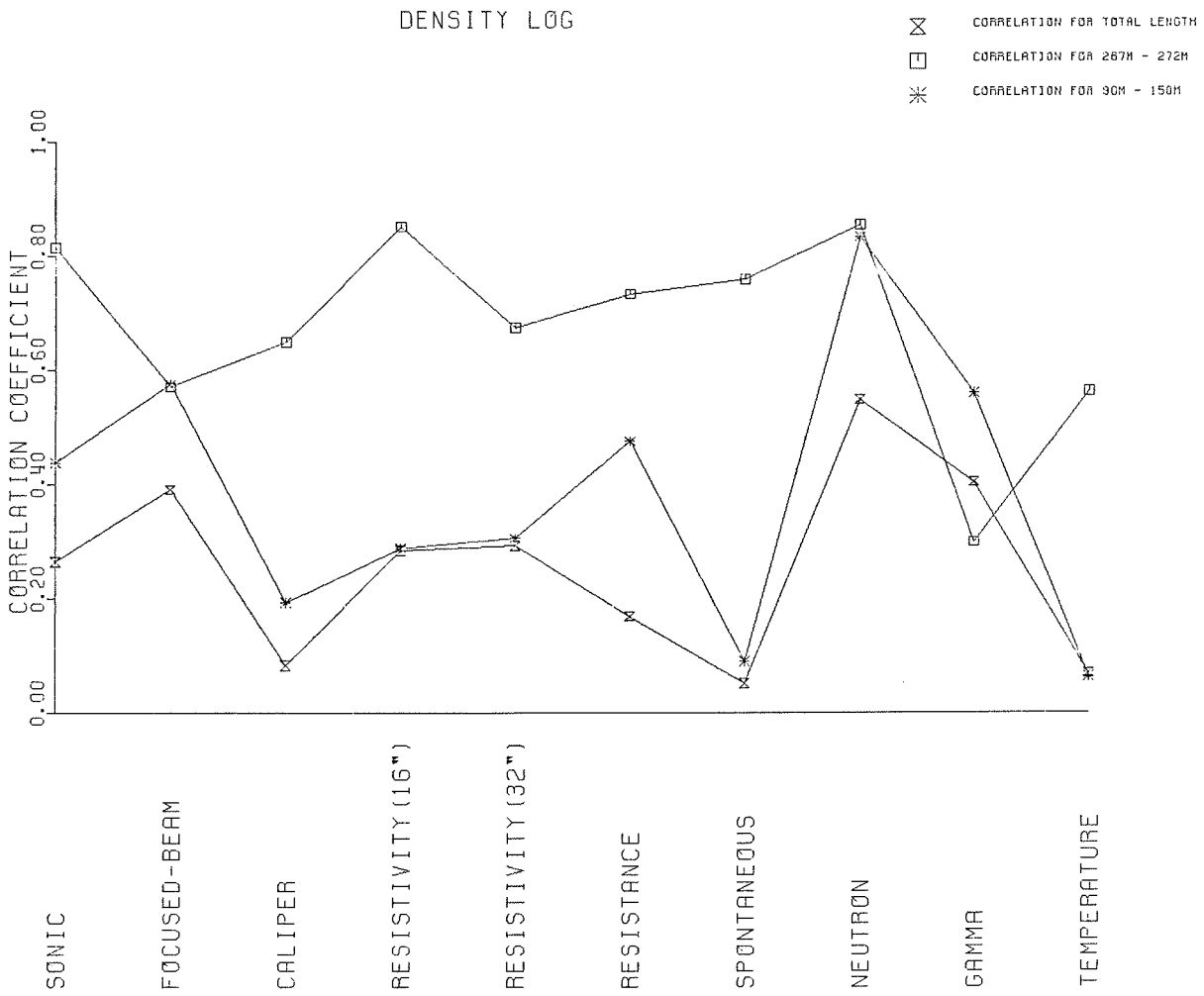

Fig.4.15: Correlation of density and other geophysical logs.

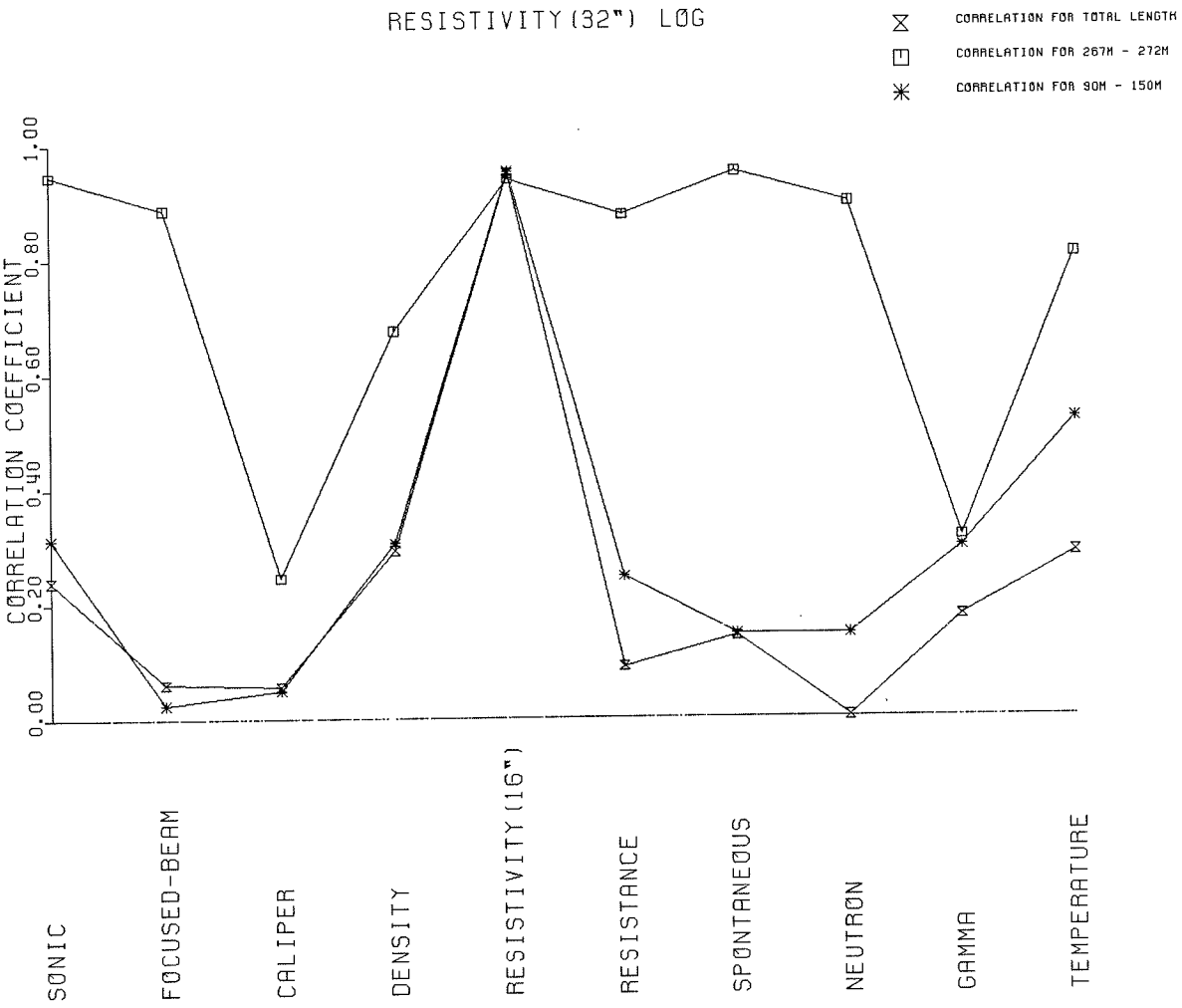

Fig.4.16: Correlation of resistivity(32'') and other geophysical logs.

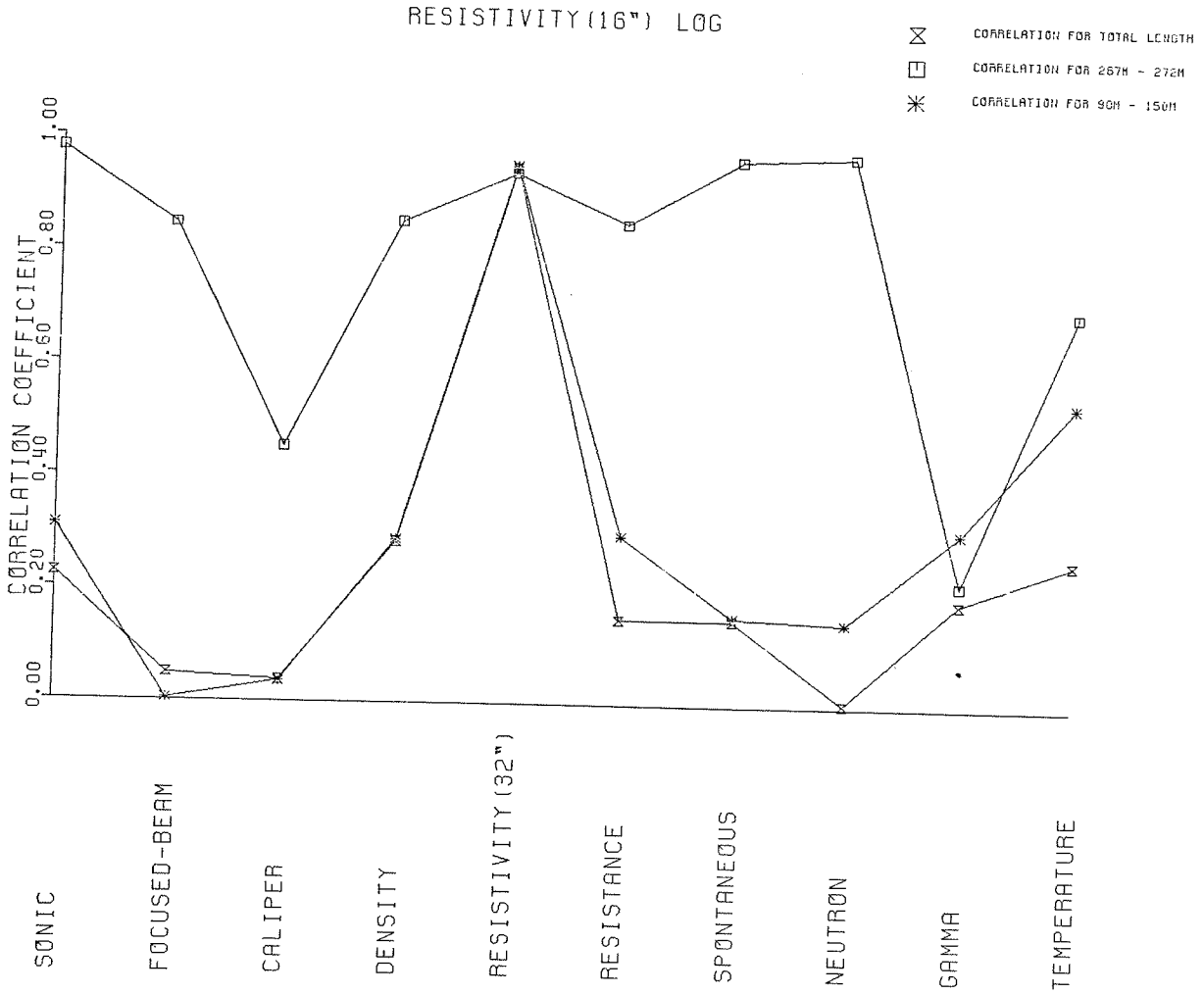

Fig.4.17: Correlation of resistivity(16'') and other geophysical logs.

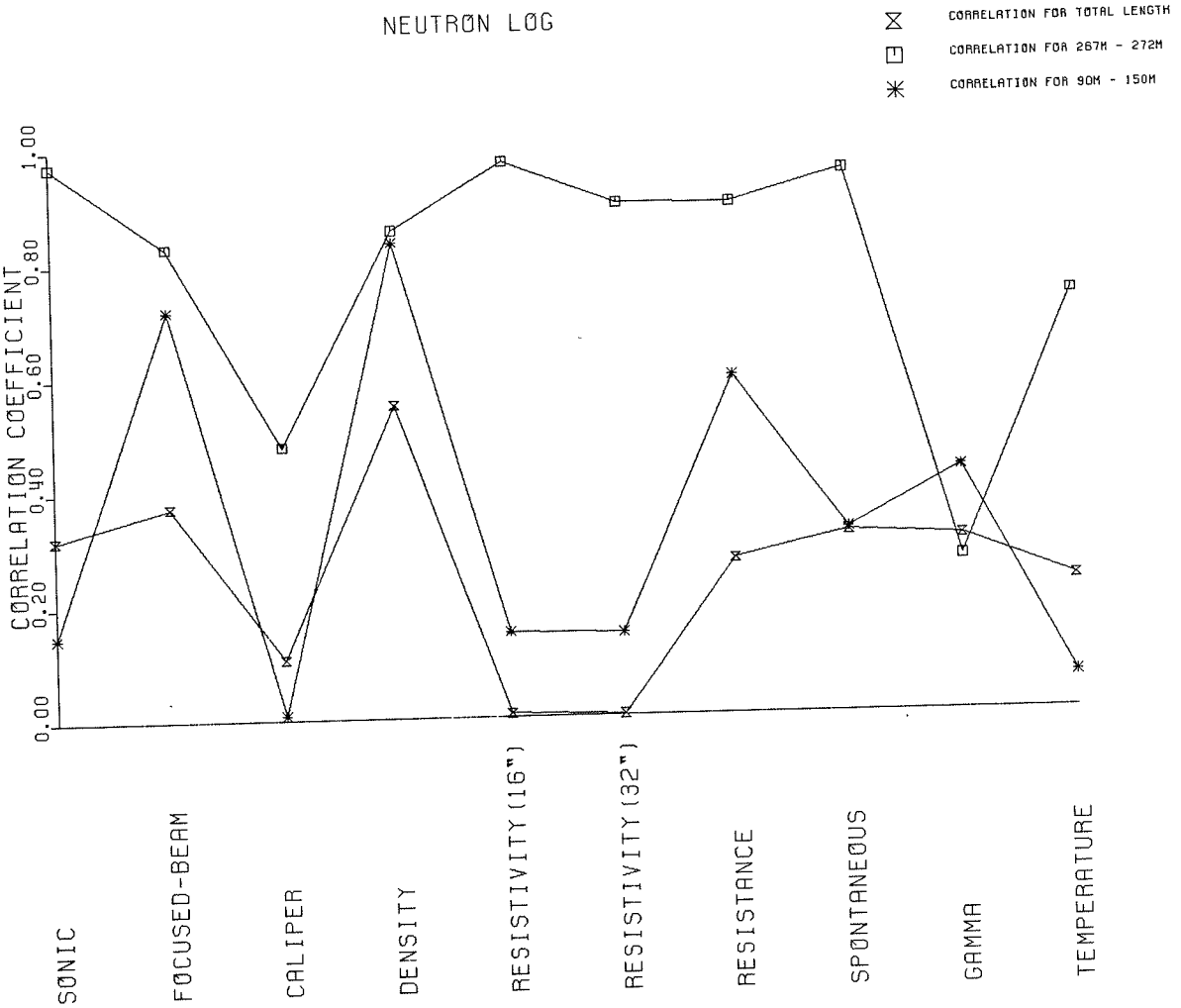

Fig.4.18: Correlation of neutron and other geophysical logs.

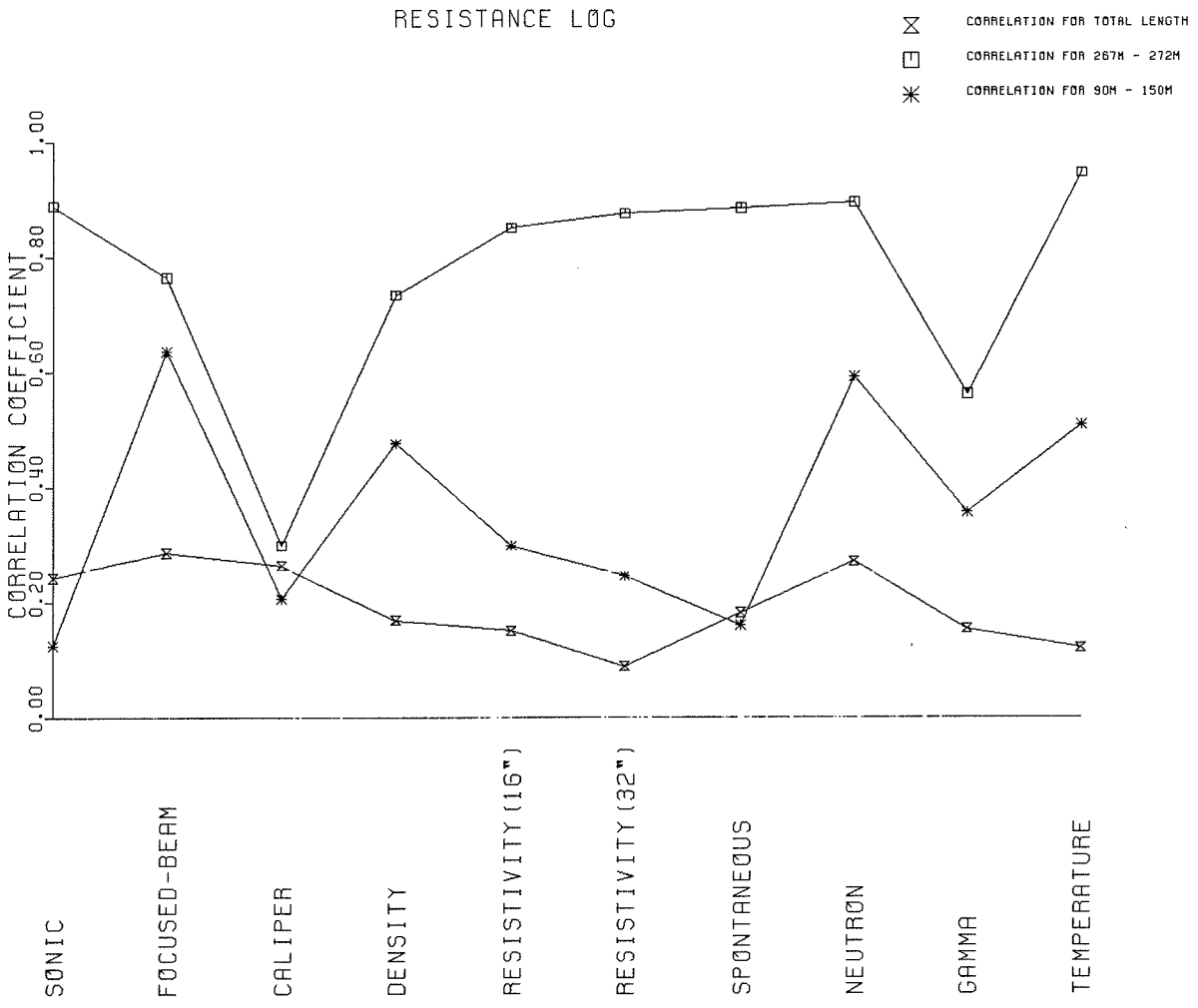

Fig.4.19: Correlation of resistance and other geophysical logs.

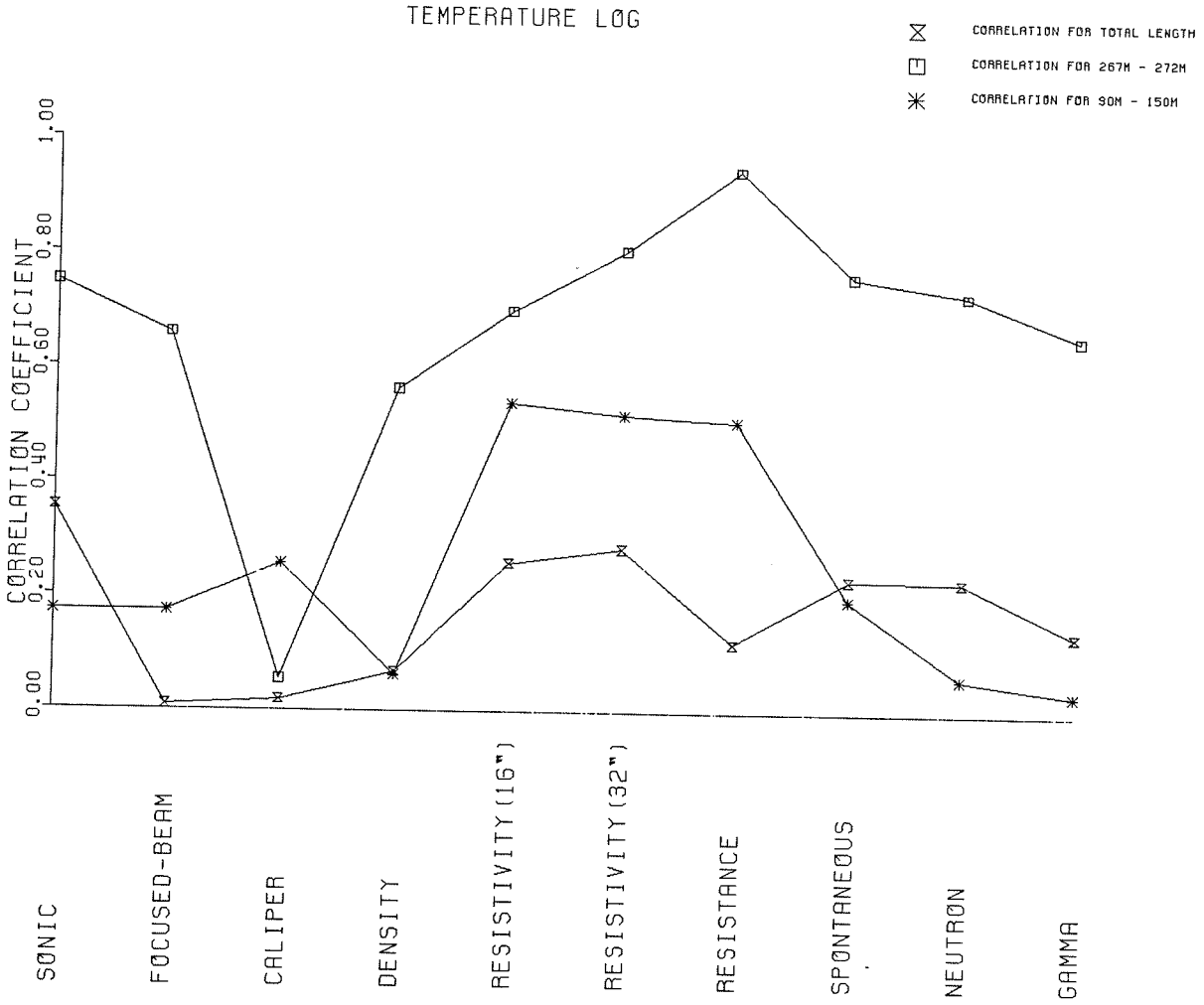

Fig.4.20: Correlation of temperature and other geophysical logs.

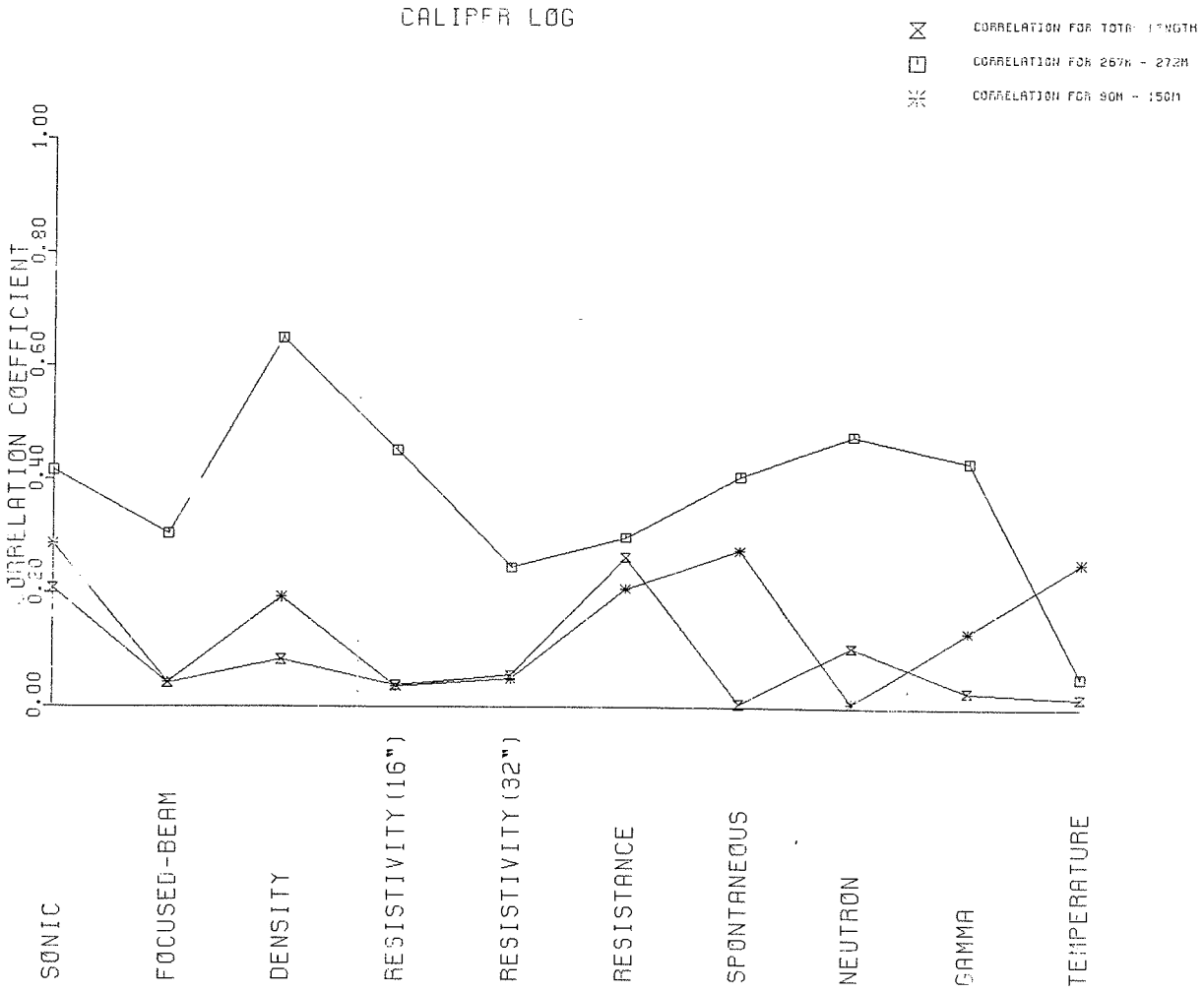

Fig.4.21: Correlation of caliper and other geophysical logs.

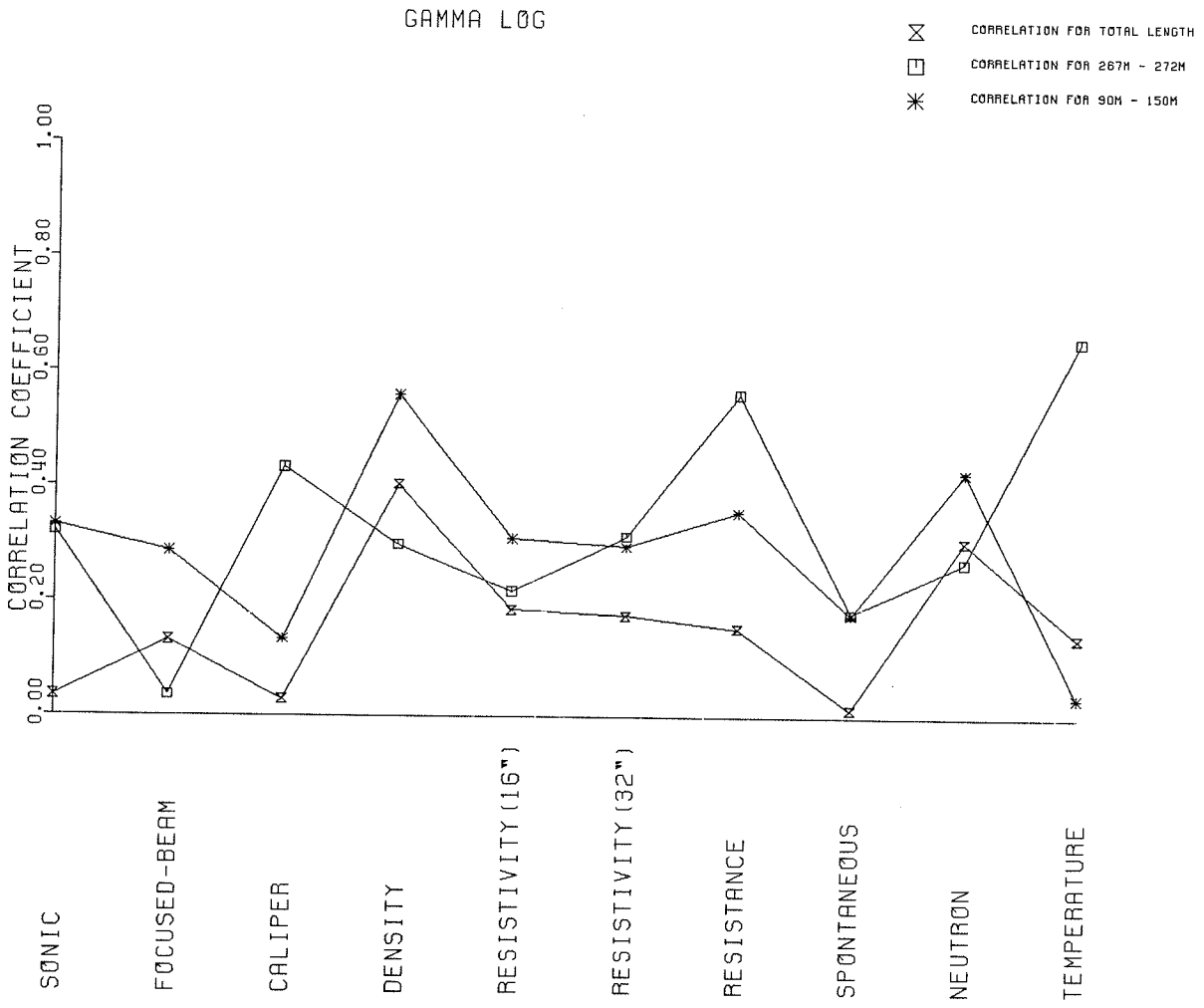

Fig.4.22: Correlation of gamma and other geophysical logs.

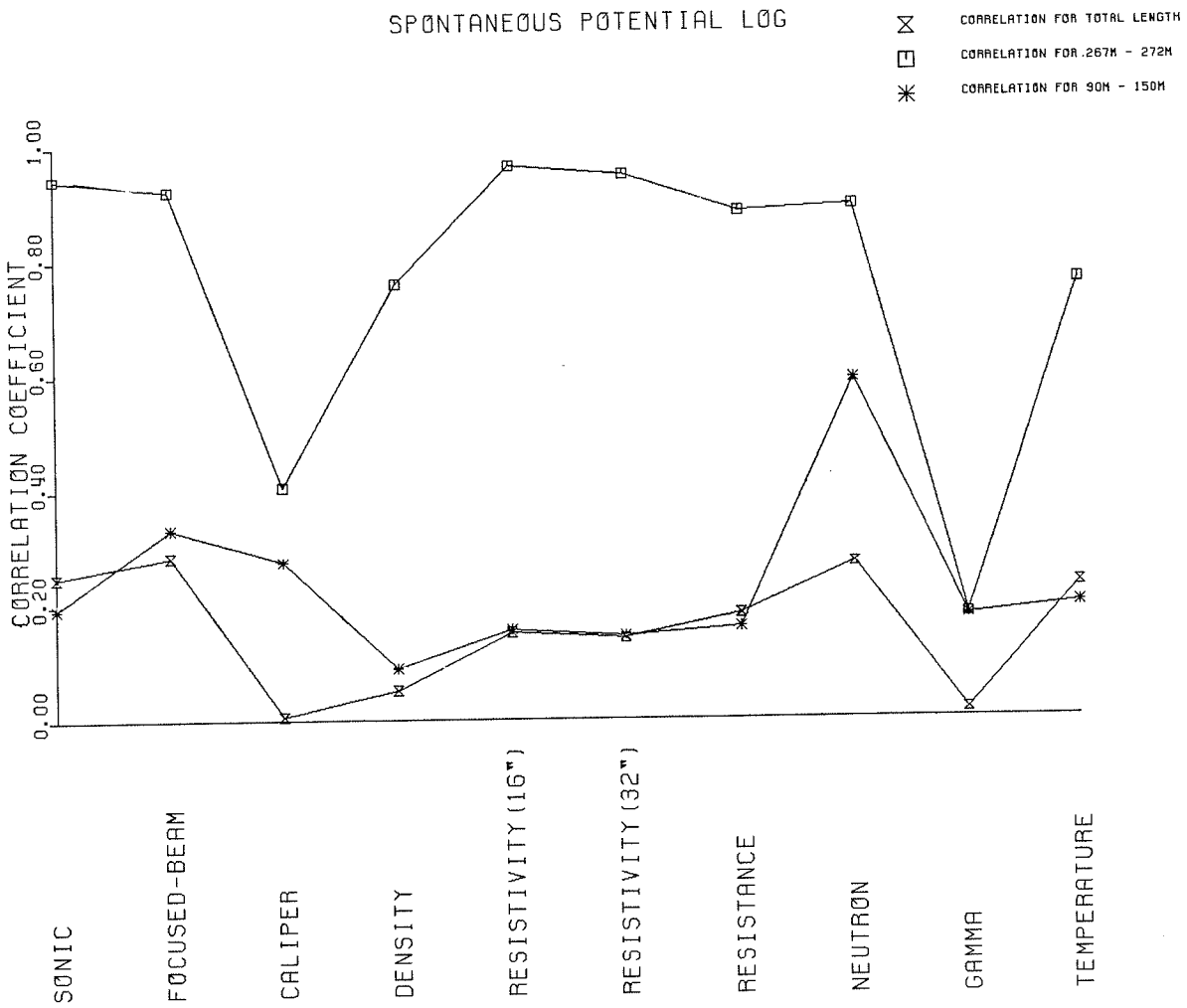

Fig.4.23: Correlation of spontaneous potential and other geophysical logs.

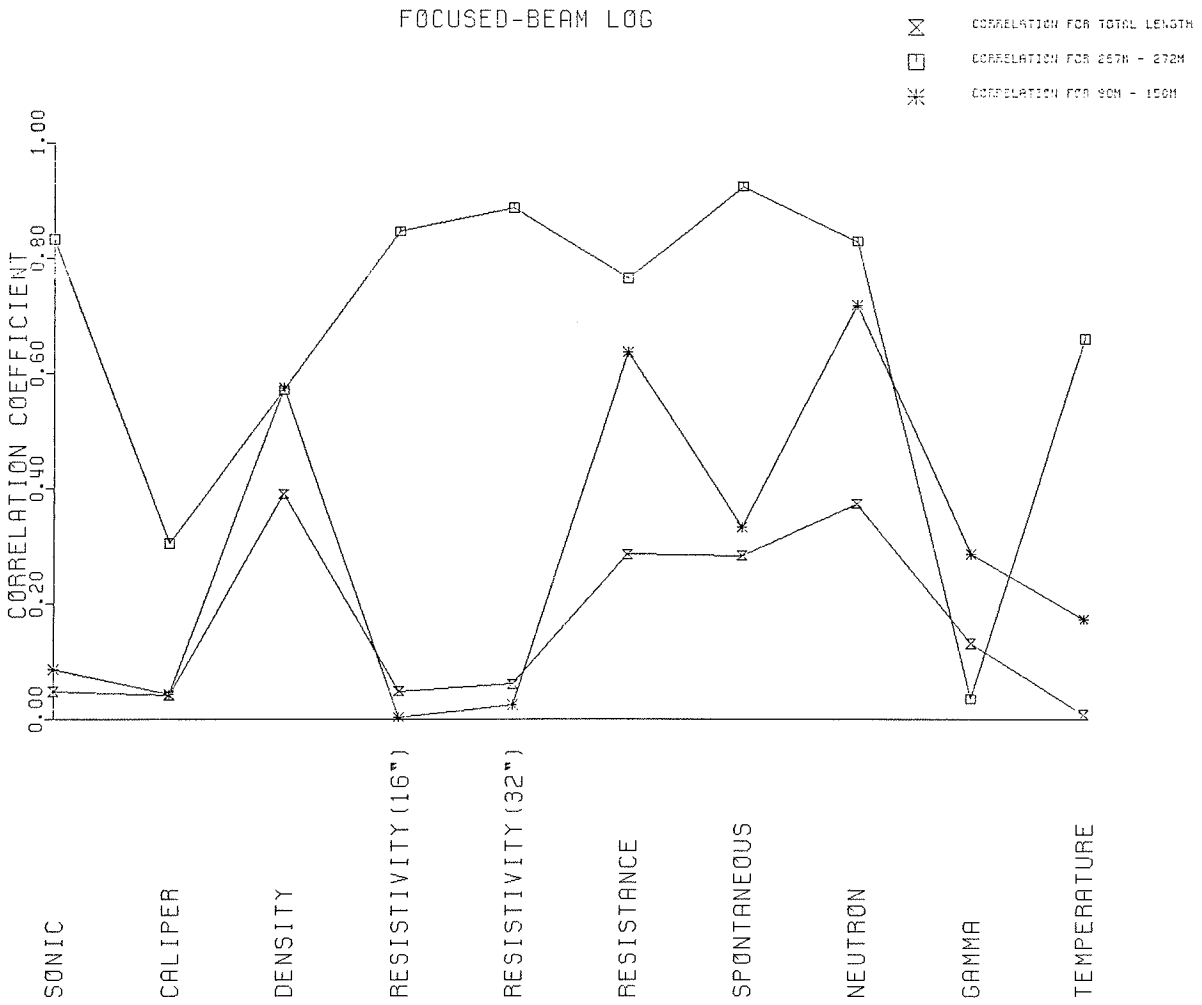

Fig.4.24: Correlation of focused-beam and other geophysical logs.

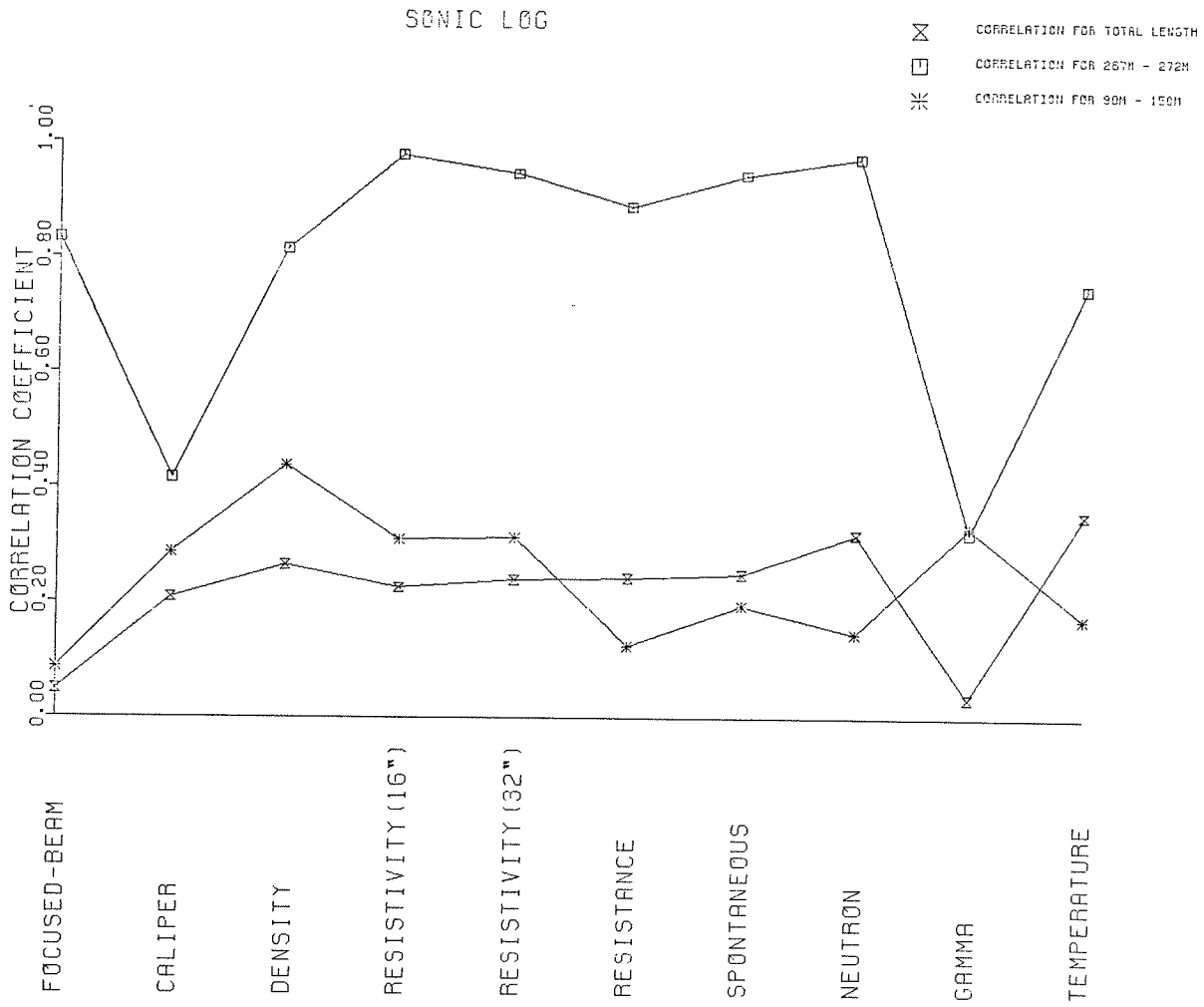

Fig.4.25: Correlation of sonic and other geophysical logs.

These figures indicate how the logs correlate at various depths and in particular within the fracture zones. For example, within the two major fracture zones, there is an almost one to one correlation between the density and resistance log(fig.4.26), neutron and resistance log(fig.4.27) and density and neutron log(fig.4.28). Notice also the improvement in the correlation of the resistivity(16'') and gamma(fig.4.29), focused-beam and gamma(fig.34.30) and resistance and spontaneous potential log(fig.4.31).

It is realized that the global correlation coefficient values do not always agree with the correlation with depth ΣD_{xy}. For example the global correlation coefficient value for the density and resistance log(fig.4.26) is 0.17 and that for neutron and resistivity(16'') log(fig.4.32) is only 0.006, even though in both cases there is an almost one to one correlation within the major fracture zones. The reason for such descrepancy is that cross-correlation measures the similarity between waveforms rather than the similarity in detecting lithologic boundaries. As an illustration consider two different logs Log1 and Log2 (fig.4.78) with different response within the same stratigraphic section. The value of the correlation coefficient is zero, yet so far as the detection of fractures are concerned, there is a perfect agreement. This observation suggests that the global cross-correlation value might not always be a good measure of the agreement between various

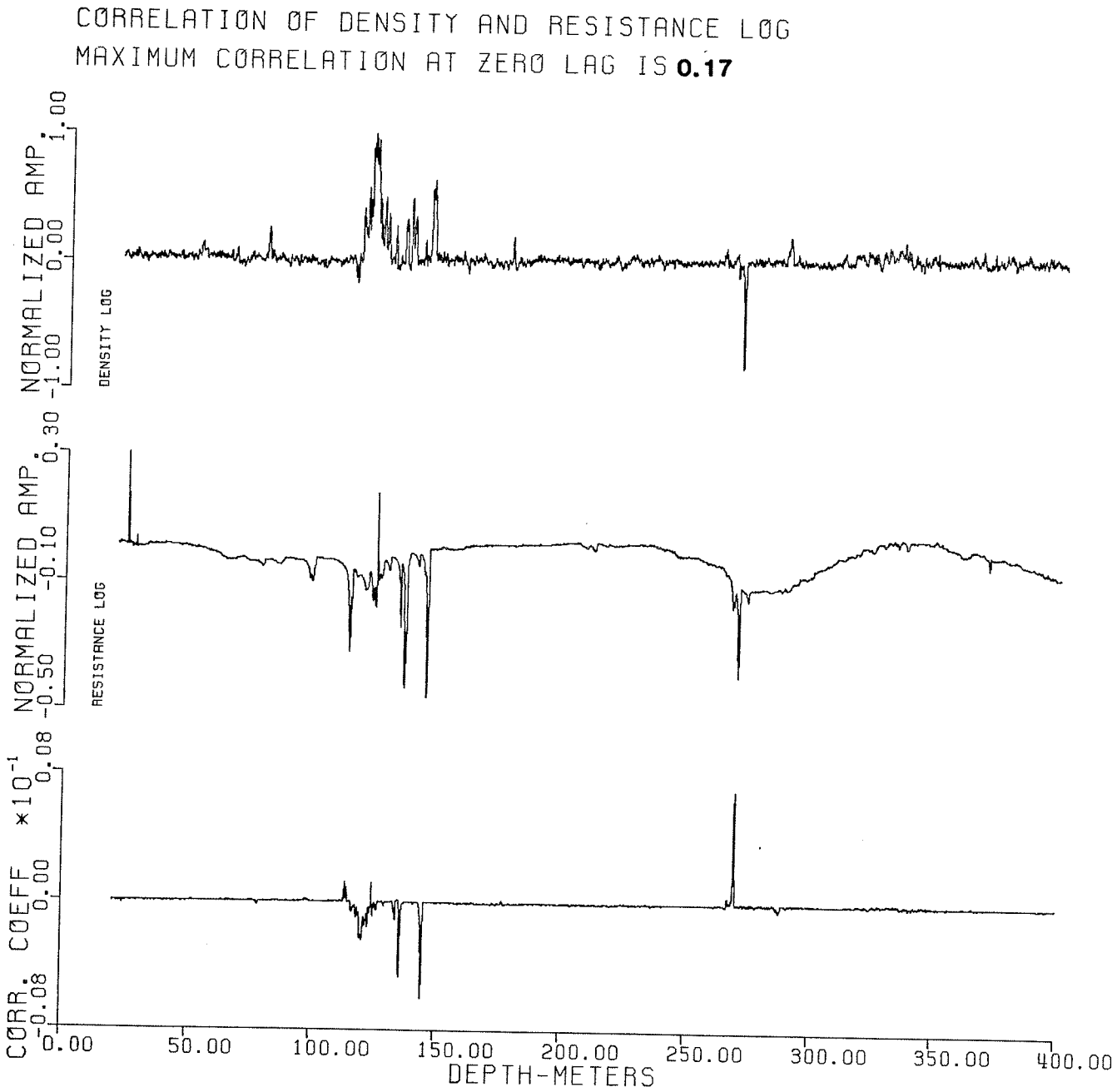

Fig.4.26: Correlation of density and resistance log.

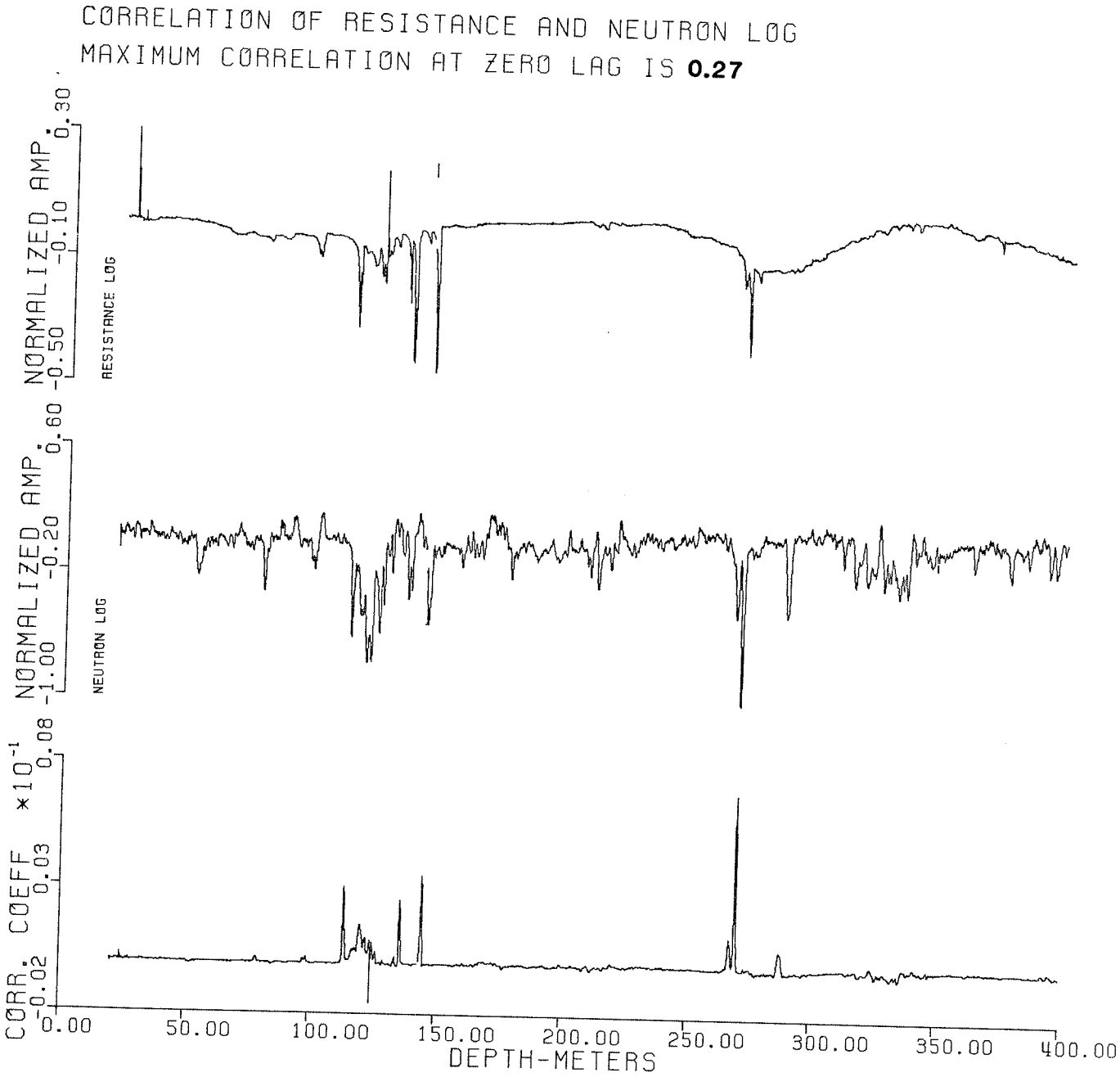

Fig.4.27: Correlation of resistance and neutron log.

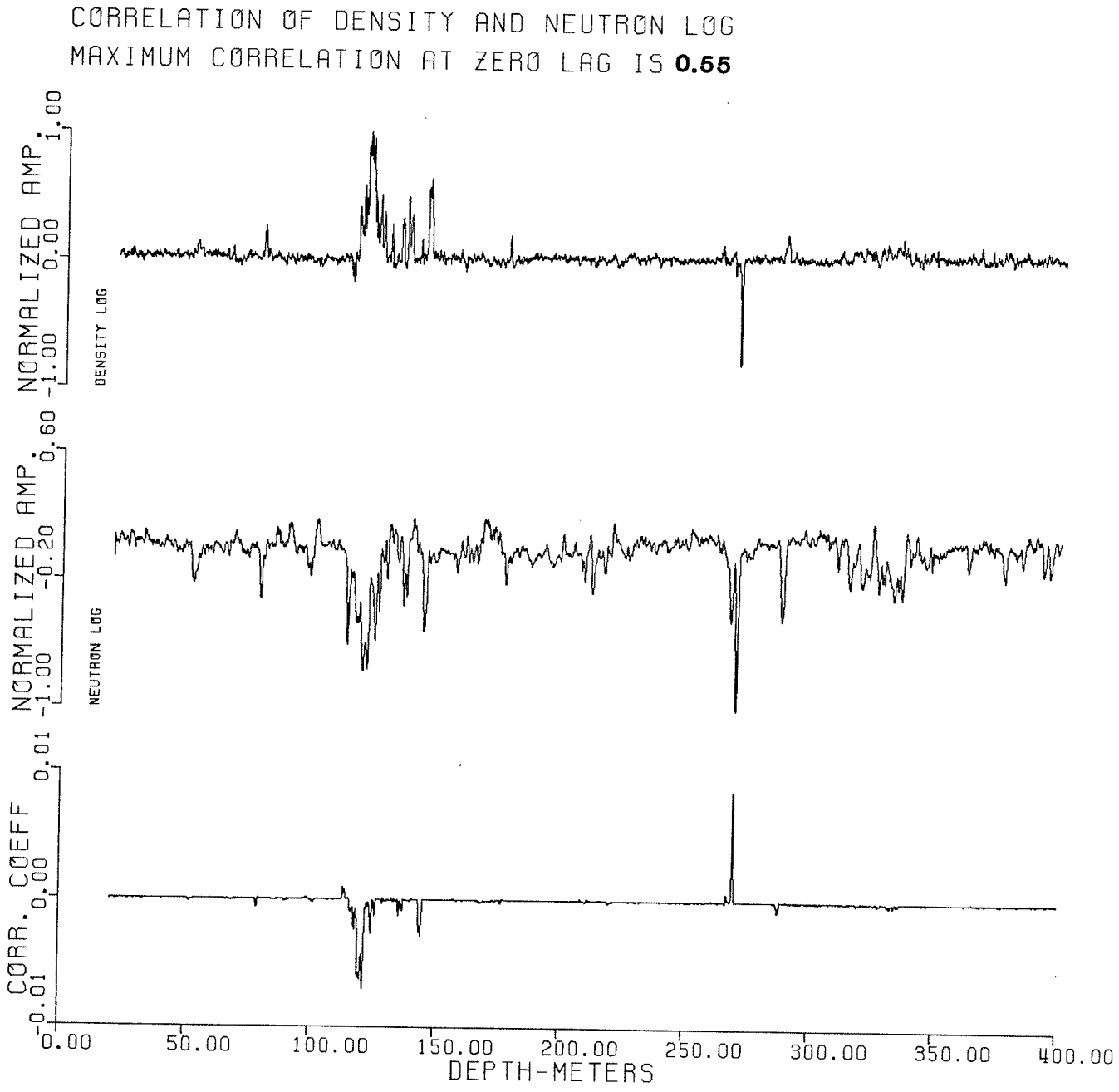

Fig.4.28: Correlation of density and neutron log.

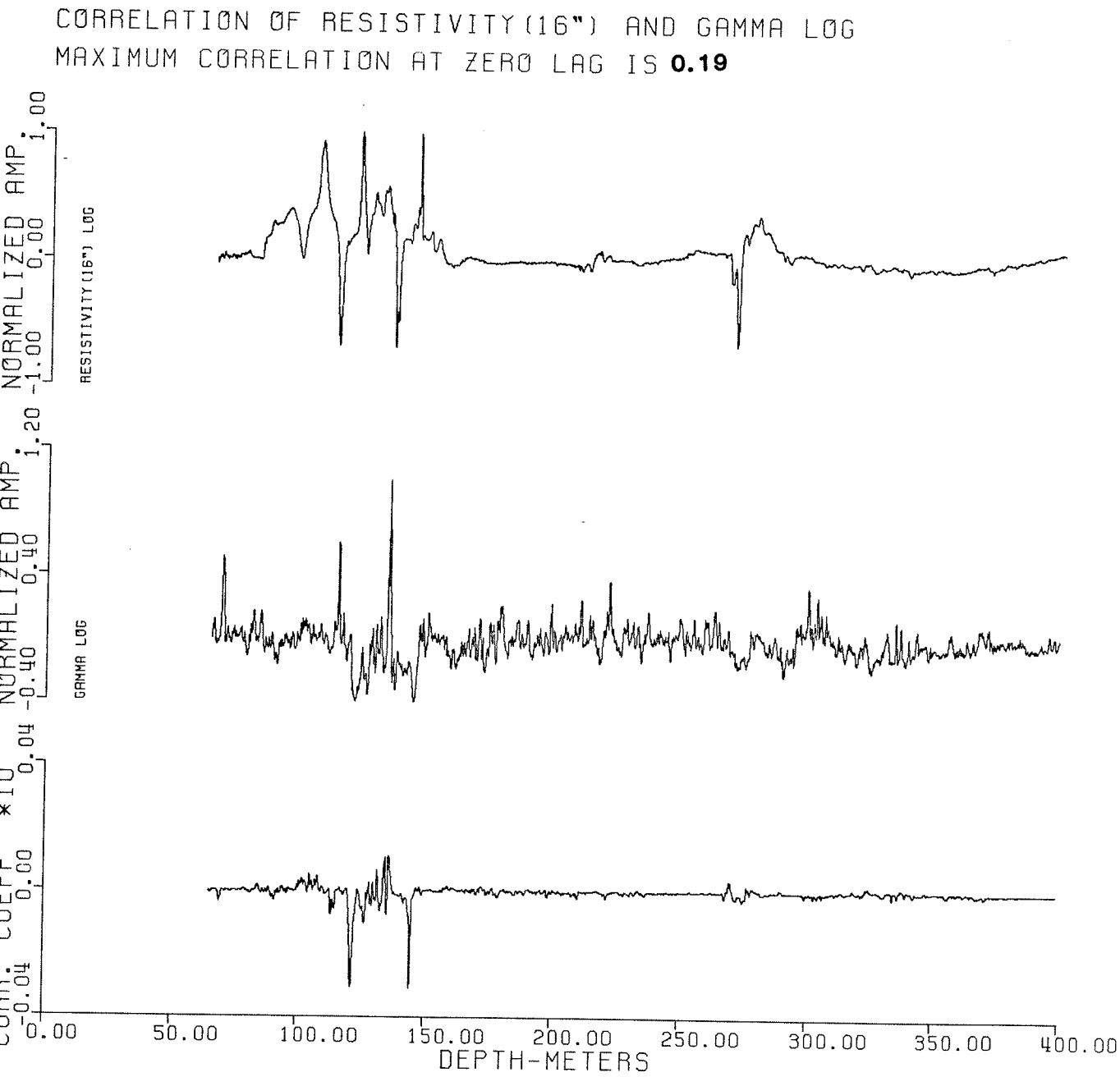

Fig.4.29: Correlation of resistivity(16'') and gamma log.

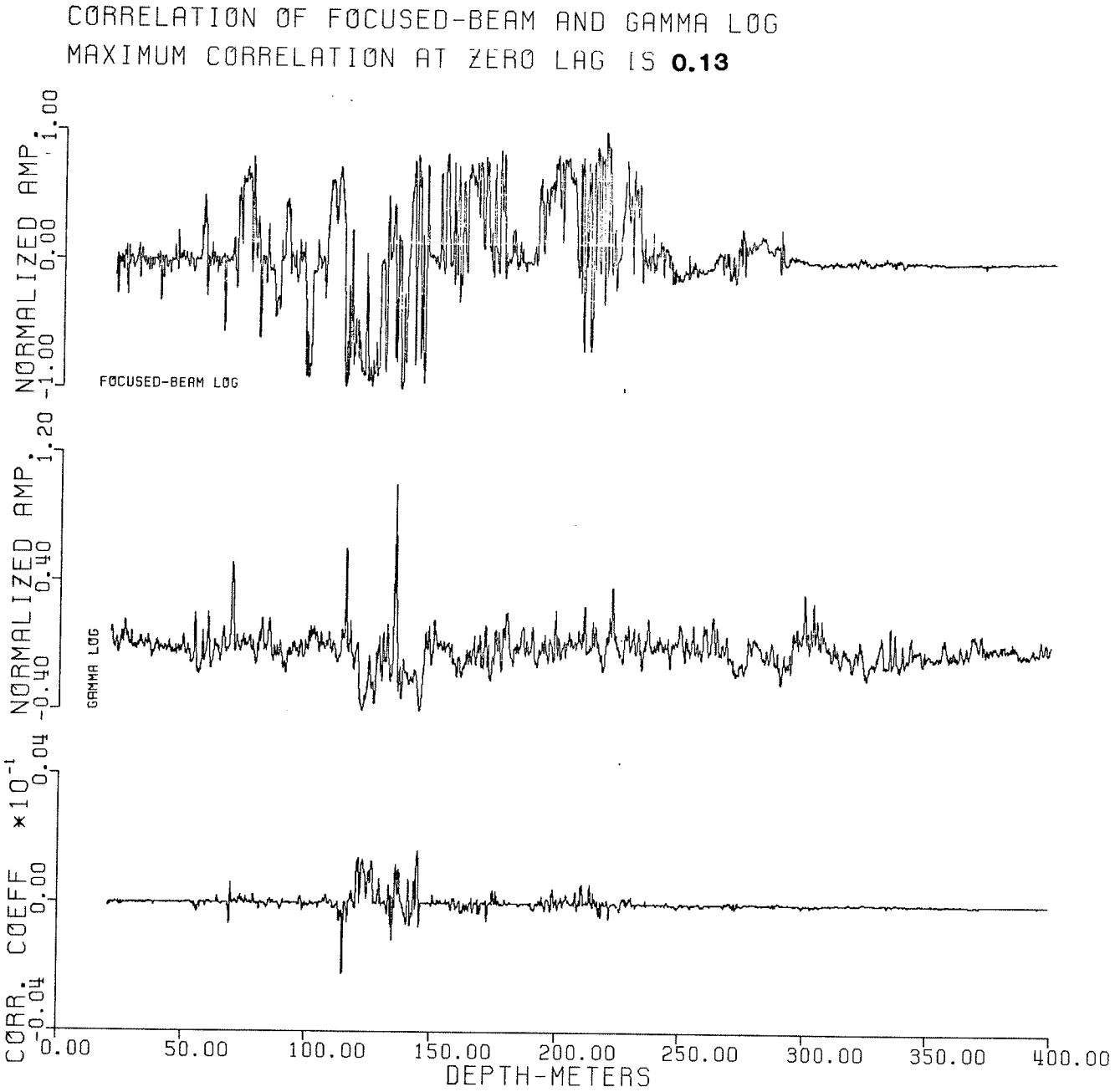

Fig.4.30: Correlation of focused-beam and gamma log.

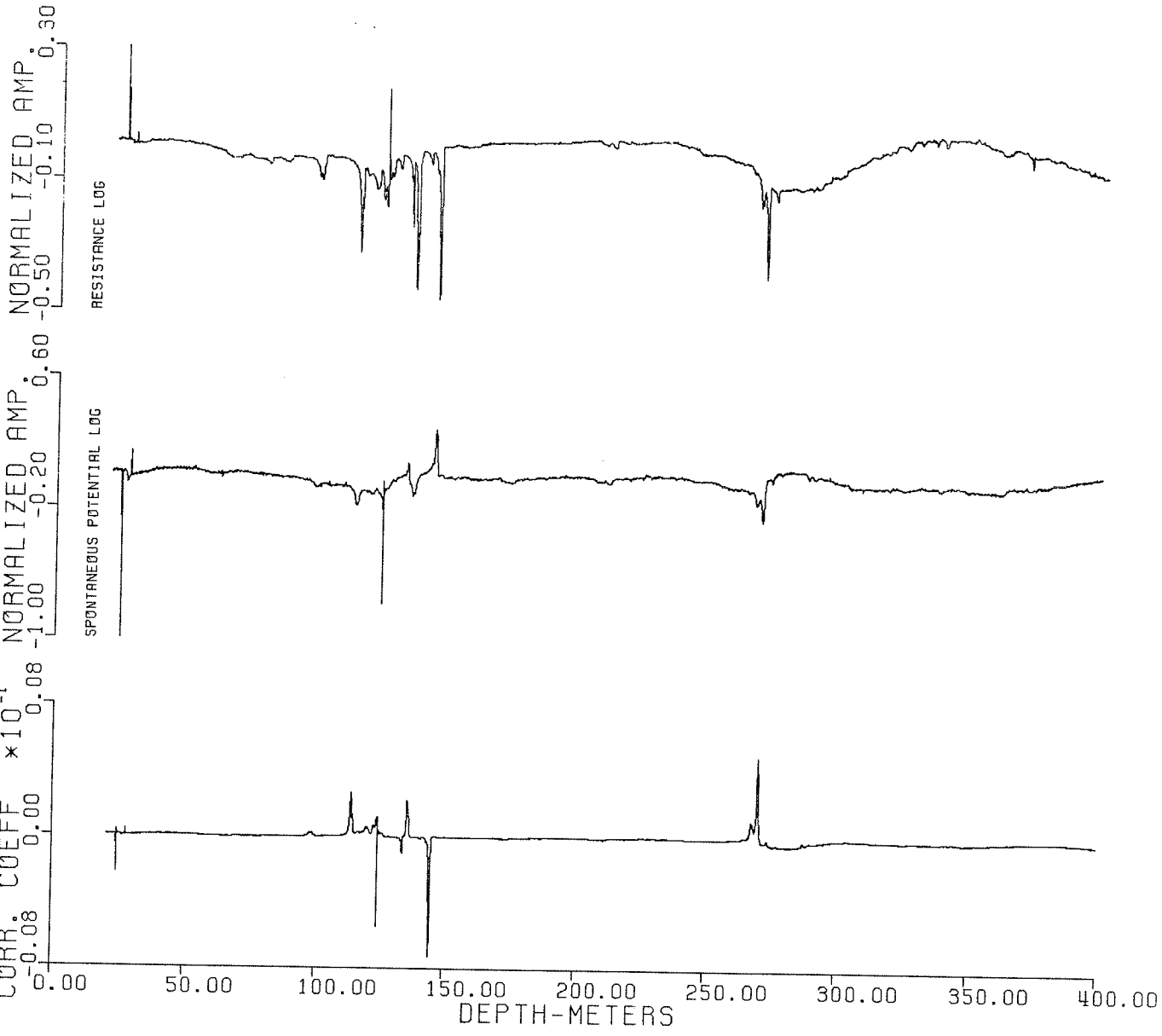

Fig.4.31: Correlation of resistance and spontaneous potential log.

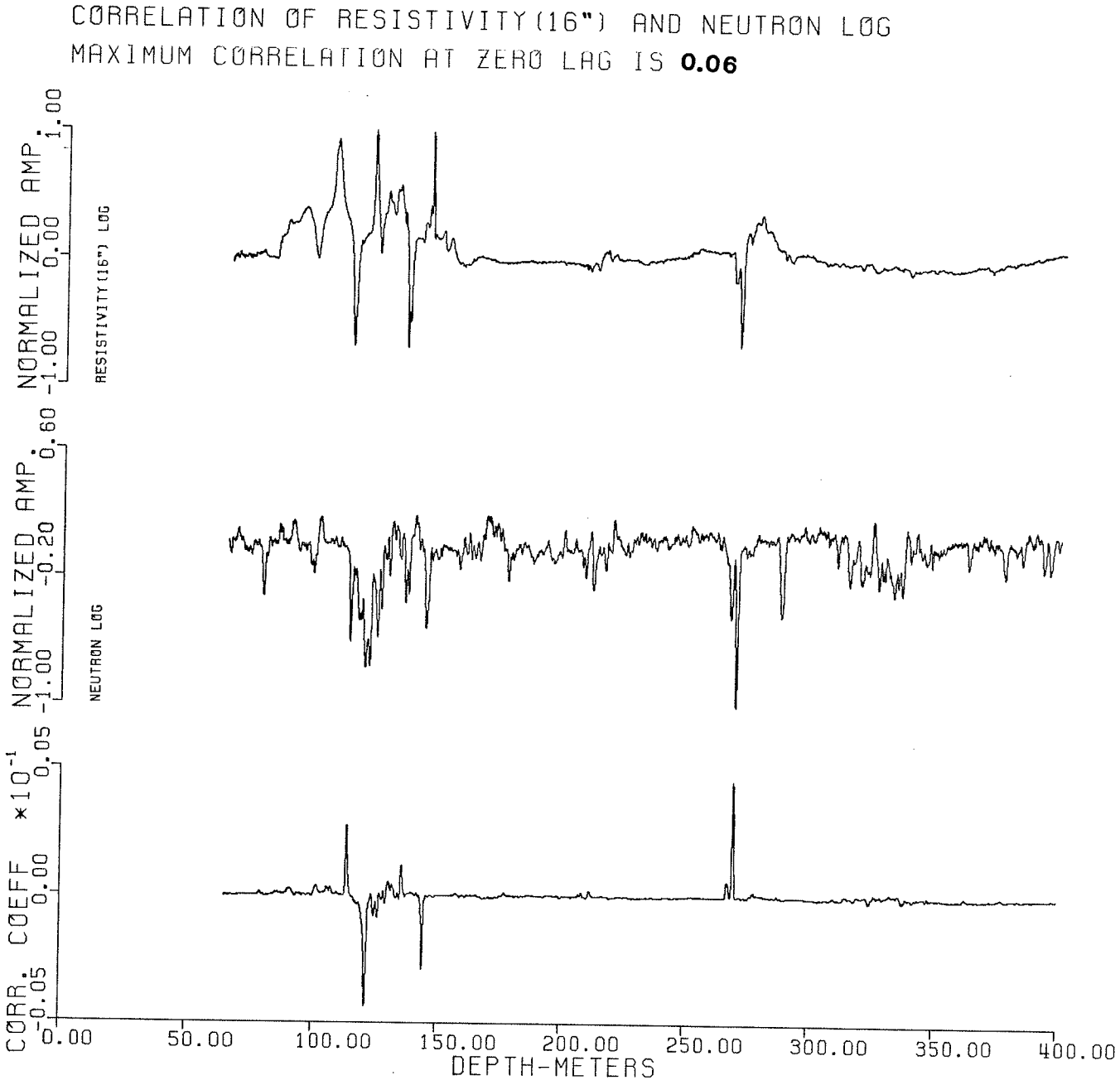

Fig.4.32: Correlation of resistivity(16'') and neutron log.

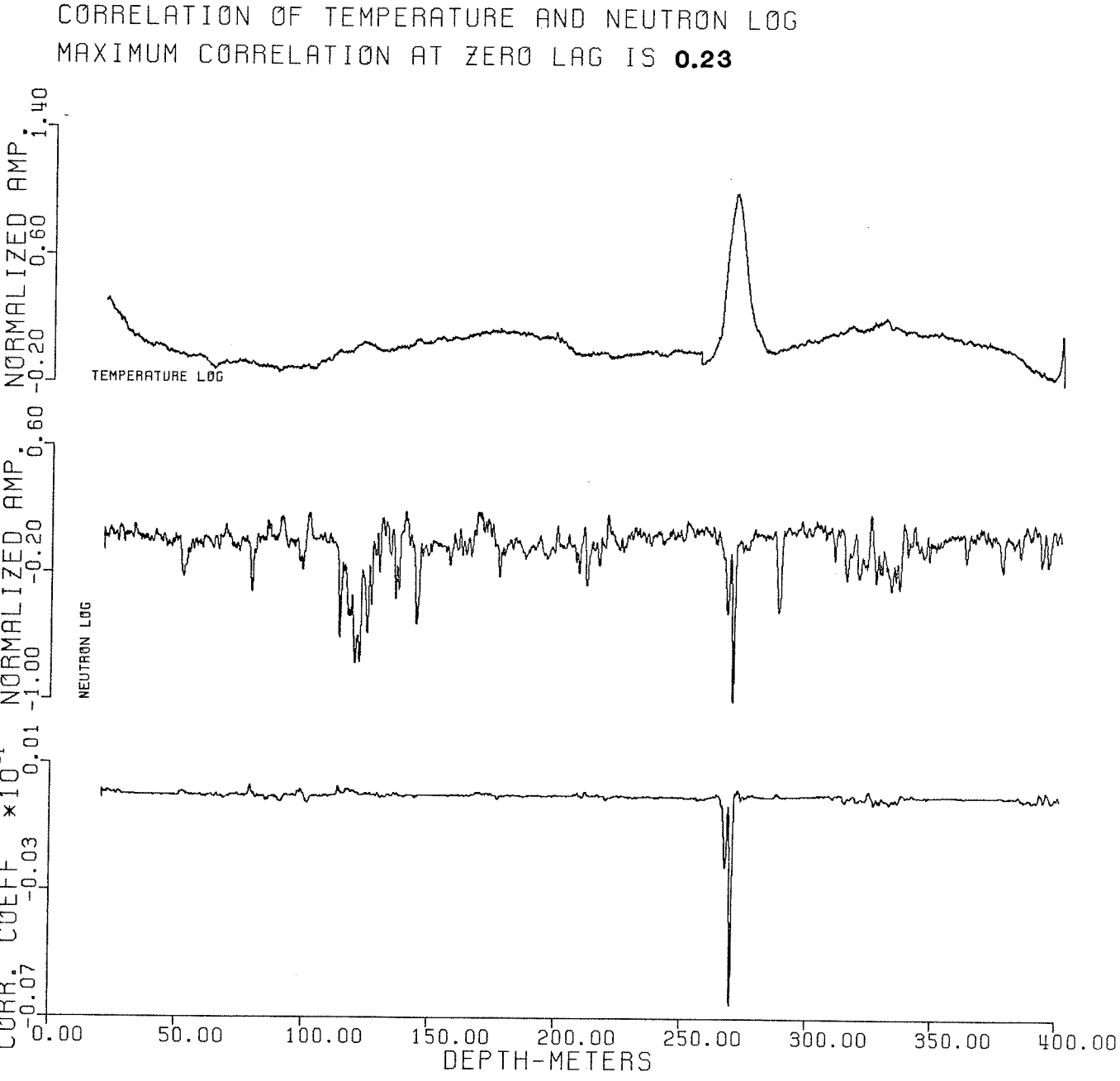

Fig.4.33: Correlation of temperature and neutron log.

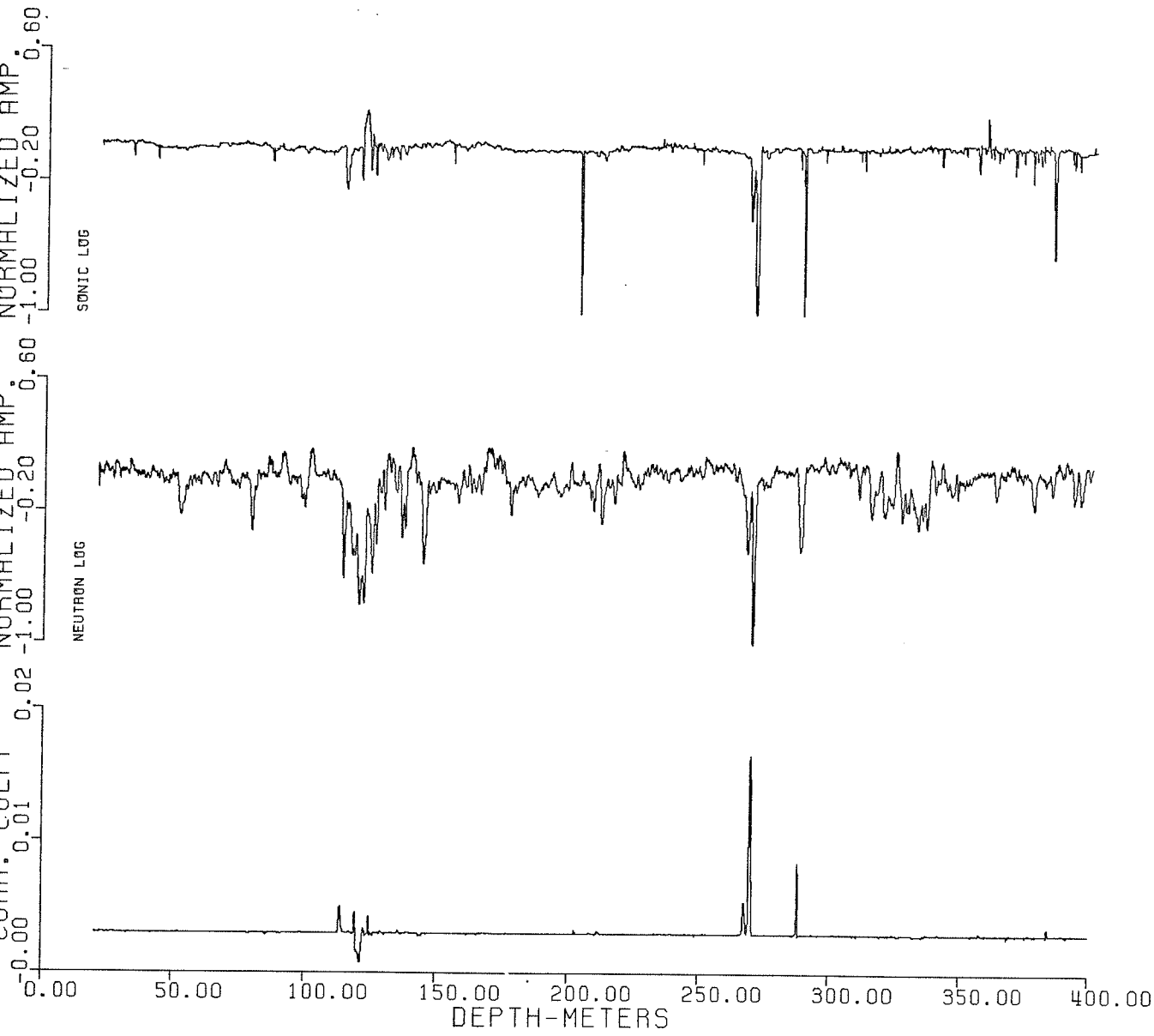

Fig.4.34: Correlation of sonic and neutron log.

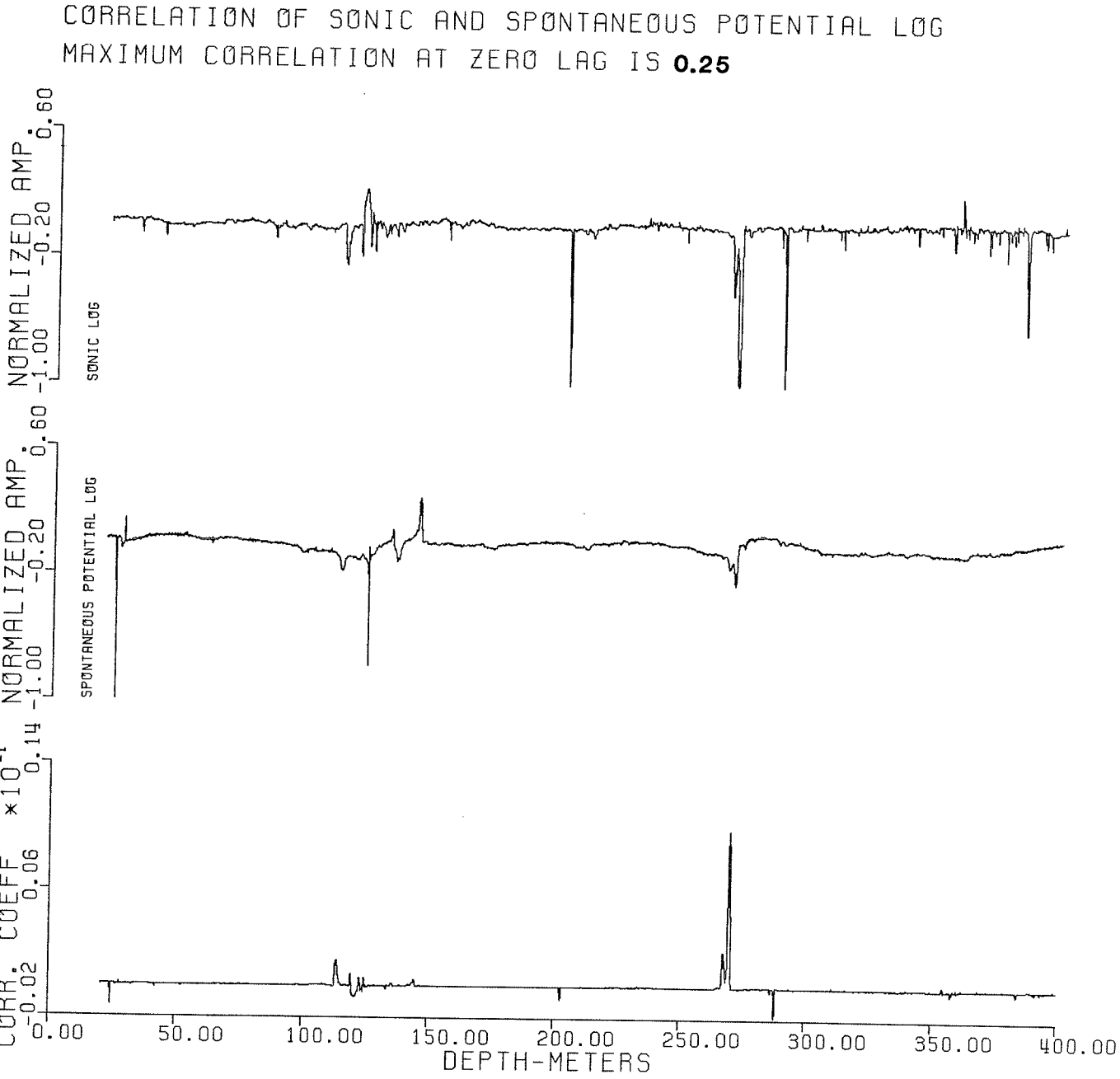

Fig.4.35: Correlation of sonic and spontaneous potential log.

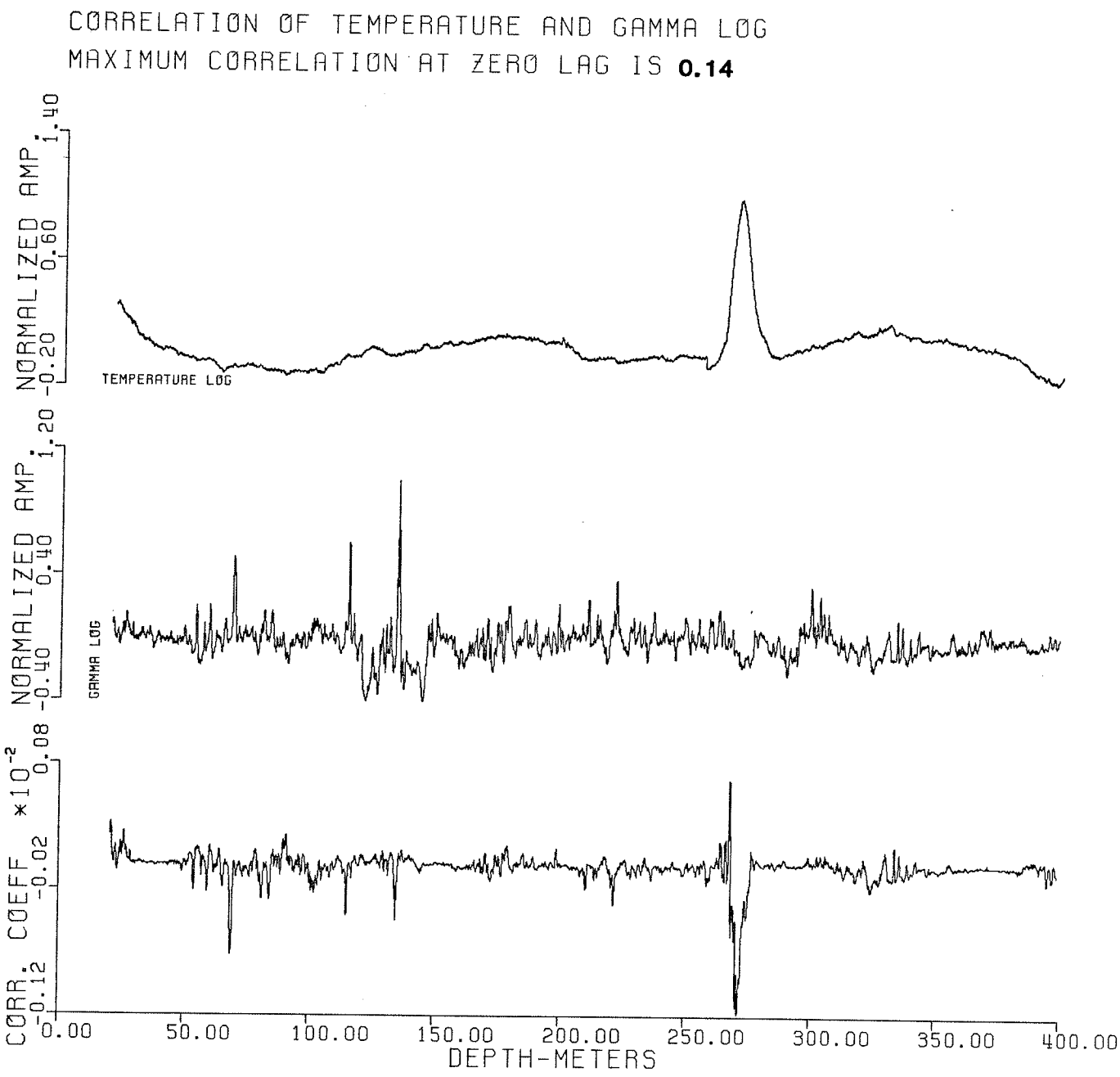

Fig.4.36: Correlation of temperature and gamma log.

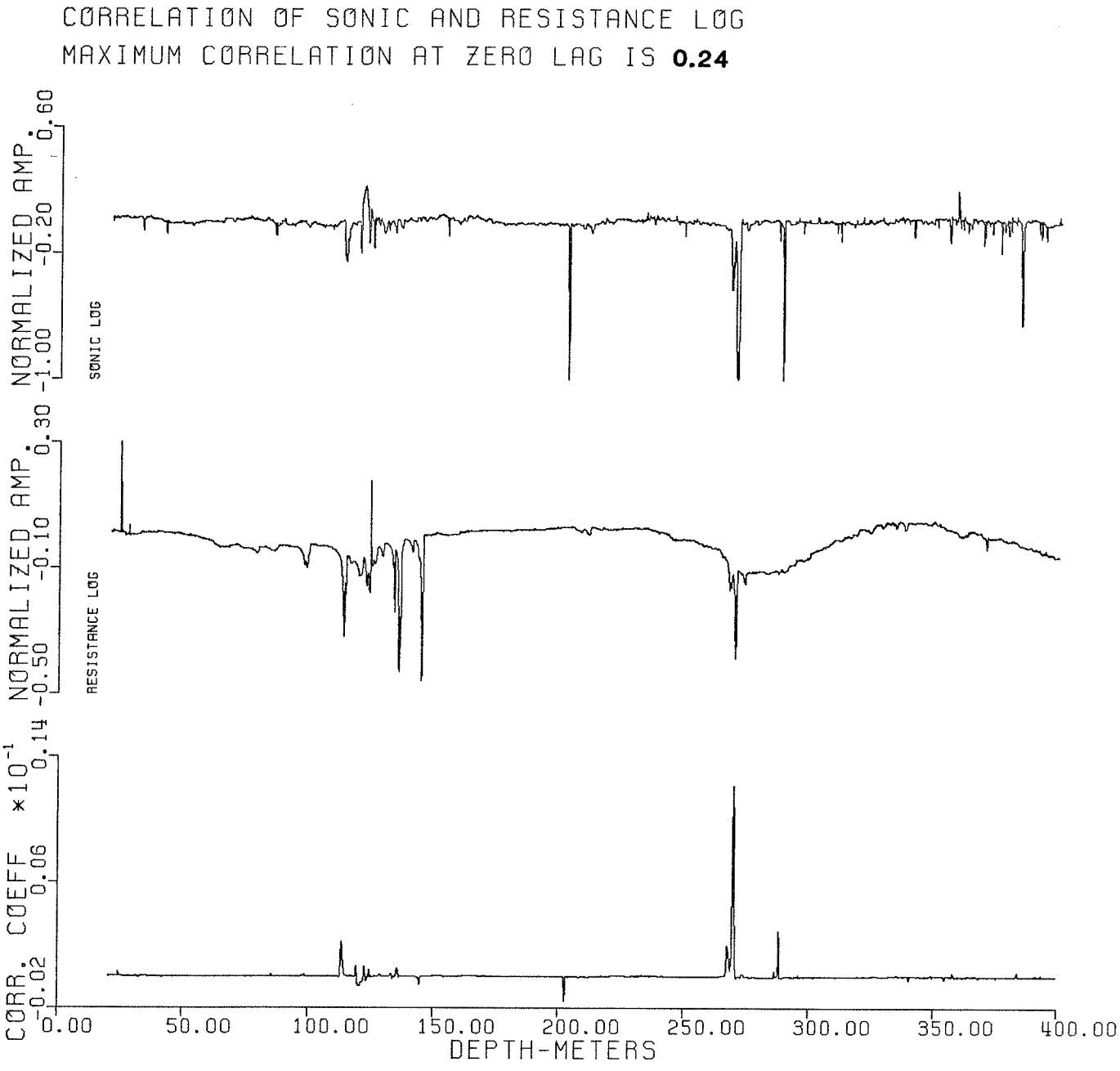

Fig.4.37: Correlation of sonic and resistance log.

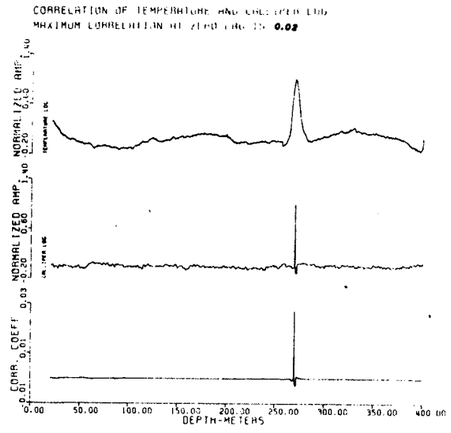

Fig.4.38: Correlation of temperature and caliper log.

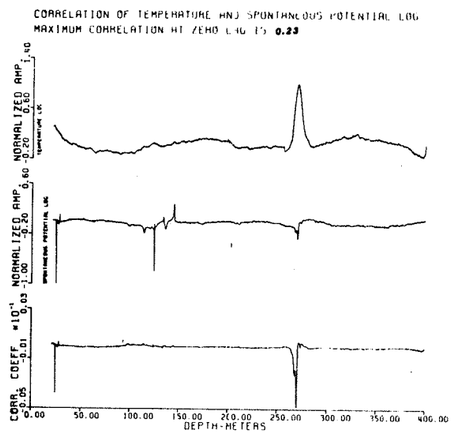

Fig.4.39: Correlation of temperature and spontaneous potential log.

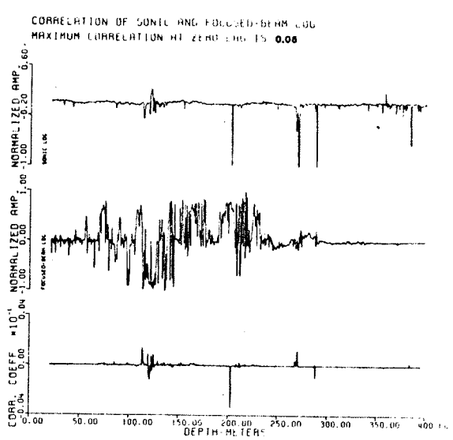

Fig.4.40: Correlation of sonic and focused-beam log.

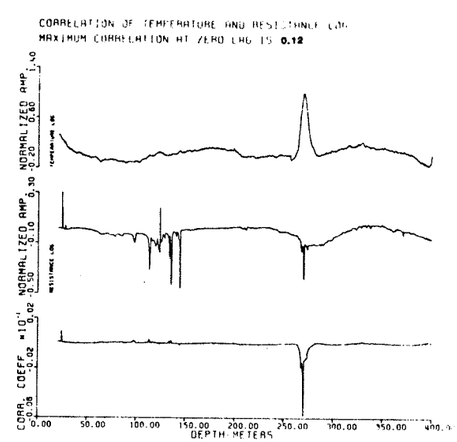

Fig.4.41: Correlation of temperature and resistance log.

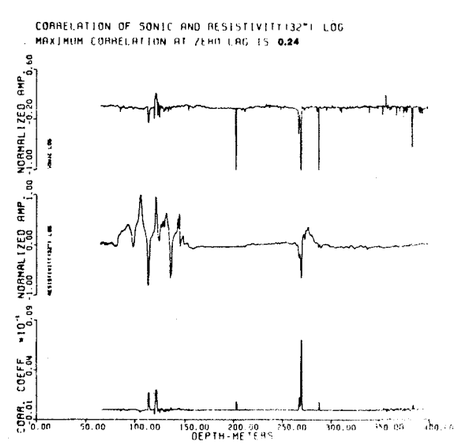

Fig.4.42: Correlation of sonic and resistivity(32'') log.

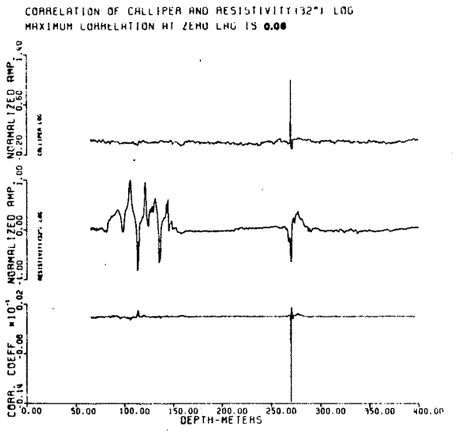

Fig.4.43: Correlation of caliper and resistivity(32'') log.

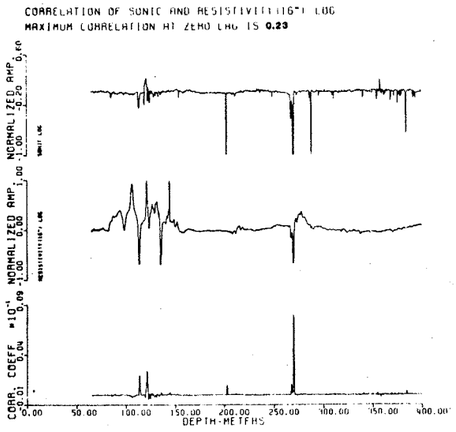

Fig.4.44: Correlation of sonic and resistivity(16'') log.

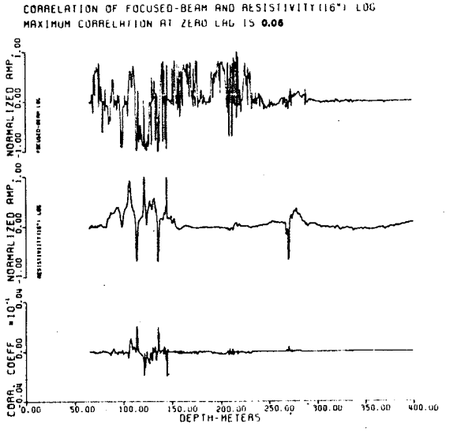

Fig.4.45: Correlation of focused-beam and resistivity(16'') log.

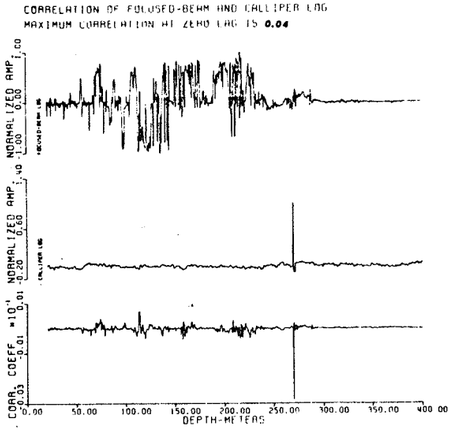

Fig.4.46: Correlation of focused-beam and caliper log.

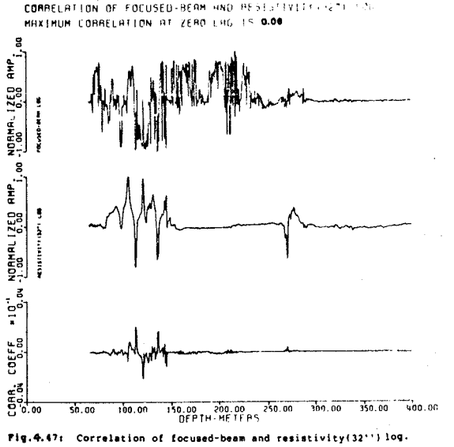

Fig.4.47: Correlation of focused-beam and resistivity(32'') log.

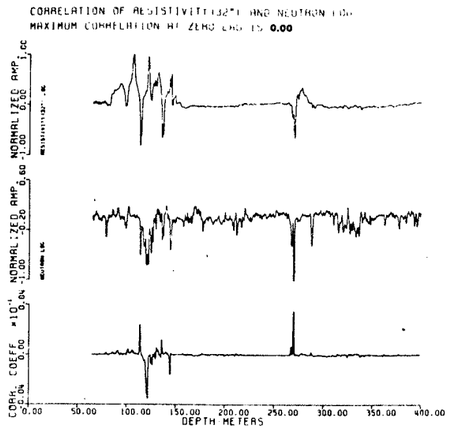

Fig.4.48: Correlation of resistivity(32'') and neutron log.

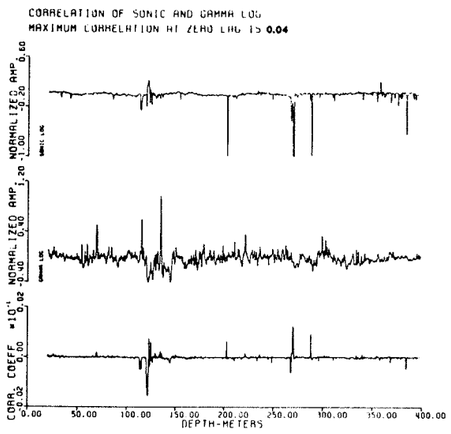

Fig.4.49: Correlation of sonic and gamma log.

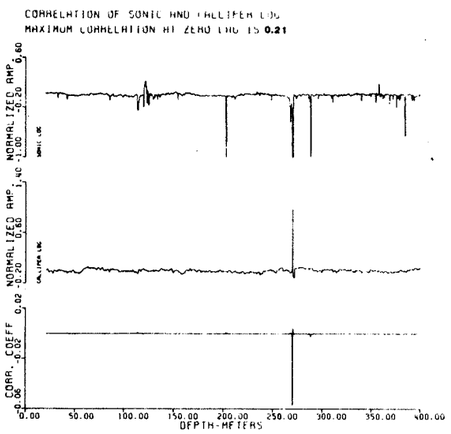

Fig.4.50: Correlation of sonic and caliper log.

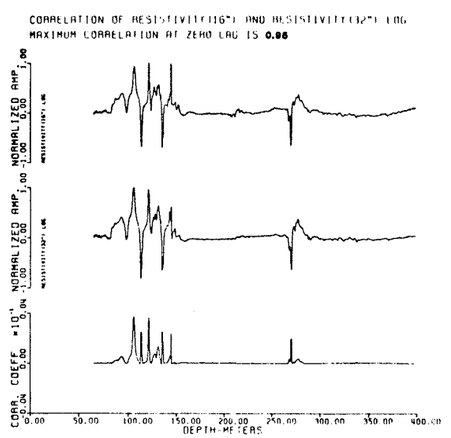

Fig.4.51: Correlation of resistivity(16'') and resistivity(32'') log.

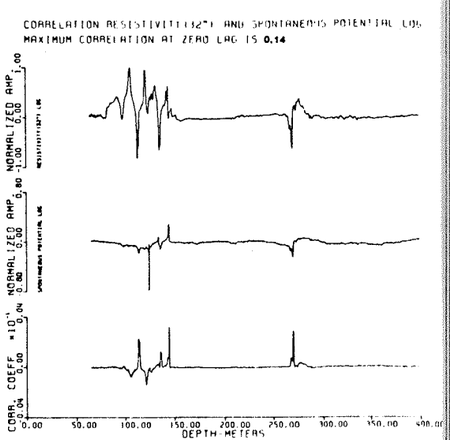

Fig.4.52: Correlation of resistivity(32'') and spontaneous potential l

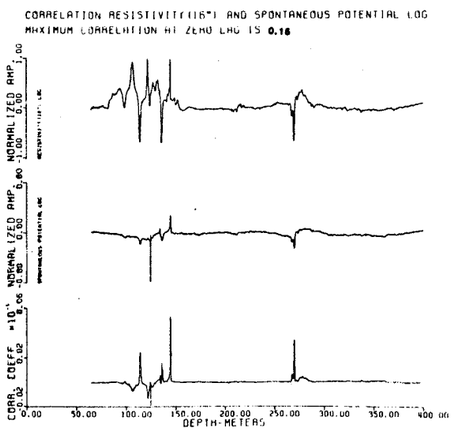

Fig.4.53: Correlation of resistivity(16'') and spontaneous potential log.

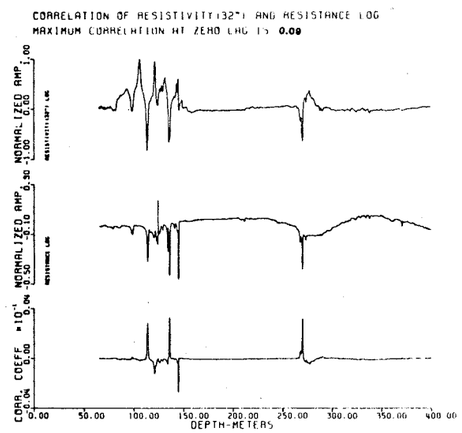

Fig.4.54: Correlation of resistivity(32'') and resistance log.

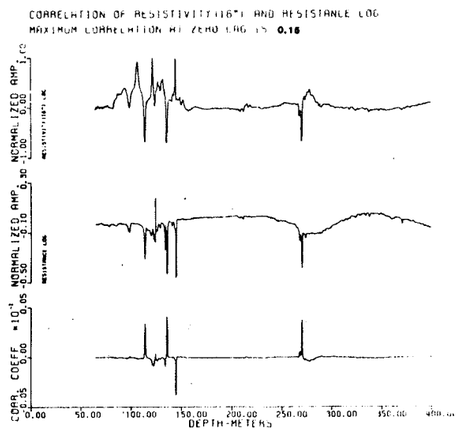

Fig.4.55: Correlation of resistivity(16'') and resistance log.

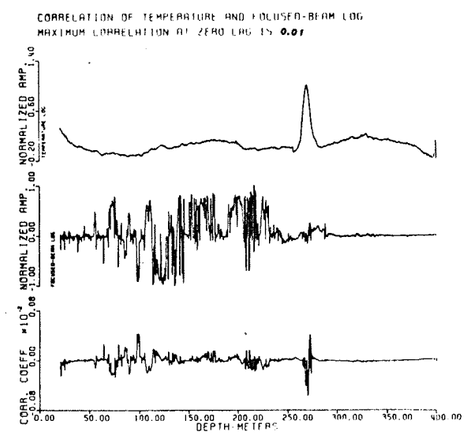

Fig.4.56: Correlation of temperature and focused-beam log.

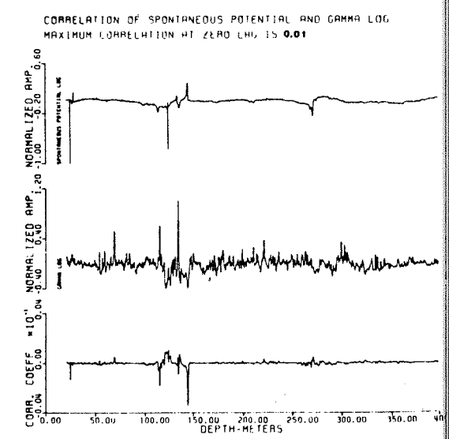

Fig.4.57: Correlation of spontaneous potential and gamma log.

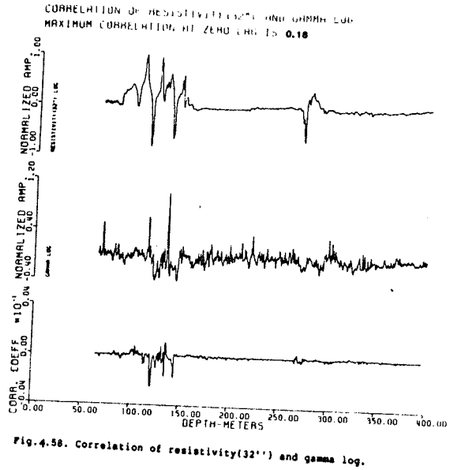

Fig.4.58. Correlation of resistivity(32'') and gamma log.

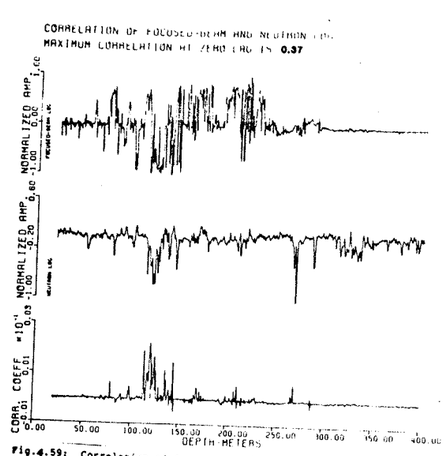

Fig.4.59: Correlation of focused-beam and neutron log.

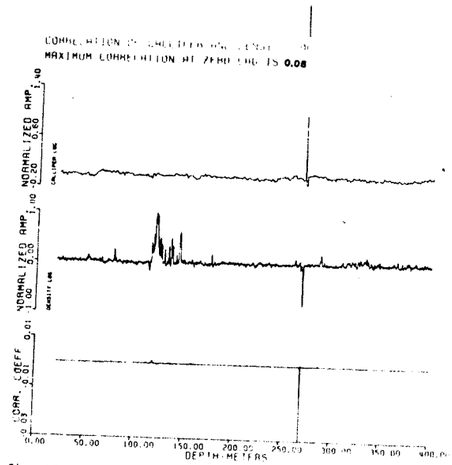

Fig.4.60: Correlation of caliper and density log.

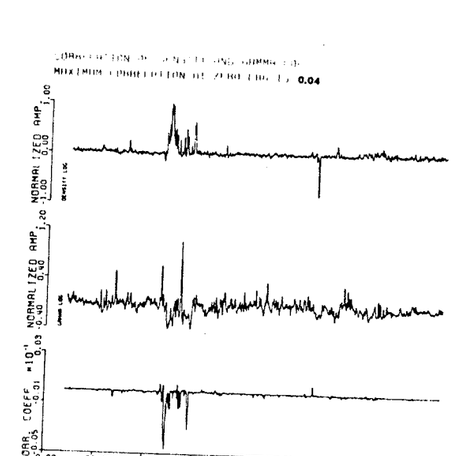

Fig.4.61: Correlation of density and gamma log.

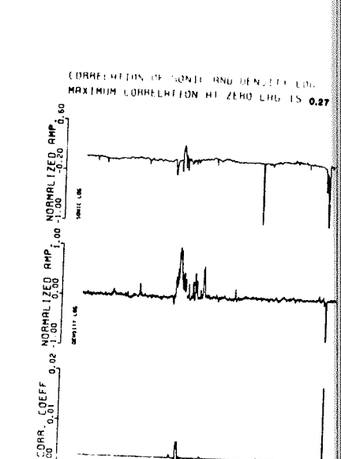

Fig.4.62: Correlation of sonic and density log.

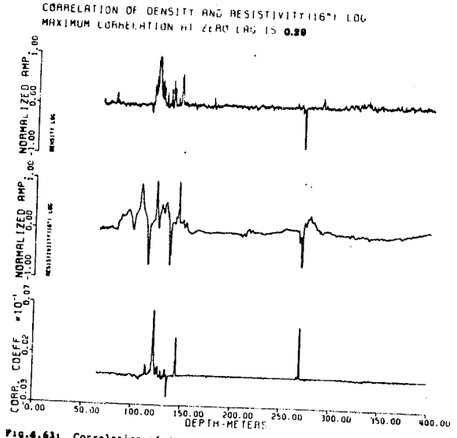

Fig.4.63: Correlation of density and resistivity(16'') log.

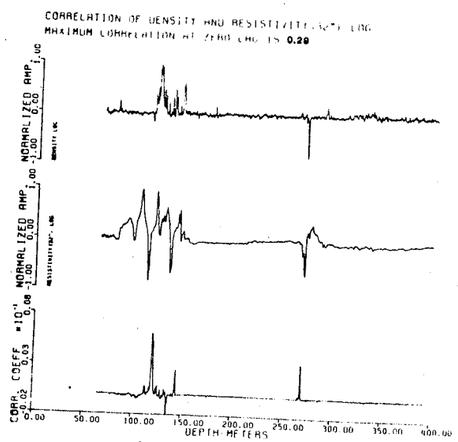

Fig.4.64: Correlation of density and resistivity(32'') log.

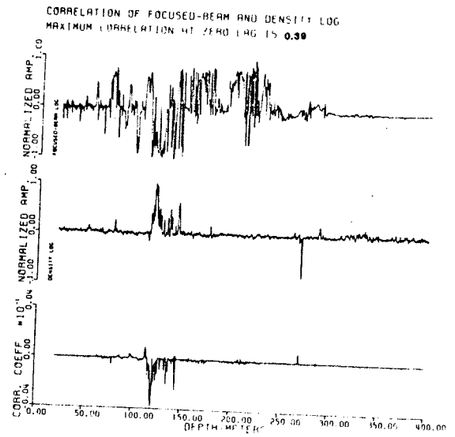

Fig.4.65: Correlation of focused-beam and density log.

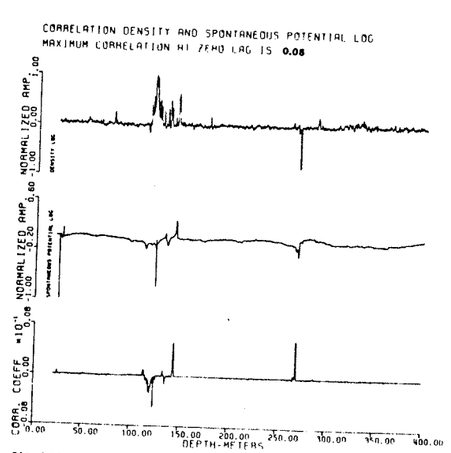

Fig.4.66: Correlation of density and spontaneous potential log.

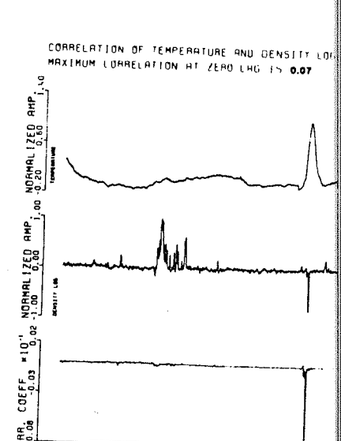

Fig.4.67: Correlation of temperature and density lo

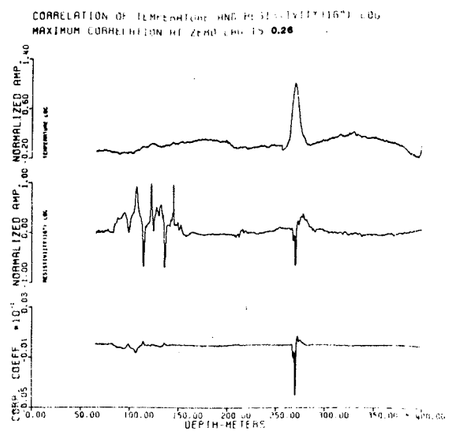

Fig.4.68: Correlation of temperature and resistivity(16'') log.

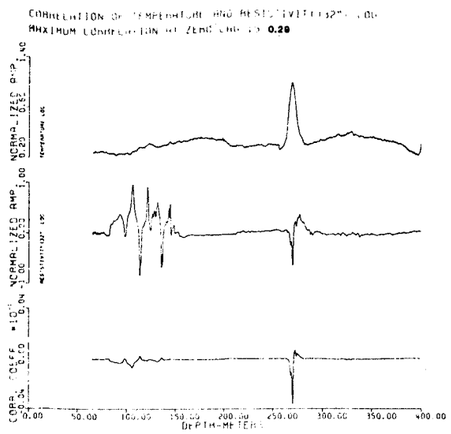

Fig.4.69: Correlation of temperature and resistivity(32'') log.

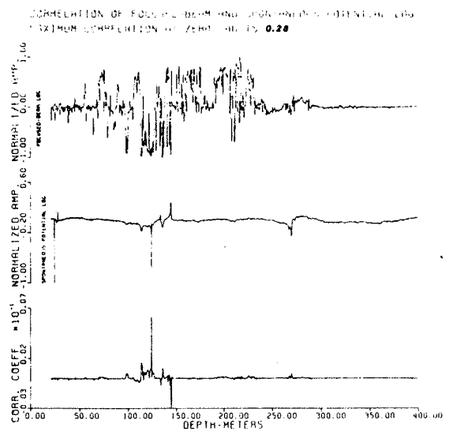

Fig.4.70: Correlation of focused-beam and spontaneous potential log.

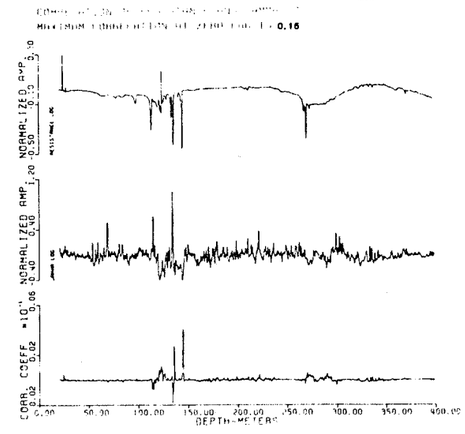

Fig.4.71: Correlation of resistance and gamma log.

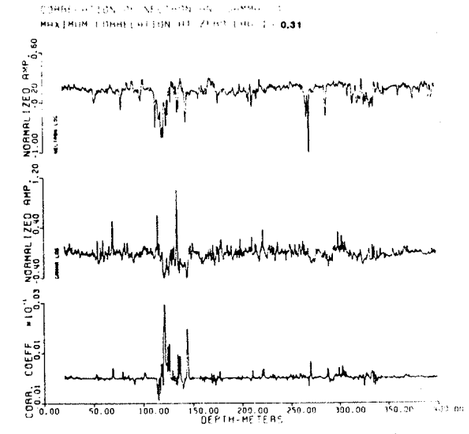

Fig.4.72: Correlation of neutron and gamma log.

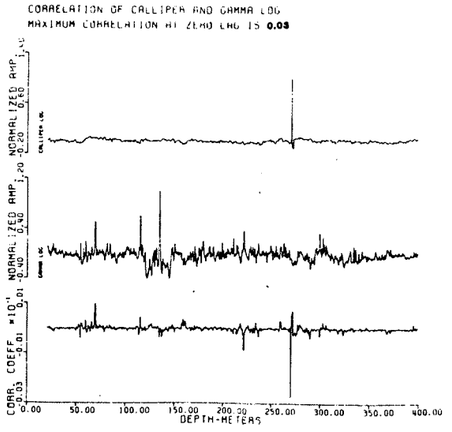

Fig.4.73: Correlation of caliper and gamma log.

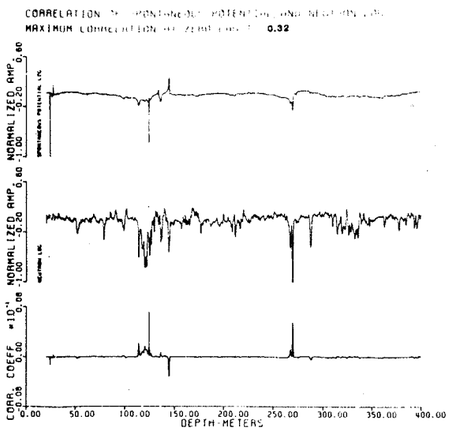

Fig.4.74: Correlation of spontaneous potential and neutron log.

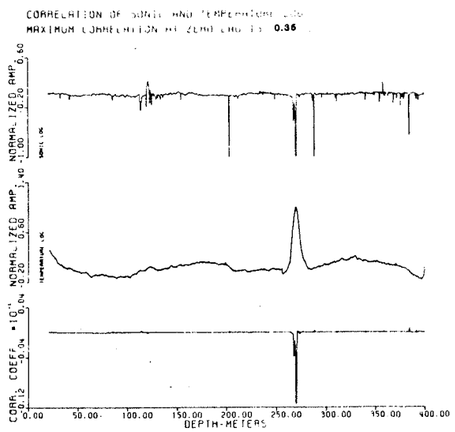

Fig.4.75: Correlation of sonic and temperature log.

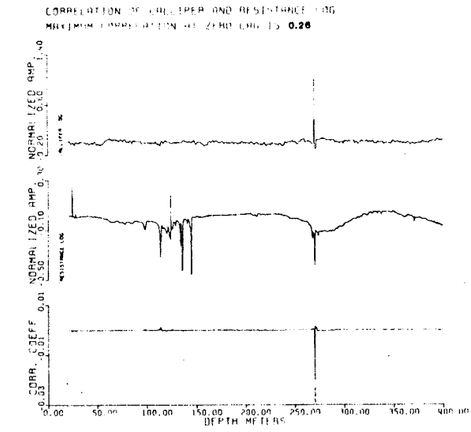

Fig.4.76: Correlation of caliper and resistance log.

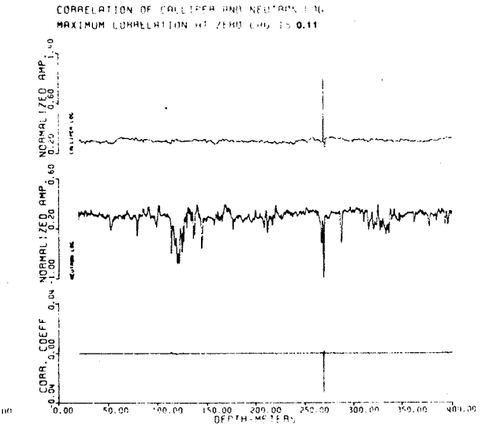

Fig.4.77: Correlation of caliper and neutron log.

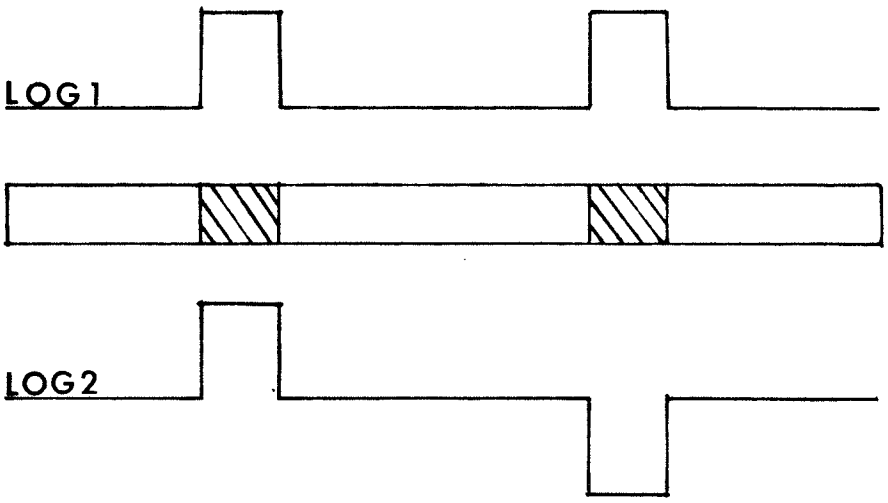

Fig.4.78: Two logs with different response within the same stratigraphic section.

logs. Also indicated in figures 4.15 through 4.25 are the cross-correlation values for the interval 90-150m and 267-272m. These values generally show improvement over the global correlation values. In some instances however, they are lower than the global correlation values. Examples of such instances are shown in the correlation of neutron-temperature(fig.4.33), sonic-neutron(fig.4.34), resistance-sonic (fig.4.37), temperature-gamma(fig.4.36) and sonic-spontaneous-potential(fig.4.35). In these cases, the total cross-correlation value is largely affected by the much stronger correlation at 267-272m. The correlation values for the 267-272m interval are generally higher. An exception to this general trend is the correlation involving the gamma log. This is because the gamma log does not show any significant anomaly within this particular interval. The large difference in the degree of correlation between two fracture zones can be attributed to the difference in the mineralogical and textural nature of the two fracture zones. The response of a particular log is determined by the parameters being measured; for example the presence of hematite within the 90-150m fracture zone is indicated by a high anomaly on the density log but a low anomaly on the neutron log because of the ability of iron to absorb thermal neutrons. The presence of different fracture infilling materials within the 90-150m fracture zone(mostly composed of chlorite, calcite, limonite and iron oxide) therefore gives rise to a wide variation of log responses.

Comparatively, the fracture zone at 267-272m has more open fractures and therefore less variation in the log responses. The results of the borehole television(Lau et al. 1983) indicate that the fracture zone at 267-272m has 0.6% of open fractures whiles the fracture at 90-150m has only 0.02% open fractures. A summary of the correlation is presented in table 3. The density, neutron and resistivity(16'') logs consistently give high correlation values whiles the gamma and caliper consistently give low values.

Systematic correlation has shown that geophysical logs can be used to characterize fractured zones in a granitic terrane. Two major fracture zones have been deduced from the well log data from borehole URL6. These are located at 98-150 m and 267-272 m. Other intervals where fracturing is apparent are 202.5-215 m and 286.5-289.4 m. Results of cross-correlation analysis performed for different pairs of well log data indicate that the value of the cross-correlation coefficient depends on the mineralogical and textural nature of the formation, and may not always be a good measure of the agreement betweem various logs in detecting fracture zones.

TABLE 3

A summary of cross-correlation of geophysical logs.

LOG	INTERVAL	HIGHEST CORRELATION	LOWEST CORRELATION
Density	267-272m	Neutron	Gamma
Density	90-150m	Neutron	Temperature
Density	Total	Neutron	Spontaneous
Neutron	267-272m	Sonic Resist.(16'')	Gamma
Neutron	90-150m	Focused-beam	Caliper
Neutron	Total	Density	Resist.(32'')
Spontaneous	267-272m	Resist.(16'')	Gamma
Spontaneous	90-150m	Neutron	Density
Spontaneous	Total	Focused-beam	Caliper
Temperature	267-272m	Resistance	Caliper
Temperature	90-150m	Resist.(16'')	Gamma
Temperature	Total	Sonic	Focused-beam
Gamma	267-272m	Temperature	Focused-beam
Gamma	90-150m	Density	Temperature
Gamma	Total	Density	Spontaneous
Resistance	267-272m	Neutron	Caliper
Resistance	90-150m	Focused-beam	Sonic
Resistance	Total	Focused-beam	Resist.(32'')
Resist.(32'')	267-272m	Resist.(16'')	Caliper
Resist.(32'')	90-150m	Resist.(16'')	Focused-beam
Resist.(32'')	Total	Resist.(16'')	Neutron
Resist.(16'')	267-272m	Neutron	Gamma
Resist.(16'')	90-150m	Resist.(32'')	Focused-beam
Resist.(16'')	Total	Resist.(32'')	Neutron
Focused-beam	267-272m	Spontaneous	Caliper Gamma
Focused-beam	90-150m	Neutron	Resist.(16'')
Focused-beam	Total	Density	Temperature
Caliper	267-272m	Sonic	Neutron
Caliper	90-150m	Sonic	Neutron
Caliper	Total	Resistance	Spontaneous
Sonic	267-272m	Resist.(16'')	Caliper Gamma
Sonic	90-150m	Density	Focused-beam
Sonic	Total	Temperature	Gamma

Chapter V

WKBJ SYNTHETIC SEISMOGRAM FOR VERTICAL SEISMIC PROFILING AT URL SITE.

Vertical seismic profiling is a relatively new seismic technique which is becoming increasingly popular in seismic exploration. It offers a wide variety of applications to reflection seismic exploration problems(Kennet et al., 1980; Balch et al., 1982; Gal'perin, 1973). With VSP, one can observe a seismic waveform that is incident upon a horizon of interest and also the resultant reflection and transmitted waveforms. The source waveform and its evolution as it travel through the earth can be observed. One can track reflected waveform upward, nearly to the ground surface, and study the waveform as it is distorted by the medium. Additionally, one can use VSP data to make a highly reliable tie between a well log and a surface profile run across the well.

In this chapter, using the data from the sonic and density logs , WKBJ theoretical seismogram for Vertical Seismic Profiling will be generated to illustrate the application of the VSP in detecting subsurface fracture zones.

5.1 DESCRIPTION OF VSP METHOD.

An idealized cross-sectional view of a conventional VSP lay-out is shown in figure 5.1(a). The seismic source, S, located at the surface is energized, and recording is made at one level at a time with a geophone, G, clamped in the well. The ray A, represents the direct arrival. The rays B and C, respectively represent single and multiple reflected events travelling upward into the geophone. The ray D, represents a multiple reflected event travelling downwards into the geophone. This event is not observed at the surface. Figure 5.1(b) represents the configuration being used for the URL experiment. This is achieved by interchanging the positions of the geophone and the shot point for the conventional VSP layout. By the Reciprocity Theorem, the seismic travel time characteristics should be the same for both configurations. With the URL configuration, only the direct and upgoing reflected events can be recorded. The downgoing reflected events in the conventional VSP, become upgoing reflected events in the URL configuration.

5.2 REVIEW OF THE WKBJ THEORY.

Several methods have been used in the computation of theoretical seismograms. These include the reflectivity method(Fuchs and Muller, 1971), the generalized ray method(Wiggins and Helmberger, 1974) and the full-wave theory

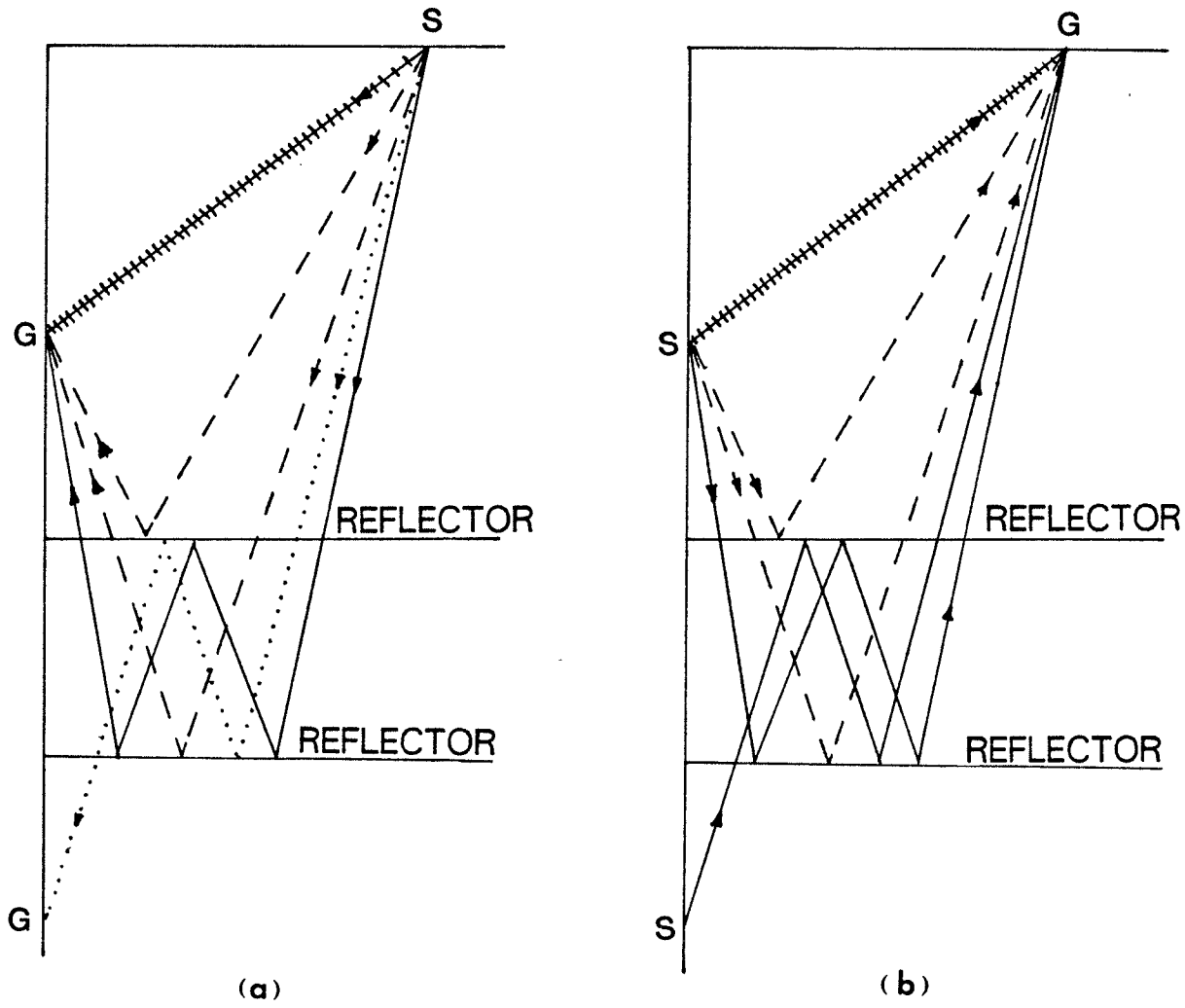

Fig.5.1: Schematic drawing of (a) a typical VSP field configuration, (b) configuration for the URL6 experiment.

method(Cormier and Richards, 1977). These methods are complicated and expensive so that their use is limited to a few trial models. To alleviate this situation, a number of approximate methods have been developed. One of such techniques devised by Chapman(1978), evaluates the inverse transform of the displacement field using the WKBJ approximation to the solution of the wave equation. This theoretical seismogram has been called the WKBJ seismogram. Compared to the other methods, this method is fast and requires far less computational time.

5.2.1 The WKBJ approximation.

For a two-dimensional medium where the parameters are functions of the vertical coordinate z and the horizontal coordinate x, the response to a point source can be obtained by taking the Fourier transform with respect to time t and horizontal distance x of the equation of motion and the constitutive equations. These transforms reduce the two-dimensional, partial-differential, elastodynamic equations to an ordinary differential equation with independent variable z. By applying the appropriate radiation and boundary conditions, this can be solved for the transform response $\hat{\hat{u}}(\omega,p)$ where ω is the frequency and p is the ray parameter of the ray of interest(Chapman, 1978). The response u(t,x) at a receiver located at x is obtained from the inverse transform of the transformed response.

This is given by

$$U(t,x) = \frac{1}{4\pi^2} \int_B \int_{-\infty}^{\infty} \hat{\tilde{u}}(\omega,p)\,|\omega| \exp\{-i\omega(t-px)\}\,dp\,d\omega \qquad 5.2.1\text{-}1$$

where B represents the Bromwich contour. By changing the order of the integration in equation 5.2.1-1 and rewriting $|\omega|$, we obtain

$$U(t,x) = -\frac{1}{4\pi^2} \int_{-\infty}^{\infty} \int_B \hat{\tilde{u}}(\omega,p)(-i\omega)(-i\,sgn(\omega)) \exp\{-i\omega(t-px)\}\,d\omega\,dp \qquad 5.2.1\text{-}2$$

Performing the inverse Fourier transform in equation 5.2.1-2, we obtain

$$U(t,x) = -\frac{1}{2\pi} \int_{-\infty}^{\infty} \tilde{u}^{+}(t-px,p)\,dp \qquad 5.2.1\text{-}3$$

where $\tilde{u}^{+}(t-px,p)$ is a time derivative of the Hilbert transform of $\tilde{u}(t-px,p)$. The seismogram are obtained by integrating the real function $\tilde{u}^{+}(t-px,p)$ along different straight lines of the form t-px. The transformed function $\hat{\tilde{u}}(\omega,p)$ can be factored as

$$U(\omega,p) = \hat{S}(\omega)\,\hat{\tilde{V}}(\omega,p) \qquad 5.2.1\text{-}4$$

where $s(\omega)$ contains the source function and the transfer function of the geophones. Equation 5.2.1-3 can thus be

re-written as

$$U(t,x) = -\frac{1}{2\pi}\frac{d}{dt} S(t) * \int_{-\infty}^{\infty} \bar{\tilde{v}}(t-px,p)\,dp \qquad 5.2.1-5a$$

$$= -\frac{1}{2\pi}\frac{d}{dt} \bar{s}(t) * \int_{-\infty}^{\infty} \tilde{v}(t-px,p)\,dp \qquad 5.2.1-5b$$

where $\bar{\tilde{v}}(t-px,p)$ and $\bar{s}(t)$ are the Hilbert transform of $\tilde{v}(t-px,p)$ and $s(t)$ respectively. In this method, the WKBJ approximation for $\bar{\tilde{v}}(t-px,p)$ and $\tilde{v}(t-px,p)dp$ are used. This approximation is valid only at frequencies that are large compared to the velocity gradients of the medium. We will now examine equation 5.2.1-3 for a turning ray, direct ray and a reflected ray.

5.2.1.1 Turning Ray.

The WKBJ approximation for a turning ray can be written, as given by Chapman(1978),

$$\hat{\tilde{V}}(\omega,p) = i\,\mathrm{sgn}(\omega)\exp\{i\omega\tau(p)\}\,R(p) \qquad 5.2.1.1-1$$

where $\tau(p)$ is the vertical-slowness integral given by

$$\tau(p) = 2\int_{z_a}^{z} q(p,\xi)\,d\xi \qquad 5.2.1.1-2$$

and z_a represents the depth of maximum penetration of the turning ray. The function R(p) contains the source and

receiver directivity functions and a product of any transmission coefficients on the ray. If we make the following substitution in equation 5.2.1-5a

$$\tilde{\tilde{V}}(t,p) = -R(p)\,\delta(t-\tau(p)) \qquad 5.2.1.1-3a$$

$$\theta(p,x) = px + \tau(p) \qquad 5.2.1.1-3b$$

The displacement field of the turning ray reduces to

$$U(t,x) = \frac{1}{2\pi}\frac{d}{dt}\,S(t) * \int_{-\infty}^{\infty} R(p)\,\delta(t-\theta(p,x))\,dp \qquad 5.2.1.1-4a$$

$$= \frac{1}{2\pi}\,\dot{S}(t) * \sum_{t=\theta(p,x)} \frac{R(p)}{|\theta'(p,x)|} \qquad 5.2.1.1-4b$$

The terms in the summation are evaluated for all solution of the equation $t=\theta(p,x)$

5.2.1.2 Direct ray.

The WKBJ approximation for the direct ray can be written as

$$\tilde{\tilde{V}}(\omega,p) = \exp\{i\omega\tau(p)\}\,R(p) \qquad 5.2.1.2-1$$

where R(p) contains the source and receiver directivity functions and any transmission coefficient on the ray(Chapman, 1978). The function $\tau(p)$ is defined as

$$\tau(p) = \int_{z_0}^{z} q(p,\eta)\,d\eta \qquad 5.2.1.2-2$$

where z_0 is the depth of the source. The corresponding seismogram is

$$U(t,x) = \frac{1}{2\pi}\,S^{+}(t) * \sum_{t=\theta(p,x)} \frac{R(p)}{|\theta'(p,x)|} \qquad 5.2.1.2-3$$

where $s^{+}(t)$ is the time derivative of the Hilbert transform of s(t).

5.2.1.3 Reflected ray.

The WKBJ approximation for the reflected ray can be expressed as

$$\hat{\tilde{V}}(\omega, p) = \exp\left\{ i\omega \tau(p) \right\} R(p) \qquad 5\cdot2\cdot1\cdot3-1$$

Considering a general case where the functions $\tau(p)$ and R(p) are both complex we have

$$\tau(p) = \tau_R(p) + i\,sgn(\omega)\,\tau_I(p) \qquad 5\cdot2\cdot1\cdot3-2a$$

$$R(p) = R_R(p) + i\,sgn(\omega)\,R_I(p) \qquad 5\cdot2\cdot1\cdot3-2b$$

where the subscripts R and I represent the real and imaginary components respectively. $\tau_I(p) \geq 0$ and the imaginary parts of the function are chosen when w is positive. Taking the inverse Fourier transform of equation 5.2.1.3-1 we obtain

$$\tilde{V}(t, p) = \frac{1}{\pi} I_m \left[\frac{R(p)}{t - \tau(p)} \right] \qquad 5\cdot2\cdot1\cdot3-3$$

The corresponding seismogram is obtained from equation 5.2.1-5b as

$$U(t,x) = -\frac{1}{2\pi^2} S^{+}(t) * \int_{-\infty}^{\infty} I_m \left[\frac{R(p)}{t - \theta(p,x)} \right] dp \qquad 5\cdot2\cdot1\cdot3-4$$

The algorithm for the WKBJ synthetic VSP seismogram is based on the above formulae 5.2.1.1-4, 5.2.1.2-2 and 5.2.1.3-4.

5.3 ACOUSTIC IMPEDANCE.

The acoustic impedance is the product of the density, r, and the compressional wave velocity, V, of the rock. The acoustic impedance computed from the density and sonic logs is shown in figure 5.2a. Also shown in figure 5.2b is the amplitude reflection coefficient, A_r, for normal incidence computed from the relation

$$A_r = \frac{\rho_2 V_2 - \rho_1 V_1}{\rho_2 V_2 + \rho_1 V_1} \qquad 5\cdot3-1$$

where $\rho_1 V_1$ and $\rho_2 V_2$ are the acoustic impedances of the material above and below the interface. This is the vertical incidence approximation which is valid for most VSP configuration. Here, it has been assumed that the fractures are situated against a material of density 2700kg/m^3 and compressional wave velocity 5929m/s, which are the average values computed from the density and sonic logs. The value of the reflection coefficient necessary to generate a detectable reflection at the surface depends on a variety of factors including the effeciency of the recording instruments and the frequency content of the seismic source. Granite is a very compact material as such we would expect that high frequencies in the seismic source would be preserved. High frequencies are necessary for better resolution.

If we assume that boundaries are detectable if their overall reflection coefficient is greater than 10%(Anstey, 1970), then we may conclude that the two major fracture

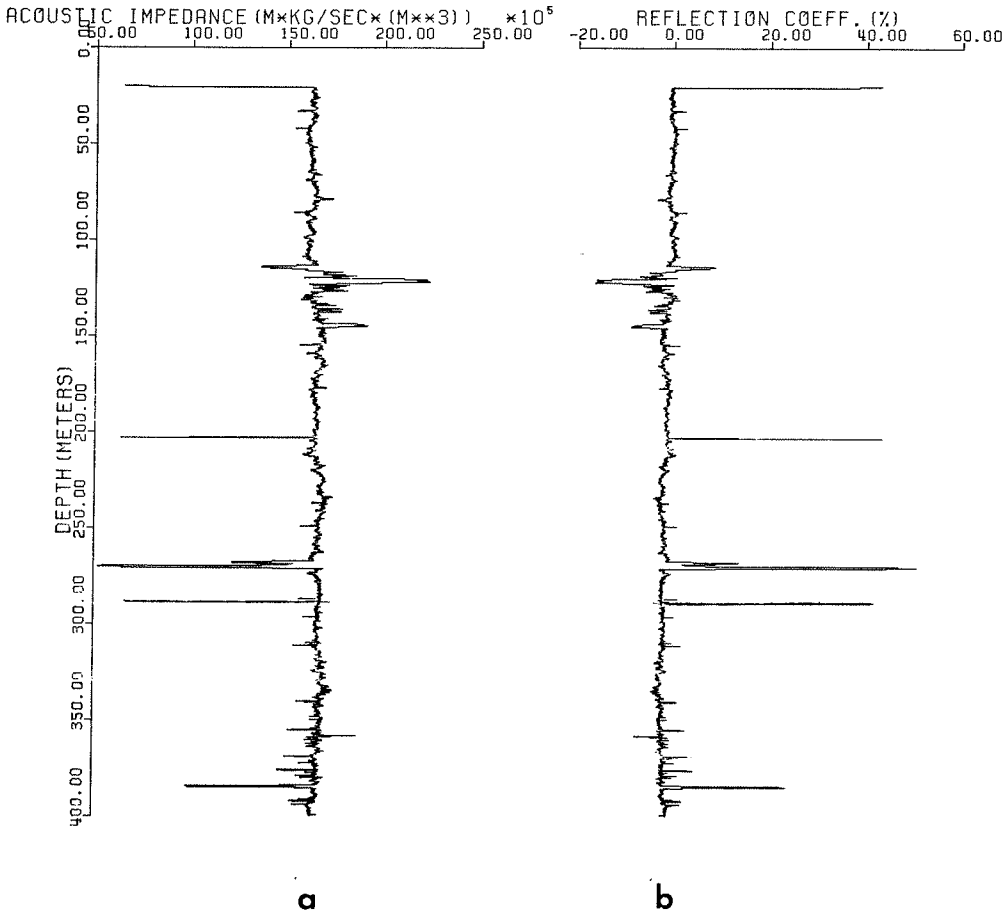

Fig.5.2: (a) Acoustic impedance and (b) reflection coefficient from sonic and density log.

zones located at 90m-150m and 267m-272m should be detectable by seismic methods. The fracture zone located at 267m-272m is believed to be part of an extensive fracture zone detected by a high resolution seismic survey(Green and Mair, 1981). This fracture zone extends to a depth of 260m in borehole URL-5 and 326m in borehole URL-1(Soonawala, 1983).

5.4 THEORETICAL SEISMOGRAMS.

The velocity and density data used to design the model were obtained from the velocity and density logs. The logs were smoothed into depth intervals within which the velocity and density values are considered to be constant. This model is shown in figure 5.3. It is recognized that some reduction in fidelity of the model was entailed in disregarding the detailed velocity and density variation on the log. This step was taken, however to obtain a practical number of model sections that could readily be programmed. Nevertheless, the important features of the logs, namely the anomalous velocity and density intervals representing the fracture zones have been maintained.

Because the WKBJ method assumes horizontal layering, the fracture zones in the model are assumed to be horizontal. Twenty shot points located vertically at 20m intervals starting from the surface were utilized. The resulting Synthetic Vertical Seismic Profile for a geophone offset of 50m is shown in figure 5.4.

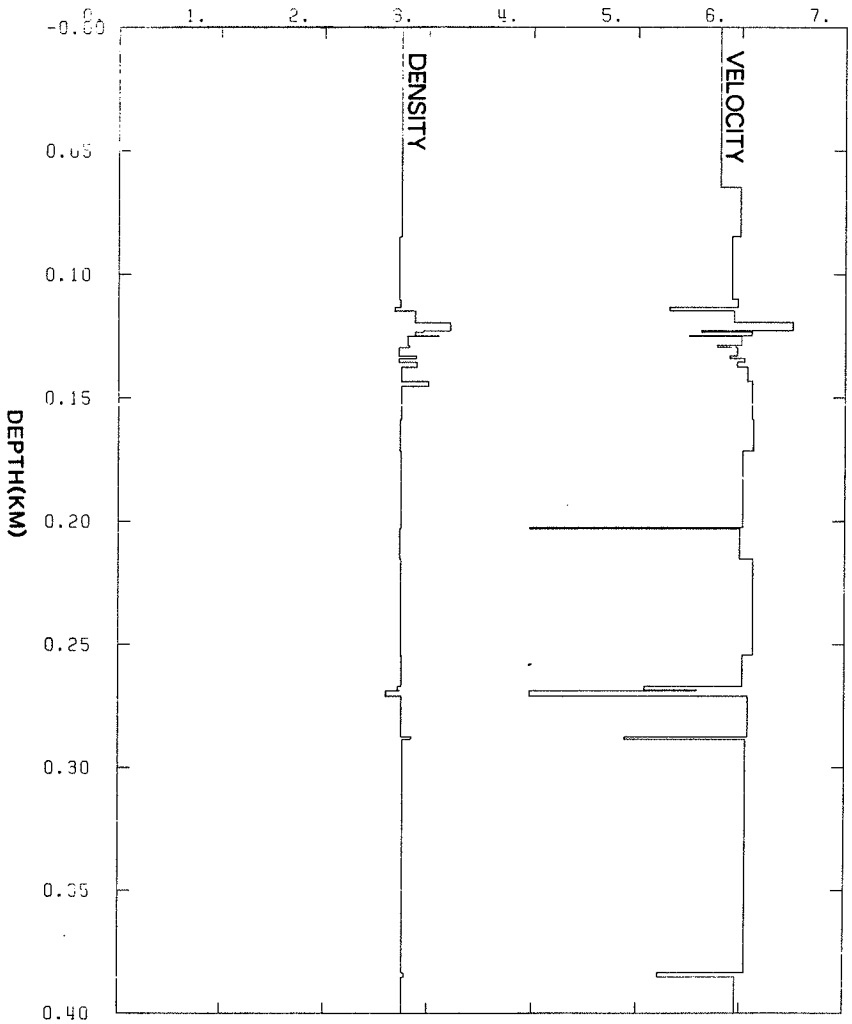

Fig.5.3: Interval velocity and density of model.

The initial pulses from the different shot points arrive at the geophone with increasing arrival time. These initial pulses constitute the direct wave. To determine the depth of a reflector, the primary reflection event is continued across to the direct wave curve. The event marked primary reflection 1 and which arrives at the surface at 0.049sec, is the reflection from the fracture zone located 119.8-122.8m; the event marked primary reflection 2 and which arrives at the surface at 0.075sec, is the reflection from the fracture zone located at 202.5-203.1m; the event marked primary reflection 3 and which arrives at the surface at 0.097sec, is a superposition of reflections from the fracture zones located at 267-271m and 287.5-288.4m; the event marked primary reflection 4 and which arrives at the surface at 0.135sec, is the reflection from the fracture zone located at 383.6-385.2m. A major attraction of VSP is that the various wavefields can be separated by filtering techniques and studied in detail(Carswell et al.1984). The WKBJ algorithm permits different wavefields to be generated separately. Figure 5.5 represents the primary reflections in figure 5.4 plotted to a different scale. Notice the emergence of the event marked primary reflection A and which arrives at the surface at 0.029sec. This event represents the reflection from the fracture zone located at 113.2-114.8m. The WKBJ algorithm can generate synthetic seismograms at various geophone offsets. This allows us to study the changes in the waveform with increasing offset.

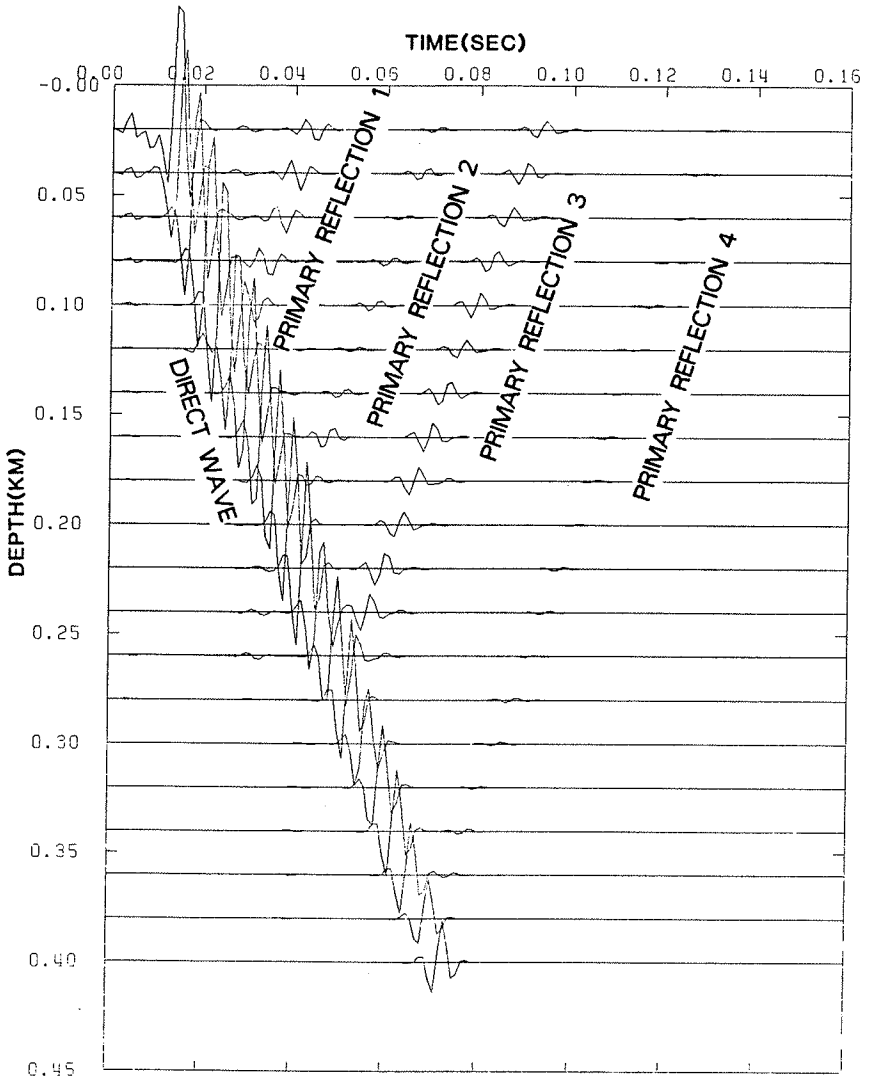

Fig.5.4: Synthetic VSP for a geophone located at 50 meters.

Figures 5.6 through 5.8 represent the primary reflection wavefield for geophone offset of 100m, 150m and 200m. A general increase in arrival time with increasing offset can be noticed. Notice also the decrease in resolution between the primary reflection A and primary reflection 1. At an offset of 150m, these two events are barely resolved and at an offset of 200m, there is no resolution and a new waveform for primary reflection 1 emerges.

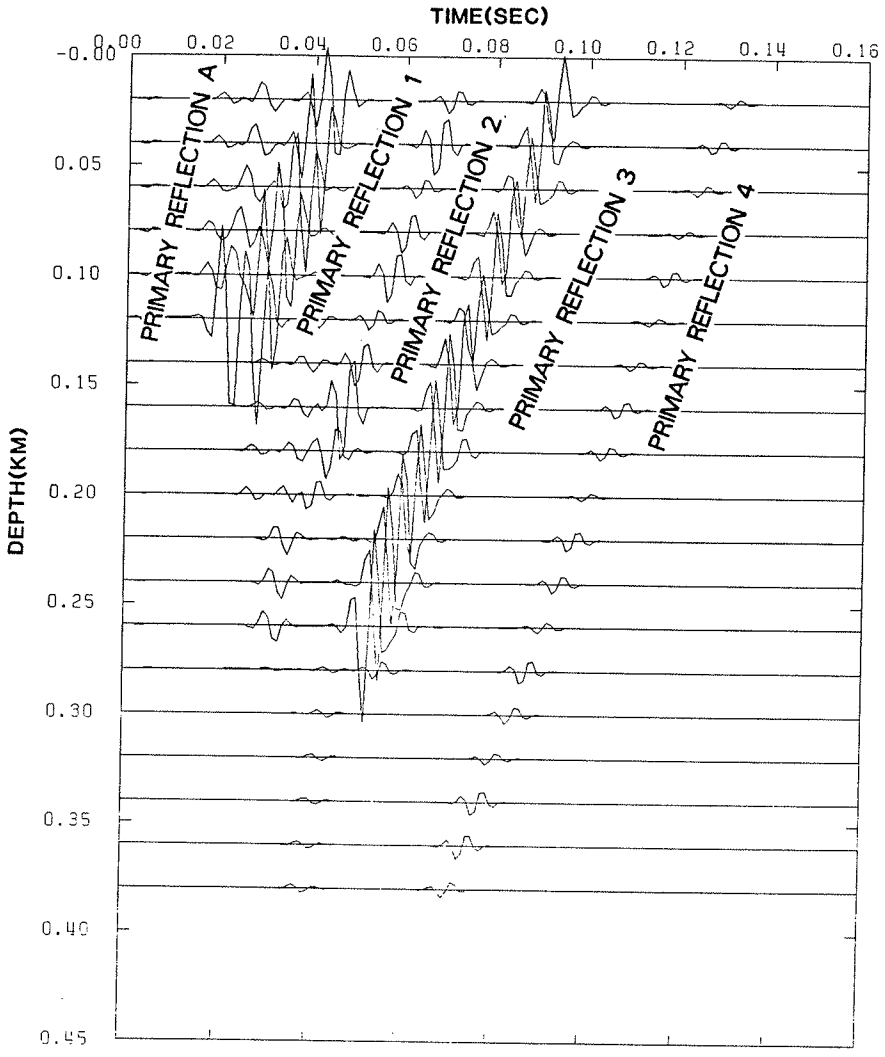

Fig.5.5: Primaries only Synthetic VSP for geophone located at 50 meters.

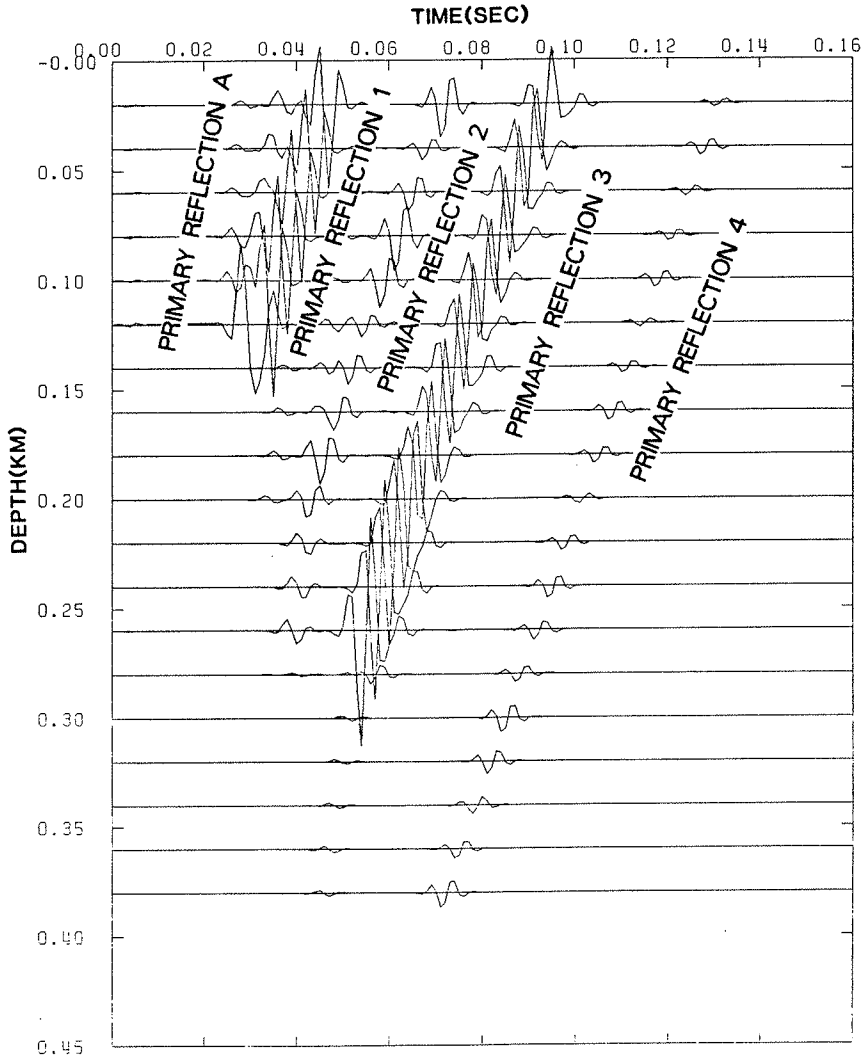

Fig.5.6: Primaries only Synthetic VSP for geophone located at 100 meters.

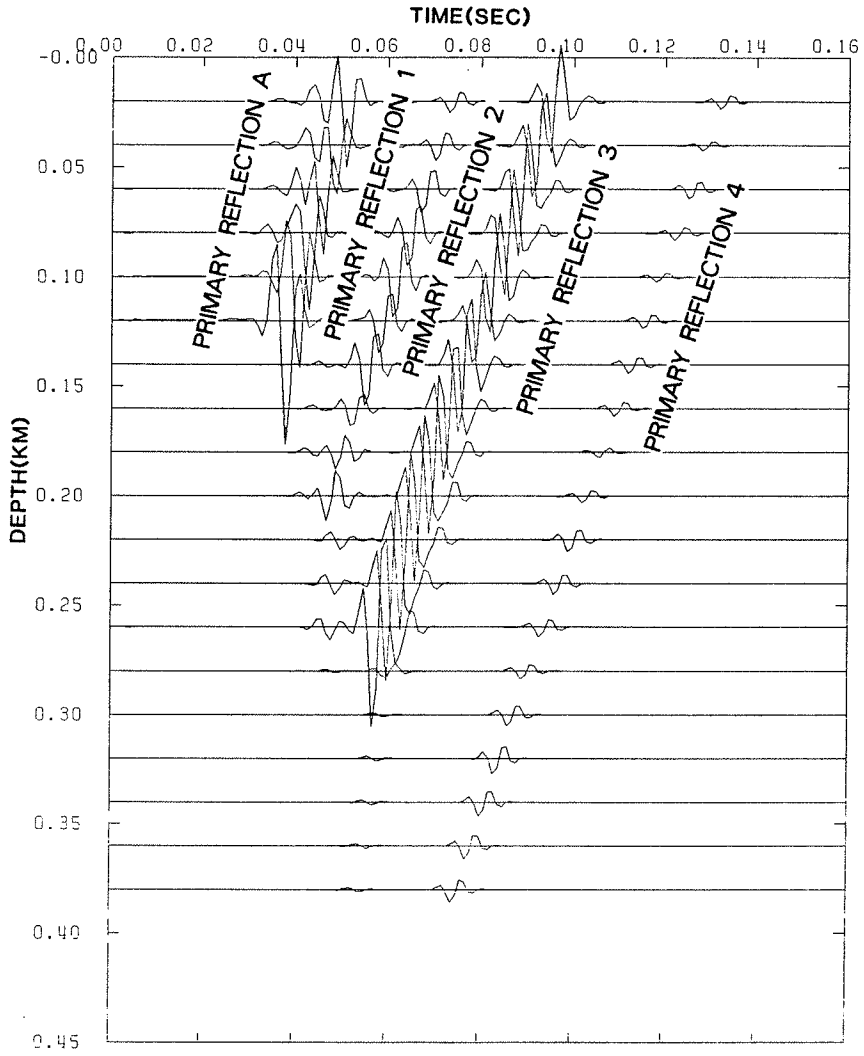

Fig.5.7: Primaries only Synthetic VSP for geophone located at 150 meters.

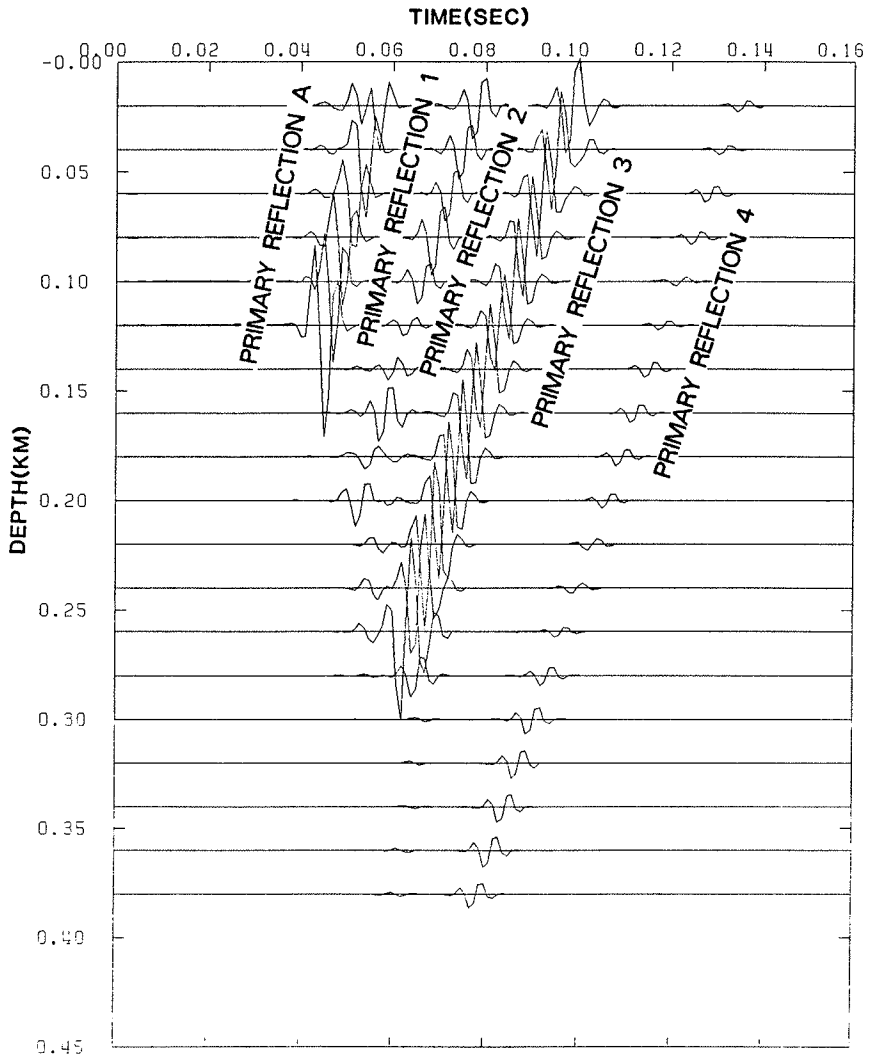

Fig.5.8: Primaries only Synthetic VSP for geophone located at 200 meters.

Chapter VI

CONCLUSION.

This thesis is concerned with the detection of fracture zones by geophysical methods within a granitic formation. The methods considered are geophysical well logging and Vertical Seismic Profiling(VSP) techniques. The theory of those geophysical logs considered most suitable for fracture detection have been reviewed. The following conclusions and recommendations were arrived at.

The performances of the normal(16'' and 32''), focused-beam and single-point resistance logs are affected by the resistivity of the formation, the macro-anisotropy, the resistivity contrast between the formation and the borehole fluid and the ratio of the electrode spacing(radius of electrode in the case of the single-point) to the borehole radius. For electrode spacing(radius of electrode in the case of single-point) very large compared to the borehole radius, the apparent resistivity measured by the logging tool is approximately equal to the mean resistivity of the fracture zone. For electrode spacing very small compared to the borehole diameter, the apparent resistivity measured by the logging tool approaches the borehole fluid resistivity.

With a large spacing, the measured current is able to penetrate deeper into the surrounding fracture zones. This however, is achieved at the expense of the vertical resolution; because as the electrode spacing increases it becomes increasingly difficult to resolve the very thin fractures.

For a fixed electrode spacing, the apparent resistivity measured by the logging tool, approaches the resistivity of the borehole fluid as the resistivity contrast between the fracture zone and the borehole fluid increases. This phenomenom is due to the tendency of the measured current to take the least resistive path; the current therefore travels along the fluid column in the borehole instead of within the fractures.

The resistivity of the fracture zones will be controlled primarily by the water content and to a lesser extent by the mineralogical composition of the fracture infilling materials. This is because of the much higher conductivity of water relative to the constituent minerals in most rocks.

Fracture zones in a granite pluton may exhibit macro-anisotropy as a result of the presence of different fracture infilling materials of contrasting resistivities. The macro-anisotropy coefficient in the presence of horizontal fractures is greater than unity. In the presence of subvertical fractures, the macro-anisotropy coefficient is less than unity. Subvertical fractures reduce the effective

macro-anisotropy coefficient of the fracture zone by offering a vertical path to the measured current and thereby reducing its penetration. The apparent resistivity measured by the logging tool in the presence of subvertical fractures would therefore be less than the mean resistivity of the fracture zone.

Because of its special arrangement, the focused-beam log is less affected by the resistivity contrast between the borehole fluid and the formation. It possess the best vertical resolution amongst the electrical resistivity logs.

The single-point log is very effective only in abnormaly low resistive fracture zones. This is due to the fact that it has a very shallow penetration.

To reduce the resistivity contrast between the granite formation and the borehole fluid, it is recommended that borehole fluid of high resistance be used. This would increase the amount of current flowing into the formation.

The precise nature of the spontaneous potential anomaly in fractured crystalline formation is not very clear. It is influenced by several factors including the salinity of the fluid flowing through the fractures, the pressure gradient in the fractures, the presence of divalent ions, the permeability of the fractures and the mineralogical composition of the fracture infilling materials.

The response of the neutron log in granite should not be interpreted only in terms of porosity. The effect of thermal neutron absorbing materials should be taken into consideration. The distance travelled by the thermal neutrons before capture is determined by the amount of thermal neutron absorbing elements in the formation. In sedimentary formations, the hydrogen contained in shales and the rock pore system constitute the major thermal neutron absorbing element. In granite other elements such as sodium, potassium and iron all have a greater tendency than hydrogen in absorbing thermal neutrons.

The density values derived from the density log should be corrected for the Z/A effect if the values are intended for quantitative gravity analysis. For density logging in granite, the use of two gamma-ray detectors is recommended. This is so that the effect of secondary gamma emission by the formation can be corrected for. The fracture zones encountered in borehole URL6 produce well defined anomalies on the density log.

The compressional wave transit time is related to the elastic properties of the fracture zones and may be used to measure the fracture frequency. The sonic log responds to both the major and minor fracture zones encountered in borehole URL6. Recent studies by others show that the compressional wave transit time is not as sensitive to the presence of fractures as the amplitude of shear and tube waves.

Unfortunately, in sonic logging it is only the compressional wave transit time which is measured and the additional information from the shear and tube waves are lost. For fluid-filled fractures, it is recommended that the full acoustic waveform be recorded so that the shear and tube wave anomalies can be measured.

In granite, the use of gamma ray spectroscopy may provide a better means of locating fracture zones. The total gamma count recorded by the conventional gamma log, may not show considerable variation due to the high concentration of potassium, thorium and uranium in granite. The temperature log can be used to detect permeable fracture zones and the caliper log for open fracture zones.

In order to obtain a quantitative measure of the agreement between the various geophysical logs in detecting fracture zones, cross-correlation was performed for different pairs of well log data. Because most common cross-correlation algorithms require that the data values occur at equal intervals, Lagrange's interpolation method was used to obtain an evenly spaced data points. This method was employed because of the simplicity of its recursion formulae which makes it easy to program. To estimate the error of this interpolation method, we compared the original and the interpolated well log data using different number of points for the interpolation. Results of this experiment indicate that for well log data, in order to minimize the interpolation

error, no more than five data points are required for acceptable interpolation results. This conclusion strictly applies only to the Lagrange's interpolation method. A similar conclusion has been obtained by Naidu(1970).

Systematic correlation has shown that geophysical logs can be used to characterize fractured zones in a granitic terrain. Two major fracture zones have been deduced from the well log data from borehole URL6. They are located at 98-150m and 267-272m. The later is characterized by a low electrical resistivity, low density, low compressional wave velocity, low neutron count rate, anomalous borehole diameter and a temperature increase. These observations suggest a permeable fracture zone. The other fracture zone is characterized by anomalies on the neutron, density, sonic and resistivity logs which suggest the presence of different minerals. Other intervals where fracturing is apparent are 202.5-215m and 286.5-289.4m. There is a good confirmation between the above characterization and those obtained from television survey and core sample analysis(fig.3.1 and 3.2). The two major fracture zones correspond to the three well-fractured zones in figure 3.1. Here, the fracture frequencies are very high and fractures produce significant anomalies on almost all the logs. In contrast, the minor fracture zones have lower fracture frequencies and produce anomalies on a limited number of logs. Core sample analysis indicates that the dominant fracture infilling materials

between 203.5m and 215m are hematite and limonite. Even though both of these infilling materials are denser than granite and are also good thermal neutron absorbers, yet there is no distinct anomaly within this interval on either the density or neutron log. This suggests that there are other important factors which also contribute to the magnitude of the anomaly. One of such factors is the fracture density or frequency. The thickness of the fractures encountered in the borehole URL6 is in the order of few millimetrs and to effectively resolve such thin fractures, we would need to employ instruments with very high vertical resolution. Most commercial logs are not designed for such situations as they do not possess such fine resolution. Therefore, in order to produce a significant anomaly on the geophysical logs, the fracture density will have to be very high.

The results of the cross-correlation analysis suggest that the cross-correlation value may not always be a good measure of the agreement between various logs in detecting fracture zones. The reason is that cross-correlation is based on similarity of waveforms rather than similarity in detecting lithologic boundaries. The cross-correlation values obtained for the fracture zone at 267-272m are generally higher than those of the fracture zones at 90-150m. This difference is attributed to the difference in the mineralogical and textural nature of the two fracture zones. The

density, neutron and resistivity(16'') logs consistently give high correlation values while the gamma and caliper logs give consistently low correlation values. The cross-correlation as a function of depth is perhaps the best way to present the similarity between the geophysical logs. Such presentations indicate how the geophysical logs correlate at various depths and in particular within the fracture zones as described in the main text of this thesis.

Synthetic seismograms are routinely computed not only for comparison with the seismic data but also for correlating well log data to the seismic data. Synthetic VSP seismograms are usually computed for vertical incidence(Wyatt, 1981). But in actual practice the angle of incidence departs from the vertcal, as receivers are usually located at some distance from the well. At angles other than the vertical, the conversion of P- to S- wave energy and changes in the reflection coefficient affect the shape of the synthetic seismograms(Douze, 1978). For this reason, Synthetic VSP seismograms at non-vertical incidence was developed from the WKBJ algorithm(Chapman, 1978; Owusu and Moon, 1984). The resulting Synthetic VSP seismograms demonstrate the capability of VSP in detecting the location of the major fracture zones. Well log data from borehole URL6 indicate that the acoustic impedance contrast at the fracture zones is adequate enough to generate detectable reflections at the surface. However, the field procedures should be carefully

planed and a high resolution VSP survey is recommended. Higher resolution means broader frequency bandwidth, which must be obtained by extending the high frequency end of the spectrum. Explosive charges should be as small as possible(0.5-1.5kg). Ziolkowski and Lerwill (1979) have shown that we can shift the spectrum into the useful band by choosing the right size charge. With small charges, the spectrum is shifted towards the higher frequencies. High frequencies are needed to resolve the fracture zones. With larger charges, because of the shift to lower frequencies, the ability to excite surface waves is enhanced. In an attempt to improve the resolution by using smaller charges, we may run into signal-to-noise ratio problems. To overcome these, it may be necessary to consider vertical stacking during the data processing sequence. The data from two or more adjacent levels are time shifted to align coherent events. These recordings are then added to enhance coherent events.

Two VSP configurations have been described. At the URL6 site, the configuration with sources along the shaft are logically acceptable.

Geophones with high natural frequencies are also recommended. Geophones usually have filtering influence on the recorded data and this influence is quite variable depending upon the seismic frequency bandwidth, geophone group, spread length and the geophone-ground coupling(Hoover and O'Brien,

1980). Even though single geophones cannot reduce surface waves and other horizontally traveling noise, they are sometimes prefered to geophone groups. Ziolkowski and Lerwill (1979) have shown that when the terrain is very rough, like at the URL6 site, even a short array can act as a filter in which the higher frequencies of the signal are attenuated. In a situation like this, the single geophone has an advantage in obtaining a broader bandwidth, but in doing so it leaves the problem of surface waves to be solved elsewhere.

BIBLIOGRAPHY

Ahmad, M.U., 1964, A laboratory study of streaming potentials Geophys. Prosp., vol. 12, p 49-64.

Anstey, N.A., 1970, Signal characteristics and instrument specification. Seismic prospecting instruments, vol.1, Geoexploartion monogr., ser.1, no.3, Borntraeger.

Aquilera, R., 1980, Naturally fractured reserviors. PennWell Publ. Co. Tulsa Oklahoma.

Balch, A.H., Lee, M,W., Miller, J.J. and Ryder, R.J., 1982, The use of Vertical Seismic Profiles in seismic investigations of the earth. Geophysics, vol.47, p 909-918.

Biot, M.A., 1952, Propagation of elastic waves in a cylindrical borehole containing a fluid. J. Appl. Physics, vol. 23, p 997-1005.

Birch, F., 1947, Temperature and heat flow in a well near Colorado Springs. Am. J. Sci., vol. 245, p 733-752.

Brisbin, W, C., 1982, In: '' Proceeding of the Twelfth Information Meeting of the Nuclear Fuel Waste Management Program'', p 369-373, Atomic Energy of Canada Limited Technical Record TR-200.

Brisbin, W.C., 1979, A gravity profile across the Lac du Bonnet batholith in southeastern Manitoba. Atomic Energy of Canada Limited Technical Record, TR=17.

Brown, A., 1982, A synopsis of the geology of the URL site. In: ''Preceedings of the Twelfth Information Meeting of the Nuclear Fuel Waste Management Program'', p 302-313, Atomic Energy of Canada Limited Technical Record, TR=200.

Campbell, D.L., 1977, Model for estimating electric macroanisotropy coefficient of aquifers with horizontal and vertical fractures. Geophysics, vol 42, p 114-117.

Carswell, A., Tang, R., Moon, W. and Dillistone, C., 1984, A new method of waveform separation in VSP. Abstract, The CSEG Convention, Calgary, June 1984.

Chapman, C.H., 1978, A new method for computing synthetic seismogram. Geophys. J. R. Astr. Soc., vol. 54, p 481-518.

Chen, C.H. and Toksoz, M.N., 1981, Elastic wave propagation in a fluid-filled borehole and synthetic acoustic logs. Geophysics, vol. 46, p 1042-1053.

Cormier, V.F. and Richards, P.G., 1977, Full wave theory applied to a discontinous velocity increase: the inner core boundary. Geophys. J., vol. 37, p 73-90.

Dakhnov, V.N., 1962, Geophysical well logging. Quarterly of the Colorado School of Mines, vol. 57, no. 3, 445p.

Danes, Z.F., 1960, A chemical correction factor in gamma-gamma density logging. J. Geophys. Research, vol. 65, p 2149-2653.

Davison, C.C., 1982, Hydrogeological studies at the URL site. In: '' Preceedings of the Twelfth Information Meeting of the Nuclear Fuel Waste Management Program'', p 332-353, Atomic Energy of Canada Limited Technical Record, TR=200.

Davison,C.C., Brown, A. and Soonawala, N.M., 1982, Preconstruction site evaluation program at the Canadian Underground Research Laboratory. In: ''Proceedings of the Fourteenth Information Meeting of the Nuclear Fuel Waste Management Program'', p 162-187, Atomic Energy of Canada Limited Technical Record, TR=207.

Doll, H.G., 1951, The Laterolog: A new resistivity logging method with electrodes using an automatic focusing system. Transactions American Institute of Minning and Metallurgical Engineers, vol. 198, p 17-32.

Douze, E.J., 1979, Synthetic Seismograms at non-vertical incidence. Geophys. Prosp., vol. 27, p 564-575.

Fuchs, K., and Muller,G., 1971, Computation of synthetic seismogram with the reflectivity method and comparison with observation. Geophys. J., vol. 23, p 417-433.

Gal'perin, E.I., 1973, Vertical seismic profiling: J.E White, editor, SEG Spec. Pub., no. 12, 270 p.

Gerald,C.F., 1980, Applied Numerical Analysis. Don Mills, Ontario, Addison-Wesley Publishing Company.

Gratsinkiy, V.G., Kozyar, V.F. and Dzeban, I.P., 1968, The effect of a fracture on a head-wave field. Physics of the solid earth. no.1, p 122-129.

Green, A.G. and Mair, J.A., 1983, Subhorizontal fractures in a granitic pluton: Their detection and implication for radioactive waste disposal. Geophysics, vol. 48, p 1428-1449.

Green, A.G. and Mair, J.A., 1981, High-resolution seismic reflection profiles reveal fracture zones within a 'homogeneous' granite batholith. Nature, vol. 294, p 439-442.

Morse, J.G., 1977, Nuclear methods in mineral exploration and production. Elsevier Scientific Publ. Co., New York.

Hajnal,Z., Stauffer,M.R., King,M.S., Wallis, P.F., Wang, H.F and Jones, L.E.A., 1983, Seismic characteristics of a precambrian pluton and its adjacent rocks. Geophysics, vol. 48, p 569-581.

Hoover, G.M and O'Brien, J.T., 1980, The influence of the planted geophone on seismic land data. Geophysics, vol. 45, p 1239-1253.

Jackson, P.D., 1981, Focussed electrical resistivity arrays:some theoretical and practical experiments. Geophys. Prosp., vol. 29, 601-626.

Johnston, D.H., Toksoz, M.N. and Timur, A., 1979, Attenuation of seismic waves in dry and saturated rocks:II. Mechanism. Geophysics, vol. 44, p 691-711.

Kayal, J.R., 1979, Electrical and gamma-ray logging in Gondwana and Tertiary coal fields of India. Geoexploration, vol. 17, p 243-258.

Kennet, P., Ireson, I.R. and Conn, P.J., 1980, Vertical Seismic Profiles: their applications in exploration geophysics. Geophys. Prosp., vol. 28, p 676-699.

Keys, W.S., 1979, Borehole geophysics in igneous and metamorphic rocks. Transaction of the SPWLA annual logging symposium, no. 20, p 1-26.

Kunz, K.S. and Moran, J.H., 1958, Some effects of formation anisotropy on resistivity measurements in boreholes. Geophysics, vol. 23, p 770-794.

Lau, J.S.O., Bisson,J.G. and Auger, L.F., 1983, A preliminary report on the URL6 borehole television survey. Atomic Energy of Canada Limited Technical Report, TR-115-28.

Naidu, P.S., 1970, A statistical study of the interpolation of randomly spaced geophysical data. Geoexploration, vol. 8, p 61-70.

O'Connel, R.J and Budiansky, B., 1977, Viscoelatic properties of fluid saturated cracked solids. J. Geophys. Res., vol. 82, p 5919-5732.

O'Connel, R.J and Budiansky, B., 1974, Seismic velocities in dry and saturated cracked solids. J. Geophys. Res., vol. 79, p 5412-5426.

Ogilvy, A.A., Ayed, M.A. and Bogoslovsky, V.A., 1969, Geophysical studies of water leakages from reserviors. Geophys. Prosp., vol. 22, p 36-62.

Olhoeft, G.R., 1981, Electrical properties of granite with implication for the lower crust. J. Geophys. Research, vol. 86, p 931-936.

Owusu, J.C and Moon, W.M., 1984, WKBJ theoretical seismograms for VSP at the AECL-URL site, near Lac du Bonnet, Manitoba. Atomic Energy of Canada Limited Technical Report.

Paillet F.L. and White, J.E., 1982, Acoustic modes of propagation in the borehole and their relationship to rock properties. Geophysics, vol. 47, p 1215-1228.

Schlumberger Limited, 1972, Log Interpretation Principles. vol. I, New York.

Soonawala, N.M., 1983, Geophysical logging in granites. Geoexploration, vol. 21, p 221-230.

Soonawala, N.M., 1982, Geophysical investigations at the site of the Underground Rsearch Laboratory. In: ''Preceedings of the Twelfth Information Meeting of the Nuclear Fuel Waste Management Program '', p 314-331, Atomic Energy of Canada Limited Technical Record, TR=200.

Tammemagi, H.Y., 1976, Geological Disposal of Radioactive Wastes : The Canadian Development Program. Atomic Energy of Canada Limited Report, AECL-5392.

Telford, W.M., Geldart, L.P., Sherriff, R.E and Keys, D.A., 1981, Applied Geophysics. Cambridge Cambridge University Press.

Tittle, C.W. and Allen, L.S., 1966, Theory of neutron logging II. Geophysics, vol. 31, p 214-224.

Tittman, J. and Wahl, J.S., 1964, The physical foundations of formation density logging. Geophysics, vol. 30, p 284-294.

Tsang, L. and Rader, D., 1979, Numerical evaluation of the transient acoustic waveform due to a point source in a fluid-filled borehole. Geophysics, vol. 44, p 1706-1720.

Tuman, V.S., 1963, Thermo-telluric currents generated by an underground explosion and other geological phenomena. Geophysics, vol. 28, p 91-98.

Wyatt, K.D., 1981, us Synthetic vertical seismic profile, Geophysics, vol. 46, p 880-891.

Ziolkowski, A and Lerwill, W.E., 1979, A simple approach to high resolution seismic profiling for coal. Geophys. Prosp., vol. 27, p 360-393.

Appendix A

TRANSFORMATION FROM AN ANISOTROPIC TO ISOTROPIC MEDIUM.

If the variation of the coefficient of macroanisotropy with r and z is expressed in the form(Kunz and Moran, 1958)

$$\lambda = S(r) \cdot k(z) \qquad A\cdot 1$$

then by equations 2.1-1 and 2.1-7,

$$\frac{S}{r}\frac{\partial}{\partial r}\left(\frac{Sr}{R}\frac{\partial V}{\partial r}\right) + \frac{1}{k}\frac{\partial}{\partial z}\left(\frac{1}{kR}\frac{\partial V}{\partial z}\right) = 0 \qquad A\cdot 2$$

By introducing the new variables

$$r' = \int_0^r \frac{dr}{S(r)} \quad \text{and} \quad z' = \int_0^z k(z)\,dz \qquad A\cdot 3$$

and letting

$$V(r,z) = V'(r',z')$$

we have(Kunz and Moran, 1958)

$$\frac{\partial V}{\partial r} = \frac{1}{S}\frac{\partial V'}{\partial r'} \quad \text{and} \quad \frac{\partial V}{\partial z} = k\frac{\partial V'}{\partial z'} \qquad A\cdot 4$$

Equation A.2 becomes

$$\frac{\partial}{\partial r'}\left(\frac{r}{R}\frac{\partial V'}{\partial r'}\right) + \frac{\partial}{\partial z'}\left(\frac{r}{R}\frac{\partial V'}{\partial z'}\right) = 0 \qquad A\cdot 5$$

By introducing a new value of resistivity at each point given by(Kunz and Moran, 1958)

$$R' = \frac{r'}{r} R$$

Equation A.5 can be written as

$$\frac{1}{r'} \frac{\partial}{\partial r'}\left(\frac{r'}{R'} \frac{\partial V'}{\partial r'}\right) + \frac{\partial}{\partial z'}\left(\frac{1}{R} \frac{\partial V'}{\partial z'}\right) = 0 \qquad A.6$$

which is equation 2.1-8. The primed parameters represent the equivalent in an isotropic medium of resistivity R'. For an infinite, homogeneous, macroanisotropic medium λ is constant; and if we make

$$S(r) = \lambda \quad \text{and} \quad k(z) = 1$$

then from equation A.3

$$r' = \frac{r}{\lambda} \quad , \quad z' = z \quad \text{and} \quad R' = \frac{R}{\lambda} = R_H \qquad A.7$$

which is equation 2.1-25.

Appendix B

LATEROLOG 7 IN AN INFINITE HOMOGENEOUS MEDIUM.

Consider a Laterolog 7 array in an infinite homogeneous medium with A as the origin(fig.4.5). The potential at any point (r,z) can be expressed as follows(Jackson, 1981):

$$V(r,z) = \frac{R}{4\pi}\left\{ \frac{I_o}{(r^2+z^2)^{1/2}} + \frac{I_H/2}{((b+c+d+z)^2+r^2)^{1/2}} + \frac{I_H/2}{((b+c+d-z)^2+r^2)^{1/2}} \right\}$$

$$= \frac{R}{4\pi}\left\{ I_o F(r,z) + I_H E(r,z) \right\} \qquad B\cdot 1$$

where R is the resistivity of the medium and b, c and d are the elctrode spacing and

$$F(r,z) = \frac{1}{(r^2+z^2)^{1/2}}$$

and

$$E(r,z) = \frac{1}{2((b+c+d-z)^2+r^2)^{1/2}} + \frac{1}{2((b+c+d+z)^2+r^2)^{1/2}} \qquad B\cdot 2$$

The potential of a point on along the axis (0,z) of the electrode is

$$V(0,z) = \frac{R}{4\pi}\left\{ I_o F(0,z) + I_H E(0,z) \right\} \qquad B\cdot 3$$

which is equation 2.1.2-2.

Appendix C

POTENTIAL FIELD OF THE LATEROLOG WITHIN A BOREHOLE

The potential at M(fig.4.4) is the algebraic sum of the contributions from the three current electrodes A_0, A and A'. The potential at any point (0,z) in the borehole is given by equation 2.1-34 as

$$V_s(0,z) = \frac{IR_s}{2\pi^2 a}\left[\frac{\pi}{2z} + \int_0^\infty C(m)\cos mz\, dm\right] \qquad C\cdot 1$$

where a is the radius of the borehole. The potential due to the electrode A_0 at M is given by

$$V_{A_0}(M) = \frac{I_0 R_s}{4\pi a}\left[F(0,b') + \frac{2}{\pi}\int_0^\infty C(m)\cos mb'\, dm\right] \qquad C\cdot 2$$

Similarly, the potential due to A and A' at M is

$$V_{AA'}(M) = \frac{I_1 R_s}{4\pi a}\left\{E(0,b') + \frac{2}{\pi}\int_0^\infty C(m)\left[\cos(m(c'+d')) + \cos(m(2b'+c'+d'))\right] dm\right\} \qquad C\cdot 3$$

where I_1 is the current from AA' and

$$b' = \frac{A_0M}{a}\ , \quad c' = \frac{MN}{a} = \frac{M'N'}{a}\ , \quad d' = \frac{NA}{a} = \frac{N'A'}{a}$$

If we let

$$J_0 = \frac{I_1}{I_0}$$

Then the total potential at M is the sum of $V_{A_0}(M)$ and $V_{AA'}(M)$:

$$V_{A_0AA'}(M) = \frac{R_B I_0}{4\pi a}\left\{F(0,b') + J_0 E(0,b') + \frac{2}{\pi}\left\{\int_0^\infty C(m)\cos mb'\,dm + J_0\int_0^\infty C(m)\left[\cos(m(c'+d')) + \cos(m(2b'+c'+d'))\right]dm\right\}\right\}$$

$$= \frac{R_B I_0}{4\pi a}\left\{F(0,b') + J_0 E(0,b') + F'\left(\lambda', \frac{R}{R_B}, b', c', d'\right)\right\} \qquad c.4$$

which is equation 2.1.2-10. Here

$$F'\left(\lambda, \frac{R}{R_B}, b', c', d'\right) = \frac{2}{\pi}\left\{\int_0^\infty C(m)\cos mb'\,dm + J_0\int_0^\infty C(m)\left[\cos(m(c'+d')) + \cos(m(2a'+c'+d'))\right]dm\right\}$$